# A Measurement of Z Boson Production and Rapidity Distribution in Proton-Antiproton Collisions at $\sqrt{s} = 1.96$ TeV

---

**Aidan Robson**
*Particle Physics, University of Oxford, Keble Road, OX1 3RH*
*Wadham College, Oxford, OX1 3PN*

Thesis submitted in fulfilment of the requirements for the
degree of Doctor of Philosophy at the University of Oxford

Michaelmas Term 2004

# Abstract

High-precision measurements are made of Z boson production in proton-antiproton collisions at $\sqrt{s} = 1.96\,\mathrm{TeV}$ recorded by the Collider Detector at Fermilab, using the electron decay channel.

The cross-section times branching ratio is measured to be

$$\sigma_{\mathrm{Z}} \cdot Br(\mathrm{Z} \to \mathrm{e}^{+}\mathrm{e}^{-}) = (255.7 \pm 2.4_{\mathrm{stat}} \pm 5.2_{\mathrm{sys}} \pm 15.2_{\mathrm{lum}})\,\mathrm{pb}$$

in a dataset of $194\,\mathrm{pb}^{-1}$ collected between March 2002 and June 2003. This agrees well with theoretical predictions.

The cross-section for W boson production in the electron channel has also been measured in the subset of this dataset of $72\,\mathrm{pb}^{-1}$ collected up until January 2003. Using this smaller dataset the ratio of cross-sections is determined to be

$$R \equiv \frac{\sigma_{\mathrm{W}} \cdot Br(\mathrm{W} \to \mathrm{e}\nu)}{\sigma_{\mathrm{Z}} \cdot Br(\mathrm{Z} \to \mathrm{ee})} = 10.82 \pm 0.18_{\mathrm{stat}} \pm 0.16_{\mathrm{sys}}$$

Combining these results with measurements made in the muon channel gives

$$R = 10.92 \pm 0.15_{\mathrm{stat}} \pm 0.14_{\mathrm{sys}} \ (\mathrm{e} + \mu \text{ channels}),$$

from which the branching ratio of the W to electrons and muons, and the total width of the W, have been extracted:

$$Br(\mathrm{W} \to \ell\nu) = 0.1089 \pm 0.0022 \quad (\ell = \mathrm{e}, \mu)$$

$$\Gamma(\mathrm{W}) = 2078.8 \pm 41.4\,\mathrm{MeV},$$

which are in good agreement with the Standard Model values and with other measurements.

The CKM quark mixing matrix element $|V_{cs}|$ has been extracted:

$$|V_{cs}| = 0.967 \pm 0.030.$$

The rapidity distribution $d\sigma/dy$ for $\mathrm{Z} \to \mathrm{ee}$ has also been measured over close to the full kinematic range using $194\,\mathrm{pb}^{-1}$ of data, and is found to be in good agreement with the NNLO prediction.

## Authorship

Except where stated otherwise, the studies and results reported in this thesis are the work of the author.

## Acknowledgments

I am extremely grateful to Greg Veramendi for having been so inspiring, supportive, patient, and generous with time and suggestions; and to Giulia Manca for all of her help, ideas, support and friendship.

Special thanks also to Pete Renton for all of his help and for coming often to Fermilab; and to Beate Heinemann, who was a particular source of inspiration and help.

I also thank the other people who have inspired, helped or supported me towards this work in so many different ways; among them: Agnes Robson, Godfrey Robson, Grace Durham, Pekka Sinervo, Pierre Savard, Bryan Webber, Janet Carter, Louis Lyons, Stephan Lammel, Young-Kee Kim, Eva Halkiadakis, Eric James, Willis Sakumoto, Cigdem Issever, Pasha Murat, David Waters, Michael Schmitt, James Stirling, Mandy Cooper-Sarkar, Thilo Pauly, Dustin McGivern, Helen Hayward, Anant Gajjar, Matthew Leslie, James Monk, Martin Griffiths, Nicola Pounder.

I gratefully acknowledge funding from the Particle Physics and Astronomy Research Council.

# Contents

## 4 Efficiencies and Backgrounds 61

## 5 Results 97

## List of figures

## List of tables

# Chapter 1

# Theory and Experiment

In this chapter the Standard Model of particle physics is introduced, and each of the three measurements presented in this thesis – $\sigma \cdot Br(p\overline{p} \to \mathrm{Z} \to \mathrm{ee})$, $R = \sigma(\mathrm{W})/\sigma(\mathrm{Z})$, and $d\sigma(p\overline{p} \to \mathrm{Z} \to \mathrm{ee})/dy$ – is discussed and put in context.

## 1.1. QCD and Electroweak Theory

Our current understanding of fundamental particles and their interactions other than gravity is described by a set of gauge field theories coupling the quarks and leptons that constitute matter to the vector bosons of the electromagnetic, strong and weak forces. In this section each of these field theories is described and a brief discussion given of particle masses and of renormalisation of the field theories.

**QED** Quantum electrodynamics (QED) [2] describes fermion-photon interactions and has been tested experimentally to an extraordinary level of precision – in, for example, the anomalous magnetic moment of the electron. The free Lagrangian corresponding to the Dirac equation for a fermion field $\psi$ having mass $m$ may be written:

$$\mathcal{L}_{\mathrm{free}} = \overline{\psi}(x)(i\,\partial\!\!\!/ - m)\psi(x). \tag{1.1.1}$$

The U(1) gauge symmetry is that of phase, and the requirement of local gauge invariance introduces a vector field $A_\mu$ that is identified with the photon. The Lagrangian acquires a kinetic term allowing the propagation of the vector field:

$$\mathcal{L}_{\mathrm{QED}} = \overline{\psi}(x)(i\,\not{\mathcal{D}} - m)\psi(x) - \frac{1}{4}F_{\mu\nu}(x)F^{\mu\nu}(x) \tag{1.1.2}$$

where for a particle of charge $eQ$ the covariant derivative $\mathcal{D}_\mu = \partial_\mu + ieQA_\mu$ and the field strength tensor $F_{\mu\nu} = \partial_\mu A_\nu - \partial_\nu A_\mu$, and $\mu$ and $\nu$ run over the four spacetime coordinates. Gauge symmetry disallows a photon mass term, consistent with experimental observation.

**QCD** In order to explain the observed hadron spectroscopy, quarks were postulated to carry a three-fold colour degree of freedom. Quantum chromodynamics (QCD) [3] is built on its gauge symmetry, $\mathrm{SU}(3)_{\mathrm{colour}}$, and describes the strong interaction with the introduction of eight massless vector fields corresponding to the gluons. The important difference between QCD and QED is the non-Abelian nature of the QCD gauge group. The Lagrangian may be written analogously with that of QED for quark fields $q_a$ having colour $a$:

$$\mathcal{L}_{\mathrm{QCD}} = \sum_{\text{flavours}} \overline{q}_a(x)(i\,\not{\mathcal{D}}_{ab} - m\delta_{ab})q_b(x) - \frac{1}{4}F^A_{\mu\nu}(x)F^{A\mu\nu}(x) \tag{1.1.3}$$

where now the covariant derivative contains the eight SU(3) matrices $\mathbf{t}$:

$$(\mathcal{D}_\mu)_{ab} = \partial_\mu\delta_{ab} + ig_s(\mathbf{t}\cdot\mathbf{A}_\mu)_{ab} \tag{1.1.4}$$

and

$$F^A_{\mu\nu} = \partial_\mu A^A_\nu - \partial_\nu A^A_\mu - f^{ABC}A^B_\mu A^C_\nu \tag{1.1.5}$$

where $f^{ABC}$ are the structure constants of the group. Unlike QED, in which the photon couples to electric charge but is itself neutral, in QCD the gluon carries colour and exhibits self-interaction, originating in the final term of Eqn 1.1.5. The observation of three-jet events in $\mathrm{e}^+\mathrm{e}^-$ collisions [4] provided the first experimental ‘observation’ of the gluon, and confirmation of the three-gluon vertex came from a comparison of three- and four-jet cross-sections and angular variables [5]. The numbers of colours and gluons is confirmed by, for example, comparing measured cross-sections with the corresponding theoretical computations that include colour pre-factors.

**Electroweak Theory** The electroweak theory [6] is built from the experimental observations that there are flavour-changing charged currents that couple to left-handed fermions only, flavour-conserving neutral currents, and couplings that are universal across the generations. The fermions are grouped into left-handed isospin doublets and right-handed singlets:

$$\left\{ \begin{pmatrix} \nu_\ell \\ \ell^- \end{pmatrix}_L , \ \ell^-_R \right\} \ ; \ \left\{ \begin{pmatrix} q_u \\ q_{d'} \end{pmatrix}_L , \ (q_u)_R \, , \ (q_{d'})_R \right\} \tag{1.1.6}$$

and the structure is repeated for each of three generations, $\{\nu_{\mathrm{e}}, \mathrm{e}^-, \mathrm{u}, \mathrm{d}'\}$, $\{\nu_\mu, \mu^-, \mathrm{c}, \mathrm{s}'\}$ and $\{\nu_\tau, \tau^-, \mathrm{t}, \mathrm{b}'\}$ (and their antipartners), where $\{\mathrm{d}', \mathrm{s}', \mathrm{b}'\}$ are the quark weak eigenstates, rotated from the mass eigenstates $\{\mathrm{d}, \mathrm{s}, \mathrm{b}\}$ by the matrix $V_{CKM}$:

$$V_{CKM} \equiv \begin{pmatrix} V_{ud} & V_{us} & V_{ub} \\ V_{cd} & V_{cs} & V_{cb} \\ V_{td} & V_{ts} & V_{tb} \end{pmatrix} . \tag{1.1.7}$$

The diagonal elements of the matrix have values close to unity, and the off-diagonal entries are small.

The electroweak gauge group $\mathrm{SU}(2)_L \otimes \mathrm{U}(1)_Y$ gives rise to three boson fields $W^i$ associated with SU(2) of weak isospin, and to a single field $B$ associated with U(1), of which the gauge charge is the hypercharge $Y$. Owing to the non-Abelian nature of SU(2) the $W$ fields exhibit self-interaction analogously to the gluons of QCD. The covariant derivative is given by:

$$\mathcal{D}_\mu = \partial_\mu \delta_{ij} + ig(\mathbf{T} \cdot W_\mu)_{ij} + ig' B_\mu Y \tag{1.1.8}$$

and the physical states are identified as

$$W^\pm_\mu = \frac{1}{\sqrt{2}}(W^1_\mu \mp i W^2_\mu) \quad \text{and} \quad \begin{pmatrix} Z_\mu \\ A_\mu \end{pmatrix} = \begin{pmatrix} \cos\theta_W & -\sin\theta_W \\ \sin\theta_W & \cos\theta_W \end{pmatrix} \begin{pmatrix} W^3_\mu \\ B_\mu \end{pmatrix} . \tag{1.1.9}$$

QED is preserved by relating the couplings:

$$g \sin\theta_W = g' \cos\theta_W = e. \tag{1.1.10}$$

The charged-current and neutral-current parts of the Lagrangian may then be written in terms of the physical states as:

$$\mathcal{L}_{\mathrm{CC}} = \frac{e}{2\sqrt{2}\sin\theta_W} \{ W^+_\mu [\, \overline{q}_u \gamma^\mu (1-\gamma_5) q_d + \overline{\nu}_\ell \gamma^\mu (1-\gamma_5) \ell \,] + \text{h.c.} \} \ ,$$

$$\mathcal{L}_{\mathrm{NC}} = eA_\mu \sum_{\text{fermions } j} \overline{\psi}_j \gamma^\mu Q_j \psi_j \; + \; \frac{e}{\sin\theta_W \cos\theta_W} Z_\mu \sum_{\text{fermions } j} \overline{\psi}_j \gamma^\mu [T_3 - \sin^2\theta_W Q_j] \psi_j \; . \tag{1.1.11}$$

The last term is often written in terms of the vector and axial couplings $g_V = T_3 - 2Q\sin^2\theta_W$ and $g_A = T_3$.

The W and Z intermediate vector bosons were predictions of the unified electroweak theory, and the first observations of W and Z bosons in p$\overline{\mathrm{p}}$ collisions in 1983 [13] [14] provided validation of the theory.

**Standard Model Masses** The W and Z bosons are found to have masses $\sim 80\,\mathrm{GeV}/c^2$ and $\sim 91\,\mathrm{GeV}/c^2$ respectively. However the gauge symmetry of $\mathrm{SU}(2)\otimes\mathrm{U}(1)$ does not permit the addition of explicit mass terms of the form $m^2 W^\mu W_\mu$, and the Lagrangian as written predicts the W and Z to be massless.

A favoured solution is to introduce a term to the Lagrangian that preserves the gauge symmetry but allows the selection of a mass scale – so-called spontaneous symmetry breaking. The Higgs mechanism [2] introduces a complex doublet of scalar fields $\phi$ that couples to the $W$ and $B$ fields and adds a potential to the Lagrangian $V = \lambda(\phi^\dagger\phi)^2 - \mu^2\phi^\dagger\phi$, which for $\lambda, \mu^2 > 0$ has a non-zero minimum at $|\phi| = \sqrt{\mu^2/2\lambda} \equiv v/\sqrt{2}$. The resulting terms that are quadratic in the physical boson fields are

$$\mathcal{L}_{\mathrm{mass}} = \frac{g^2 v^2}{4} W^+_\mu W^{-\mu} + \frac{(g^2 + g'^2)v^2}{8} Z_\mu Z^\mu \quad , \tag{1.1.12}$$

giving the W and Z bosons the masses

$$m_{\mathrm{W}} = \frac{1}{2} v g \quad \text{and} \quad m_{\mathrm{Z}} = \frac{1}{2} v \sqrt{g^2 + g'^2} \equiv \frac{m_{\mathrm{W}}}{\cos\theta_W} \quad . \tag{1.1.13}$$

This mechanism predicts a physical neutral scalar particle, the Higgs boson, as yet unobserved; but not its mass.

Fermions also acquire masses through interaction with the Higgs field and in this case each mass is a free parameter. Fermion masses have the interesting property that they can be seen as a left-right transition, and in the minimal Standard Model the right-handed neutrino $\nu_R$ is absent. So in the framework of the Standard Model the recent evidence that neutrinos oscillate and hence have mass [8] is problematic.

**Feynman Diagrams** The scattering matrix for a particular process may be written as a perturbative series in a Hamiltonian $\mathcal{H}$ derived from the Lagrangians written above.

Feynman diagrams give a visual representation of the terms in the series, with 'external lines' representing the initial and final states, vertices representing the interactions and 'internal lines' and 'loops' representing intermediate particles. The higher the order of calculation desired, the larger the number of diagrams with different configurations of internal lines that can be drawn, however the more suppressed (in powers of the coupling constant) are their contributions. A calculation including all terms to order $\alpha_S$, compared to the lowest-order diagram, is referred to as 'next-to-leading order' (NLO) in QCD, and one containing all terms to order $\alpha_S^2$ referred to as 'next-to-next-to leading order' (NNLO).

**Renormalization** Couplings and fermion masses are written in the Lagrangians as parameters. However higher order loops may be viewed as modifiying a coupling, depending on whether a loop is taken along with the vertex or as part of the rest of the diagram; and analagously the extent to which a mass is 'shielded' by pairs of virtual particles depends on the scale of the probe. The redefinition of couplings and masses as being scale-dependent is known as renormalization. The technique makes it possible to treat infinities that are introduced by these virtual loops into perturbative calculations.

In QED the coupling $\alpha$ increases with $Q^2$, and the force has infinite range. However in QCD the self-interaction of the gluon results in an $\alpha_S$ that decreases with $Q^2$, the property known as asymptotic freedom. Thus at high $Q^2$ quarks may be treated as free particles and perturbation theory may be used for calculations, but at long distances the coupling is strong and quarks are not seen as free particles – they are confined. The running of $\alpha_S$ has been seen through its measurement at different scales in Deep Inelastic Scattering and in $e^+e^-$ and hadron collisions.

**Summary** The Standard Model has been described in terms of the gauge theories $SU(3)_C \otimes SU(2)_L \otimes U(1)_Y$ and, except for neutrino masses, shows good agreement with experiment. However the Standard Model is thought to be an effective low-energy theory, and searches are underway for evidence of physics beyond the Standard Model that may become manifest at higher scales, such as supersymmetry – a symmetry of bosons and fermions which predicts spectra of new particles; or extra dimensions – theories that would unite gravity with the strong and electroweak forces. As the Standard Model is an overconstrained system, one way of testing it is to make increasingly precise measurements of a variety of physical quantities with the aim of revealing inconsistencies in global fits of many measurements. This is the objective of part of the work presented here.

## 1.2. W/Z Production in $\mathrm{p\overline{p}}$ collisions

W and Z bosons are produced in $\mathrm{p\overline{p}}$ collisions at the Tevatron through the Drell-Yan process: at leading order via $\mathrm{q\overline{q}}$ annihilation as shown in Figure 1, and at higher orders with contributions from qg, qq and gg. Next-to-leading-order diagrams are shown in Figure 2. Any process that may be described by Z exchange may also be described by $\gamma^*$ exchange, and the two corresponding terms interfere. For the events in the region of the Z pole studied here, Z exchange is dominant. As the $Q^2$ of the process is very high the interacting parton content of the proton and antiproton is asymptotically free; this means that tree diagrams can be calculated perturbatively. However the initial state does consist of bound hadrons rather than of free quarks, so the measured cross-sections are sensitive to the quark distributions of the proton.

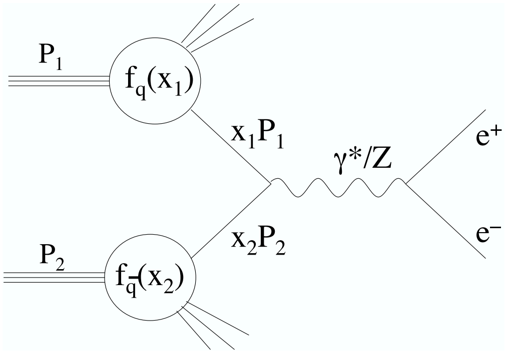

**Figure 1:** *Leading-order (parton model) Drell-Yan electron pair production.* $x_1$ *and* $x_2$ *are the momentum fractions of the incident proton and antiproton carried by the colliding quark and anti-quark.*

### 1.2.1 The Inclusive Cross-section $\sigma(\mathrm{p\overline{p}}\rightarrow\mathrm{Z})\cdot Br(\mathrm{Z}\rightarrow\mathrm{ee})$

At leading order the cross-section for Z production from quarks is given [3] by

$$\hat{\sigma}(\mathrm{q\overline{q}}\rightarrow\mathrm{Z}) = \frac{\pi}{3}\sqrt{2}\,G_F\,m_{\mathrm{Z}}^2\,(g_V^2+g_A^2)\,\delta(\hat{s}-m_{\mathrm{Z}}^2) \tag{1.2.1}$$

where $G_F$ is the Fermi constant and $g_V$ and $g_A$ are vector and axial couplings defined in the previous section. $\hat{s} = sx_1x_2$, where $s$ is the total centre-of-mass energy squared, and

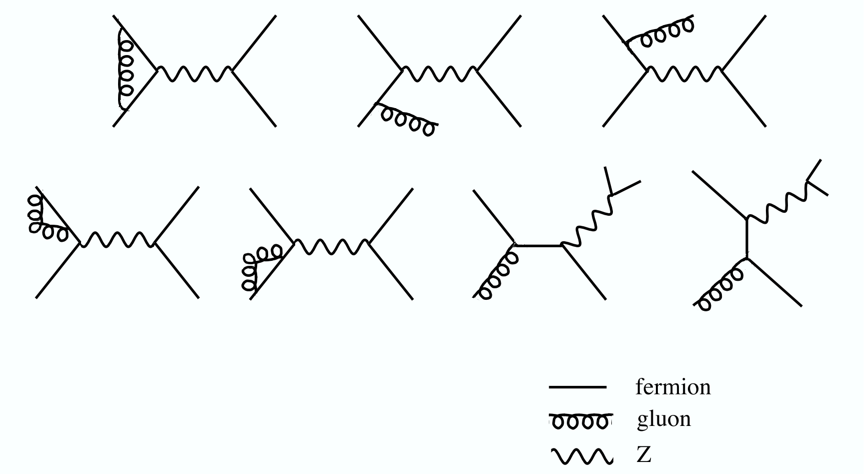

**Figure 2:** *Next-to-leading-order contributions to Drell-Yan electron pair production*

$x_1$ and $x_2$ are the momentum fractions of the incident proton and antiproton carried by the colliding quark and antiquark. The total cross-section is obtained by convolution with the parton density functions (PDFs) $f_q$, which are interpreted as the probability of finding a parton of given momentum fraction $x$ inside the proton:

$$\sigma_{\text{tot}}(\hat{s}) = \int dx_1 dx_2 \; \hat{\sigma}_{\text{Z}} \sum_q \{ f_q(x_1) f_{\overline{q}}(x_2) + (q \leftrightarrow \overline{q}) \} \quad . \tag{1.2.2}$$

The cross-section for a particular final state may be obtained by multiplying this total cross-section by final-state branching ratios.

The cross-section $\sigma(\text{p}\overline{\text{p}} \rightarrow \text{Z})$ has been calculated in full at next-to-next-to-leading-order (NNLO) in QCD. The QCD perturbation series is found to converge quickly: the NLO and NNLO contributions are respectively of the order of 16% and 2% of the LO cross-section. The branching ratio $Br(\text{Z} \rightarrow \text{ee})$ has been measured to high precision at LEP [51]. A measurement of $\sigma(\text{p}\overline{\text{p}} \rightarrow \text{Z} \rightarrow \text{ee})$ may therefore be seen as a test of the evolution of the PDFs from the scale at which they are measured in DIS data, $Q^2 \sim 10^{1-2}\text{GeV}^2$, to the scale of this process, $Q^2 \sim 10^4\text{GeV}^2$.

The first measurement presented in this thesis is the inclusive cross-section for Z production in proton-antiproton collisions at $\sqrt{s} = 1.96\,\text{TeV}$, observed in the electron decay channel using the Collider Detector at Fermilab (CDF). Experimentally, calorimeter and tracking information is used to select events with two high-$p_T$ electron candidates having invariant mass consistent with a Z. The cross-section is evaluated as

$$\sigma_{\mathrm{Z}/\gamma^*} \cdot Br(\mathrm{Z} \rightarrow \mathrm{e}^+\mathrm{e}^-) = \frac{N_{\mathrm{Z}}^{\mathrm{candidates}} - N^{\mathrm{background}}}{A_{\mathrm{Z}} \cdot \epsilon_{\mathrm{Z}} \cdot \epsilon_{trig} \cdot \epsilon_{zvertex} \cdot \int \mathcal{L}dt} \qquad (1.2.3)$$

where $N$ are numbers of candidate and background events, $A_{\mathrm{Z}}$ and $\epsilon_{\mathrm{Z}}$ are the kinematic and geometric acceptance, and identification efficiency, for the Zs; $\epsilon_{trig}$ is a trigger efficiency; $\epsilon_{zvertex}$ is a factor to correct for the events removed by a cut on the primary vertex of the event; and $\int \mathcal{L}dt$ is the integrated luminosity recorded by the experiment.

The Drell-Yan continuum cross-section ($\mathrm{p\overline{p}} \rightarrow \gamma^*$) has been measured by many experiments since the 1960s, and $\sigma(\mathrm{p\overline{p}} \rightarrow \mathrm{Z})$ by the UA1 and UA2 experiments in 1990. However only the Run I Tevatron experiments, at $\sqrt{s} = 1.8$ TeV, have made measurements at centre-of-mass energies close to the 1.96 TeV used for the measurements presented here; and those earlier measurements were much more limited by statistics than these new analyses.

### 1.2.2 The Cross-section Ratio $R$

In addition to measuring total inclusive cross-sections $\sigma(\mathrm{p\overline{p}} \rightarrow \mathrm{Z} \rightarrow \mathrm{ee})$ and $\sigma(\mathrm{p\overline{p}} \rightarrow \mathrm{W} \rightarrow \mathrm{e}\nu)$ it is of great interest to measure their ratio. The individual cross-section measurements may be designed such that many of the experimental uncertainties cancel in the ratio; in particular, the large luminosity uncertainty common to all cross-section measurements at the Tevatron.

The ratio may be expressed

$$R \equiv \frac{\sigma_{\mathrm{W}} \cdot Br(\mathrm{W} \rightarrow \mathrm{e}\nu)}{\sigma_{\mathrm{Z}} \cdot Br(\mathrm{Z} \rightarrow \mathrm{ee})} = \frac{\sigma_{\mathrm{W}}}{\sigma_{\mathrm{Z}}} \frac{\mathit{\Gamma}(\mathrm{W} \rightarrow \mathrm{e}\nu)}{\mathit{\Gamma}(\mathrm{Z} \rightarrow \mathrm{ee})} \frac{\mathit{\Gamma}(\mathrm{Z})}{\mathit{\Gamma}(\mathrm{W})} \quad . \qquad (1.2.4)$$

The ratio of the total cross-sections and the partial width $\mathit{\Gamma}(\mathrm{W} \rightarrow \mathrm{e}\nu)$ are calculable in the Standard Model, and the total width of the Z and the leptonic branching ratio $\mathit{\Gamma}(\mathrm{Z} \rightarrow \mathrm{ee})/\mathit{\Gamma}(\mathrm{Z})$ are well-measured from LEP [51]. A measurement of the cross-section ratio may thus be used to extract an indirect measurement of the total width $\mathit{\Gamma}(\mathrm{W})$. The total width is very sensitive to any non-Standard Model decay of the W – for example, before the observation of the top quark it was used to set a lower bound on the top quark mass. A measurement of $R$ and of $\mathit{\Gamma}(\mathrm{W})$ is thus a sensitive test of the Standard Model.

### 1.2.3 The Differential Cross-section $d\sigma/dy$

It is important to understand not only inclusive cross-sections, but also their behaviour in a variety of kinematic variables. Cross-sections of boson production differential with respect to invariant mass, boson transverse momentum and boson rapidity have been studied in the past, each with a slightly different emphasis. The mass distribution has been used as a way of searching for new physics, and the $p_T$ distribution to test the modeling of soft QCD initial-state radiation. The rapidity distribution has been used to test and constrain PDFs, and is also key for event generator parameter tuning. Currently the Run I rapidity measurement is used by CDF to tune PYTHIA [24], and a better measurement from Run II will result in lower systematic uncertainties on measurements such as total cross-sections, the forward-backward asymmetry $A_{fb}$, and precision mass measurements $m_W$ and $m_t$.

PDFs are principally measured through deep inelastic scattering (DIS) [7] of leptons and hadrons, with the unknown structure measured from the energies and angular distributions of the scattered lepton. However other measurements such as $d\sigma/dy$ [9] and the W charge asymmetry measured at CDF [10] are complementary to the DIS measurements in the range of $x$ and $Q^2$ that they cover, and collaborations such as CTEQ [11] and MRST [12] combine many different measurements into global QCD fits. It is envisaged that a new determination of $d\sigma/dy$ from Run II of the Tevatron will be incorporated into future versions of such fits.

Rapidity $y$ is defined

$$y \equiv \frac{1}{2} \ln \frac{E + p_z}{E - p_z} \tag{1.2.5}$$

and has the property of invariance under Lorentz boosts. It follows from this definition that for the Drell-Yan process at leading order as shown in Figure 1, the momentum fractions $x$ of the interacting partons in the proton are directly related to the rapidity:

$$x_{1,2} = \frac{m}{\sqrt{s}} e^{\pm y} \tag{1.2.6}$$

where $m$ is the mass of the dielectron pair and $s$ the centre-of-mass energy. The production of Zs at high rapidity therefore involves the interaction of a parton at high $x$ and one at low $x$, and a particular interest of measuring $d\sigma/dy$ is to use the high rapidity region to probe low-$x$ distributions that are not very well-known. Additionally the contribution of gluon diagrams at orders higher than leading order gives some sensitivity to the gluon distributions, which are also not well-known.

Experimentally $d\sigma/dy$ is measured by evaluating each quantity of Eqn 1.2.3 in bins of rapidity. As the calorimeteric coverage of CDF is much greater than the coverage of the muon chambers, the electron channel is ideally suited to this measurement.

## 1.3. Thesis Outline

The Tevatron accelerator complex, the detectors used to collect the collision data and the datasets used in the analyses presented here are described in Chapter 2. In Chapter 3 the geometric and kinematic acceptances of the detector are studied, and in particular the benefit of including the forward detectors is shown. Chapter 4 discusses the measurement of backgrounds and of efficiencies associated with the trigger, with electron reconstruction, and with the electron identification requirements made on top of the geometric and kinematic selection in order to reduce backgrounds. Finally the measurements of $\sigma \cdot Br(p\overline{p} \rightarrow \mathrm{Z} \rightarrow \mathrm{ee})$, $R = \sigma(\mathrm{W})/\sigma(\mathrm{Z})$, and $d\sigma(p\overline{p} \rightarrow \mathrm{Z} \rightarrow \mathrm{ee})/dy$ are presented and discussed in Chapter 5.

# Chapter 2

# Accelerator, Detector and Datasets

The measurements presented here are performed on data collected by the Collider Detector at Fermilab (CDF), a multi-purpose experiment that records proton-antiproton collisions in the Tevatron accelerator. In this chapter elements of the detector and the accelerator complex are described, and also the datasets used in the analyses.

## 2.1. Accelerator

There are five stages in the accelerator chain at Fermilab. $H^-$ ions are accelerated to 750 keV in the Cockcroft-Walton accelerator and fed into the linear accelerator to be brought to 400 MeV. At this stage the ions are passed through a carbon foil in order to remove the electrons, and the resulting protons are accelerated to 8 GeV and bunched in the Booster. Subsequently the Main Injector takes the protons to 150 GeV, and finally the Tevatron accelerates them to 980 GeV. The accelerator complex is shown in Figure 3.

Antiprotons are generated by sending 120 GeV protons from the Main Injector to a nickel target. From the resulting shower of particles, antiprotons of around 8 GeV are selected and sent to the Debuncher and Accumulator Rings where they are stochastically cooled. Once a 'stack' has been collected the antiprotons are sent back to the Main Injector, accelerated to 150 GeV and put into the Tevatron, circulating counter to the proton bunches. Currently 36 bunches each of protons and antiprotons are collided with a separation of 396 ns.

Once both beams are at the maximum energy they are focused and brought to collision with centre-of-mass energy $\sqrt{s} = 1.96$ TeV at two interaction points, one of which is at the centre of the CDF detector. The luminous region has a Gaussian dispersion of around 30 $\mu$m transverse to the beam direction, and a length along the beam directions of around 30 cm.

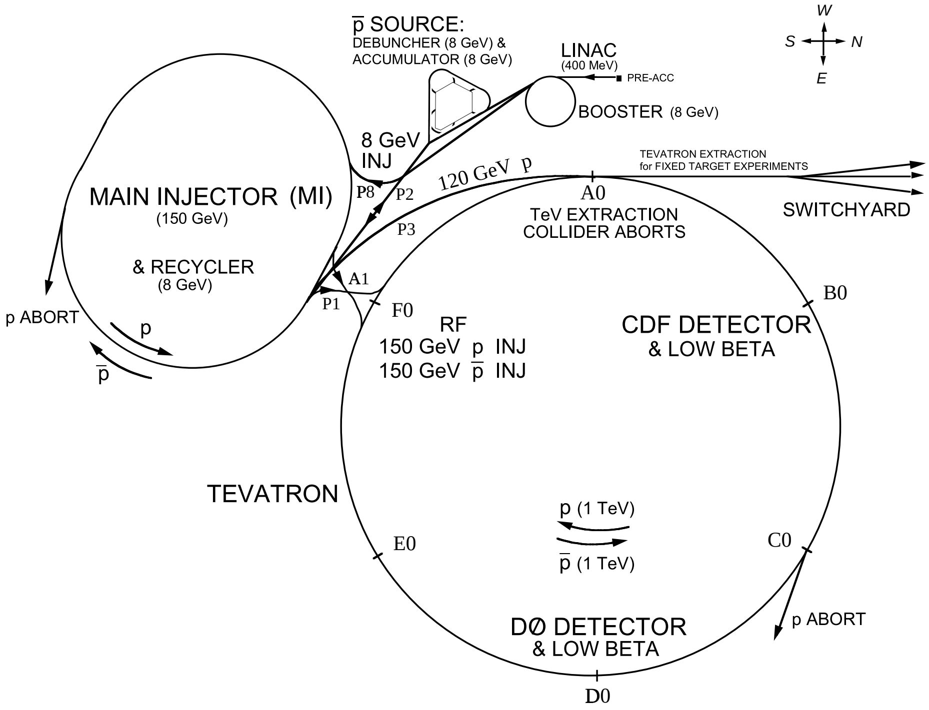

**Figure 3:** *The Fermilab accelerator complex.*

Parts of the Fermilab accelerator complex are 20 years old and there have been some setbacks since the upgrades to take the Tevatron from 1.8 TeV to 1.96 TeV, such as inefficiencies in the transfer lines that can lead to antiprotons being lost; the lack of performance of the recycler, which should have reclaimed antiprotons from the Tevatron; and the cancellation of the proposed reduction in bunch spacing from 396 ns to 132 ns. However the initial instantaneous luminosity of stores has been steadily increasing, recently reaching $10^{32}$ cm$^{-2}$s$^{-1}$, and the rate of integrated luminosity delivery has also been increasing so that as of September 2004 CDF had on tape around 350 $\mathrm{pb}^{-1}$ of physics-quality data: more than double the integrated luminosity collected during Run I.

## 2.2. Detector

The CDF detectors are arranged cylindrically around the interaction point. Closest to the beamline are layers of silicon, providing high-precision tracking and vertexing. Next is a wire drift chamber for track reconstruction, positioned inside a solenoid and surrounded by electromagnetic then hadronic calorimeters. Finally there is a muon system. The layout of these detectors is shown in Figure 4, which depicts one quadrant of the cross-section through the detector.

In the following sections, parts of the detector used in these measurements are discussed in more detail, along with the trigger system used to filter interesting events to be written to tape for later analysis.

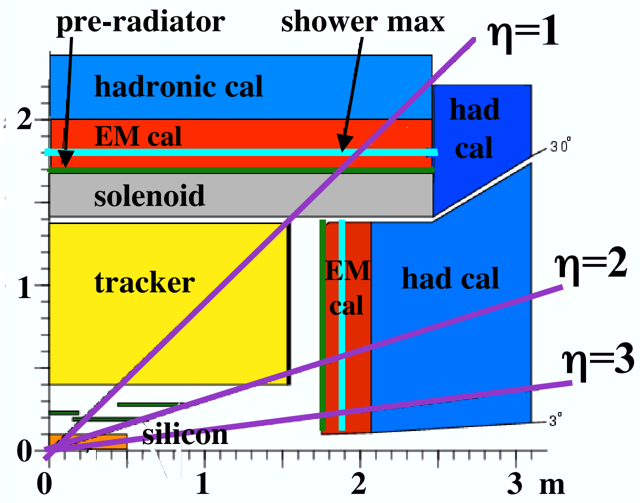

**Figure 4:** *The CDF Detector (a quadrant of the yz plane as defined in Figure 5). Muon chambers are positioned round the hadronic calorimeters.*

### 2.2.1 Coordinate System and Transverse Quantities

Positions are measured at CDF using a cylindrical coordinate system $(\theta, \phi, z)$ with origin at the nominal interaction point, as illustrated in Figure 5. $z$ is the proton direction at the interaction point (east) and $\phi$ is measured in the $xy$ plane up from $x$, which is defined as the direction out from the centre of the Tevatron ring. Figure 4 shows angular values measured in the pseudorapidity variable $\eta$, which is defined as

$$\eta \equiv -\log\left(\tan\frac{\theta}{2}\right). \tag{2.2.1}$$

In the limit of massless particles, pseudorapidity equals rapidity as defined in Eqn 1.2.5.

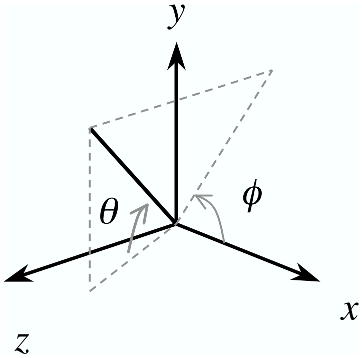

**Figure 5:** *The CDF coordinate system.*

A useful measure of separation between two objects in the detectors is the conical separation $\Delta R$, defined through

$$(\Delta R)^2 = (\Delta\eta)^2 + (\Delta\phi)^2. \tag{2.2.2}$$

Reference will be made to the components of physical quantities measured perpendicularly to the beamline, 'transverse' energy and momentum $E_T$ and $p_T$. These are defined as $E\sin\theta$ and $p\sin\theta$ respectively, although in some cases to be discussed later $\theta$ is redefined with respect to the event interaction vertex rather than the origin of the coordinate system.

### 2.2.2 Tracker

CDF uses silicon strip detectors and a drift chamber for charged-particle track reconstruction and vertex finding. The tracking systems are inside a superconducting solenoid of radius 1.5 m that provides a 1.4 T magnetic field parallel to the beam axis. Both the silicon system and the drift chamber were redesigned and completely rebuilt between Run I and Run II of the Tevatron.

**Silicon (SVX, Layer00, ISL)** As charged particles move through the 'depletion layer' created in a biased $p-n$ semiconductor junction, they create electron-hole pairs that drift to be collected at the surfaces.

The CDF silicon system consists of five layers of double-sided silicon strips comprising the 'Silicon Vertex Detector' (SVX). The stereo sides are alternately small-angle and 90°, and the detectors are positioned between 2 cm and 11 cm from the beampipe. An additional single-sided layer of silicon ('Layer00') is mounted on the beampipe. Further from the beam, a layer of silicon is placed at 22 cm in the central region $|\eta| < 1$, and two layers at 20 cm and 28 cm in the region $1 < |\eta| < 2$. These layers comprise the 'Intermediate Silicon Layers' (ISL).

Owing to beam accidents and to operating conditions that resulted in wire jumpers resonating and breaking, around 12% of the z-side chips and 5% of the r-$\phi$ chips have been lost and accurate modeling of the silicon system's acceptance is complicated. For this reason and given the relative purity of the $Z \rightarrow ee$ samples, the silicon systems are used only in the reconstruction of very forward Z bosons, which are not used in all parts of the analyses.

**Drift Chamber (COT)** Drift chambers use electric fields to direct the ions created by the passage of charged particles through a gas towards sense wires that can be read out to give a precise position measurement.

The central outer tracker (COT) [15] is a 3 m long open-cell drift chamber that extends between 40 cm and 132 cm from the beampipe. Sense wires and potential wires are alternated and arranged in 8 'superlayers' as shown in Figure 6, each consisting of 12 layers of sense wires. Superlayers are alternately axial, and ±2° stereo. Within each superlayer are 'cells', bounded by field-shaping sheets. The cells are angled at 35° to the radial direction to compensate for the Lorentz angle of the drifting charged particles. There is a 'spacer' at $z = 0$ that results in a lower tracking trigger efficiency at $\eta = 0$. The chamber is filled with a mixture of argon, ethane and a small amount of alcohol. Recently this was supplemented with a small amount of oxygen, which was found to reverse aging that had been observed in the inner superlayers of the chamber.

The tracking resolution is given in Table 1 along with the resolutions of other detectors used in these analyses. Tracks can be reconstructed in the COT up to $|\eta| \sim 1$.

### 2.2.3 Calorimeters

As charged particles progress through the calorimeters they interact and develop charac-

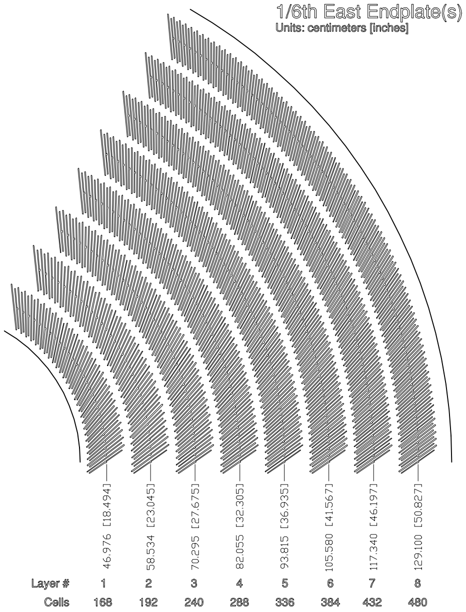

**Figure 6:** *Superlayers of the COT, showing the tilt of the cells. Even-numbered layers are axial; odd layers are stereo.*

teristic 'showers'. Whereas electrons and photons shower quickly and are largely contained in the electromagnetic calorimeter, hadron jets pass through and leave significant energy in the hadronic calorimeters.

As may be seen from Figure 4, CDF's calorimeters are physically separated into two sections: the central region, cylindrical about the beamline and covering $|\eta| < 1$; and the forward regions or 'end plugs', covering $1.1 < |\eta| < 3.6$. The principal components of the central calorimeter are the central electromagnetic (CEM) and central hadronic (CHA) compartments. Both the CEM and CHA are retained from Run I.

**Central Electromagnetic Calorimeter (CEM, CES, CPR)** The central electromagnetic calorimeter (CEM) [16] is constructed in 15° wedges placed outside the solenoid and consists of 31 layers of polystyrene scintillator interleaved with layers of lead clad in aluminium. The sheets are stacked in a projective tower geometry, as shown in Figure 7, where each tower subtends 15° in $\phi$ and 0.1 in $\eta$. It can be seen that in each wedge 'tower 9' is truncated; this will be important later in defining electron fiduciality. At higher $z$ some of the lead is replaced by plastic in order that the effective radiation depth be approximately independent of angle. Light is fed through waveshifters and collected in phototubes as indicated in Figure 7.

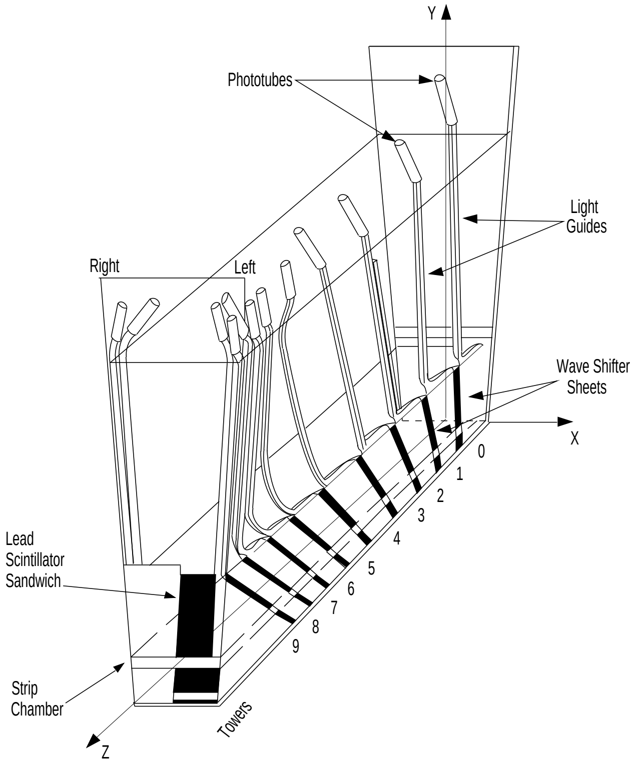

**Figure 7:** *A wedge of the central calorimeter, showing the projective tower geometry.*

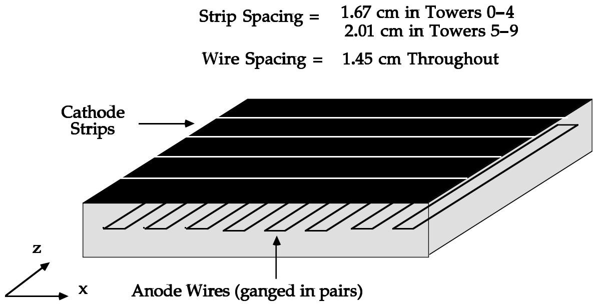

**Figure 8:** *A central shower-max chamber shown schematically.*

After the eighth layer of lead, corresponding to the depth at which showers typically reach their maximum transverse extent, is the central shower-maximum (CES) detector. This consists of proportional chambers as shown in Figure 8 that give good position resolution.

A further component of the central calorimeters is the central pre-radiator (CPR), a set of proportional chambers between the CEM and the magnet designed to help separate electrons and pions.

Detector resolutions are given in Table 1.

**Central and Wall Hadronic Calorimeters (CHA, WHA)** The central hadronic calorimeter (CHA) [17] is immediately on top of the CEM and consists of steel layers sampled each 2.5 cm by scintillator. Filling a space between the CHA and the forward plug hadronic calorimeter (PHA) is the wall hadronic calorimeter (WHA), which continues the tower structure of the CHA but with reduced sampling each 5.0 cm. Like the electromagnetic calorimeters, the hadronic calorimeters are read out using waveshifting lightguides and phototubes.

**Plug Electromagnetic Calorimeter (PEM, PES, PPR)** The plug electromagnetic calorimeter (PEM) was newly built for CDF Run II [18]. Like the CEM, the PEM consists of a stack of lead and scintillator sheets read out by phototubes. At lower values of $\eta$ the tower segmentation is $7.5^\circ$ in $\phi$, doubling to $15^\circ$ at higher $\eta$ as shown in Figure 9, which also gives the $\eta$ segmentation. A 30 GeV electron shower will be largely contained in four of the towers at lower $\eta$.

Approximately 6 radiation lengths into the PEM is a shower-maximum detector, the PES, designed to provide good position measurement. It consists of two layers of scintillator strips at $45^\circ$ to each other, assembled in $45^\circ$ sectors.

Finally, the first layer of the PEM is read out separately and referred to as the plug preradiator (PPR). The PPR can help to distinguish between electrons/photons and hadrons by indicating the extent to which the particle shower has already developed at the face of the calorimeter.

**Plug Hadronic Calorimeter (PHA)** The plug hadronic calorimeter (PHA) consists of layers of iron and scintillator, extending back from and maintaining the same segmentation as the PEM.

#### 2.2.3.1 Electron Clustering

At the Level-2 trigger, Level-3 trigger and offline, calorimeter towers are clustered to give electron and photon candidates. The triggers will be discussed further in Section 2.2.5.

At Level-2 the central calorimeters are simplified into a $24 \times 24$ grid in $\eta$ and $\phi$, and starting from a seed tower, clusters are expanded recursively into adjacent towers that have energy greater than a certain threshold. For high-$p_T$ electron triggers the seed tower is

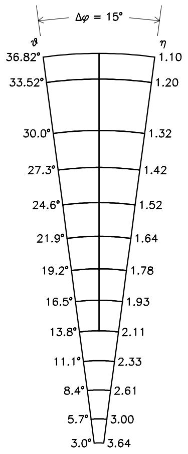

**Figure 9:** *Forward detector segmentation.*

required to be 8 GeV and the shoulder-tower 7.5 GeV, which is relatively high and leads to a loss in efficiency at Level-2; but is necessary to control trigger rates. A more sophisticated algorithm has been developed for Level-2 clustering that allows a lower shoulder-tower threshold, and that will soon be implemented for the high-$p_T$ electron triggers.

At Level-3 and offline the algorithms are more complex [30]. Towers are ordered in EM $E_T$ and the highest EM $E_T$ tower that has not yet been clustered is taken as a seed. In the CEM, available shoulder towers are added to the cluster if they are adjacent in $\eta$ to the seed (although offline, clusters are restricted to two towers and not three).

At Level-3 in the PEM, available shoulder towers are added to the cluster if they are adjacent in $\eta$ or $\phi$ to the seed. Unlike at Level-2, the shoulder-tower threshold is very low (100 MeV), and there is no simplification of the tower structure. A cluster is accepted if the ratio of hadronic to electromagnetic energy $Had/EM$ is less than 0.125, or if the electromagnetic energy is greater than 100 GeV.

Offline in the PEM the BF_CLUSTERING algorithm considers all towers with $E_T >$ 100 MeV. Taking as seed tower the highest $E_T$ tower not already assigned to a cluster, the algorithm adds to it the tower with the highest EM $E_T$ that shares a border with the seed tower. Then the highest EM $E_T$ pair of towers that shares borders with those two seed and shoulder towers is added, so that the size of the resulting cluster is $2 \times 2$ towers.

### 2.2.3.2 Calorimeter Calibrations and Corrections

Radioactive sources are built in to the central and forward calorimeters and are pulled across the calorimeters several times each year, during accelerator shutdowns, to calibrate the detectors. As frequently as each day, between stores, laser systems are used to provide relative calibrations across the calorimeters. In addition medium- and high-$p_T$ electron candidates ($> 8\,\mathrm{GeV}$) are monitored offline – in particular the distribution $E/p$, the ratio of electromagnetic energy to track momentum in the central region. Given stable track reconstruction this can pinpoint towers that have drifting gains. In the forward region where tracking is not available, minimum bias events provide high statistics and are used in addition to the lasers and sources to monitor the relative tower calibrations. The reconstructed mass of Z events in which one electron is reconstructed in the forward region provides an absolute scale, although statistics are more limited.

Combining the above methods provides 'tower-to-tower' corrections and time-dependent corrections. Online calibrations used by the trigger system are updated from time to time, and residual corrections are made offline.

The calorimeter response also varies within each wedge, and 'face corrections', determined from mapping the response across the wedge in a testbeam [19], are applied after the data have been processed offline.

Finally, for these analyses the PPR energy is added in to the PEM energy offline and further overall scale corrections are made to the forward calorimeter energies, as described in Section 3.2.1.

| Detector System | Resolution |
|---|---|
| COT | $\sigma(p_T)/p_T \sim 0.15\% \cdot p_T$ [GeV/$c$] |
| CEM | $\sigma(E)/E \sim 13.5\%/\sqrt{E_T}$ [GeV] |
| CHA | $\sigma(E)/E \sim 50\%/\sqrt{E}$ [GeV] |
| CES | 2 mm at 50 GeV |
| PEM | $\sigma(E)/E \sim 14.4\%/\sqrt{E}$ [GeV] $\oplus$ 0.7% |

**Table 1:** *Detector resolutions.*

### 2.2.4 Muon Chambers

Muons act as minimum-ionising particles in the calorimeters, and are detected in sets of drift chambers outside the calorimeters. Similarly to the stereo layers of the silicon system and central tracker, alternating layers of the chambers are staggered. A muon candidate consists of a 'stub' of hits recorded in the muon chambers, matched to a COT track. The central muon system (CMU) and central muon upgrade (CMP) cover $|\eta| < 0.6$; the central muon extension (CMX) covers $0.6 < |\eta| < 1.0$; and the barrel muon system (BMU) is still under commissioning and covers $1.0 < |\eta| < 1.5$. In the CMU, each $15^{\circ}$ wedge contains three chambers. The muon systems are not used directly in these analyses, although a final combination of the electron and muon channel measurements of the Z cross-section and W and Z cross-section ratios will be given in Chapter 5.

### 2.2.5 Trigger

The event rate is such that it is necessary to filter physically interesting events to be written to tape, and this is achieved through a three-level trigger system, designed to be 'deadtimeless'.

The Level-1 trigger is in hardware. There are three parallel processing streams finding calorimeter objects, muons and tracks respectively, which may be combined with AND and OR to give 64 triggers. At Level-1, calorimeter objects consist of single tower energies, tracks are 2-dimensional as found by the eXtremely Fast Tracker (XFT) which compares COT hits to look-up tables; and muons consist of a 'stub' in the muon chambers matched to a track within $2.5^{\circ}$ in $\phi$. The input rate of 2.5 MHz is reduced by the Level-1 trigger to $\sim$30 kHz.

Level-2 is also in hardware. Basic calorimeter clustering can be carried out at Level-2 as mentioned in Section 2.2.3.1, and shower maximum information added. Silicon tracking information is also available. The Level-2 output rate is $\sim$350 Hz.

Level-3 consists of the event builder (EVB) and the Level-3 farm. The EVB assembles event fragments from Level-1 and Level-2 into complete events, and then the Level-3 farm runs a version of the full offline reconstruction code. This means that for example fully-reconstructed 3-dimensional tracks are available to the trigger decision. The Level-3 output rate is $\sim$75 Hz and accepted events are written to tape in eight separate 'streams', sorted by trigger, by the Consumer-Server Logger (CSL).

### 2.2.5.1 Electron and Jet Triggers

Each trigger is composed of Level-1, Level-2 and Level-3 'paths'. The principal electron trigger used in these analyses is ELECTRON_CENTRAL_18, summarised in Table 2. The Level-1 path is L1_CEM8_PT8; that is, to pass the trigger an event must contain a single tower in the CEM that has $E_T > 8\,\mathrm{GeV}$ and is matched to an XFT track with $p_T > 8\,\mathrm{GeV}/c$. If the tower has $E_T < 14\,\mathrm{GeV}$ it must also have the ratio of hadronic to electromagnetic energy $Had/EM < 0.125$. The Level-2 requirement is L2_CEM16_PT8, so the calorimeter cluster formed at Level-2 must have $E_T > 16\,\mathrm{GeV}$. The Level-3 path is L3_ELECTRON_CENTRAL_18, which requires an 18 GeV central electromagnetic calorimeter cluster that has $Had/EM < 0.125$ and is matched to a Level-3 track having $p_T > 9\,\mathrm{GeV}/c$.

| | ELECTRON_CENTRAL_18 |
|---|---|
| L1 | CEM cluster, $E_T > 8\,\mathrm{GeV}$ and XFT track, $p_T > 8\,\mathrm{GeV}/c$<br>($Had/EM < 0.125$ for $E_T < 14\,\mathrm{GeV}$) |
| L2 | CEM cluster, $E_T > 16\,\mathrm{GeV}$ and XFT track, $p_T > 8\,\mathrm{GeV}/c$ |
| L3 | CEM cluster, $E_T > 18\,\mathrm{GeV}$ and COT track, $p_T > 9\,\mathrm{GeV}/c$<br>($Had/EM < 0.125$) |

**Table 2:** ELECTRON_CENTRAL_18 *trigger requirements.*

This principal trigger is supported by backup triggers that allow the trigger efficiencies to be measured; this will be discussed in Chapter 4.

For Z bosons at high rapidity, the Z_NOTRACK trigger is used, which requires an 8 GeV electromagnetic cluster at Level-1, and two electromagnetic clusters, each with 16 GeV at Level-2 and 18 GeV at Level-3. The clusters may be anywhere in the detectors and no track requirement is made.

Another class of triggers used in these analyses are the jet triggers. The differences between the trigger levels are again in the cluster-finding algorithm and the corresponding thresholds; so for example the trigger JET_20 consists of L1_JET5_PS20, L2_JET15_PS25 and L3_JET20. As the clustering increases in sophistication through the trigger levels, a higher energy threshold can be applied. PS indicates 'prescale' and is used to limit the rate of high-rate triggers: PS20 means that only one triggered event in 20 will be passed to the next trigger level.

## 2.3. Electron Reconstruction

Clustering in the electromagnetic calorimeters has already been discussed in Section 2.2.3.1. However electron candidates consist not only of an electromagnetic cluster, but also of associated pre-radiator and shower-maximum clusters, and – in the central region – tracks.

First an attempt is made to associate a track with the candidate cluster, if it is reconstructed in the CEM [30]. Each track of the event is extrapolated to the plane of the CES (assuming a helical path). Of the set of tracks coming within 25 cm in $x/\phi$ and 38 cm in $z$ of the seed-tower centre, the track that is associated with the cluster is the one that has the highest $p_T$ and is located not more than 5 cm from the seed-tower boundary.

CES and CPR clusters are associated with the CEM cluster if they are reconstructed in the same wedge. The 'best-matching' CES cluster is the one seeded by the track described above. PES clusters are associated with PEM clusters if they come within 10cm of each other in the plane of the PES.

Although the reconstruction run in the Level-3 farms is largely complete, events that have been written to tape are reprocessed before final physics analysis to take advantage of the most recent reconstruction code and calibrations, which are not available at Level-3.

During 2002 and 2003 there were many new software and calibration releases, and much time had to be spent keeping up-to-date with the latest versions of the data.

Important information for high-$p_T$ electrons that becomes available offline is a beamline measurement. The beamline is measured for each run or groups of runs by vertex-fitting large numbers of tracks from unbiased triggers. It can then be regarded as an extra constraint for track-finding, and tracks may be refitted offline to include the extra point. This is known as 'beam-constraining' and is used for all the central electron candidates in these analyses.

A final modification that takes place even after the reprocessing of the data is the recalculation of transverse quantities with respect to the event vertex. For $\mathrm{Z} \rightarrow \mathrm{ee}$ events, the event vertex is taken to be defined by the highest $p_T$ central electron track, and $E_T$ and $p_T$ are recalculated accordingly.

## 2.4. Simulation

A detector simulation is crucial for understanding detector acceptances and in many cases for modeling backgrounds. The CDF simulation parameterizes the detector geometry and material using GEANT 3 [20], tuned from testbeam and collision data. The kinematics of physical processes are reproduced to a certain order of calculation by a Monte Carlo generator program such as PYTHIA or HERWIG, which also implement parton showering to model initial- and final-state radiation and hadronisation. The generator gives a set of four-vectors that may be stepped through the CDF simulation, interacting and depositing energy in a realistic manner.

The simulation produces data banks from each subdetector identical to those from collision data, and the simulated data are analysed using the same code as the collision data. The truth variables from the event generator are also stored, and the understanding of the detectors and data may therefore be investigated by comparing the simulated and collision data.

## 2.5. Luminosity

The total integrated luminosity recorded by the experiment is determined from the rate of inelastic $\mathrm{p\overline{p}}$ interactions, measured using Cherenkov detectors. There is a Cherenkov luminosity counter (CLC) [21] at each side of the detector, and each consists of a set of 48 long, conical counters arranged in three rings around the beamline.

The luminosity $\mathcal{L}$ is evaluated as

$$\mathcal{L} = \frac{R_{\mathrm{p\overline{p}}}}{\epsilon_{CLC} \cdot \sigma_{\text{inelastic}}}, \tag{2.5.1}$$

where $R_{\mathrm{p\overline{p}}}$ is the measured rate, $\epsilon_{CLC}$ is the CLC detector acceptance, and $\sigma_{\text{inelastic}}$ is the total inelastic cross-section, measured in Run I at $\sqrt{s} = 1.8\,\text{TeV}$ by CDF and by the E811 experiment at the E0 interaction point [22], and scaled to $\sqrt{s} = 1.96\,\text{TeV}$.

A 6% uncertainty is assigned to the cross-section, coming equally from $\epsilon_{CLC}$ and from $\sigma_{\text{inelastic}}$. The CDF and E811 measurements of the total inelastic cross-section are not in good agreement, which leads to the large uncertainty in that number.

## 2.6. Datasets

The datasets used in these analyses are defined by their Level-3 trigger for collision data, and by the generated process for simulated data.

**Collision Data** The electron dataset used in these analyses is made by taking the raw datasets containing the high-$p_T$ electron trigger (`bhel08` and `bhel09`) and making the further requirement that there be two electron candidates with $E_T > 15\,\mathrm{GeV}$. Only events passing the ELECTRON_CENTRAL_18 or Z_NOTRACK triggers are used for analysis. In addition a 'good run' requirement is made that calorimetry, tracking and muon systems are certified to have been fully working [23].

The jet datasets used correspond to the same runs as the electron dataset, but collected from the appropriate jet trigger: JET_20, JET_50 or JET_100 (`gjet0a` and `gjet09`).

All the data are processed using version 4.8.4 of the CDF offline software. The code is always being improved and a significant update to calorimeter calibrations was made available from version 5.3.1; hence in addition to the main processing with 4.8.4, calorimetry objects only are remade using version 5.3.1.

Two distinct datasets are used in different parts of these analyses, consisting of $194\,\mathrm{pb}^{-1}$ collected between March 2002 and June 2003 – used in the measurement of the total cross-section and $\frac{d\sigma}{dy}$ – and its subset of $72\,\mathrm{pb}^{-1}$ collected up until January 2003, used in the measurement of $R$ (Eqn. 1.2.4). The smaller dataset is used in order to match the W cross-section measurement. For the very forward events only $191\,\mathrm{pb}^{-1}$ is available as the Z_NOTRACK trigger was not included in the earliest runs.

**Simulated Data** Monte Carlo data are used to check understanding of the detectors and for the study of detector acceptance. Datasets were generated and simulated using version 4.9.1 of the CDF offline software, tuned for the electroweak group. Version 4.9.1 has the same reconstruction as version 4.8.4, used for the data. The principal signal dataset consists of 500,000 Drell-Yan events, $\mathrm{p\overline{p}} \rightarrow \mathrm{Z}/\gamma^* \rightarrow \mathrm{ee}$, generated by PYTHIA (`zewk1e`). Backgrounds are investigated using 500,000 PYTHIA $\mathrm{W} \rightarrow \mathrm{e}\nu$ events (`wewk7e`) and 500,000 PYTHIA $\mathrm{Z}/\gamma^* \rightarrow \tau\tau \rightarrow \mathrm{ee}\nu\nu\nu\nu$ events (`zewk1t`). Systematic studies on the amount of material in front of the calorimeters, as described in Section 3.2.2, are made using datasets generated with $\pm 1\sigma$ material count in the central region (`zewk3e` and `zewk4e`) and $\pm 1\sigma$ material count in the forward region (`zewk7e` and `zewk8e`).

# Chapter 3

# Acceptance

The fraction of Z events produced in collisions that is observed in the dataset is evaluated as the product of two components: acceptance×efficiency. The acceptance is defined as the effect of geometric and kinematic cuts and is determined using the simulation, while the efficiency accounts for the effects of trigger requirements, electron reconstruction and electron selection criteria, and is measured directly from the data. In this chapter the determination of the acceptance and its associated systematic uncertainties is presented, and in particular the extra coverage coming from the forward detectors is discussed. The acceptance for $\mathrm{W} \to \mathrm{e}\nu$ events is also summarised before determining the systematics on the ratio of W to Z acceptances, which is needed to calculate the ratio of cross-sections.

The efficiencies will be discussed in Chapter 4.

## 3.1. Acceptance for $\mathrm{Z} \to \mathrm{ee}$ Events

The acceptance is measured by applying the geometric and kinematic cuts developed for the analysis to events generated by PYTHIA[24] and passed through the full detector simulation. The acceptance is binned in rapidity to be used directly in the evaluation of $d\sigma/dy$. For the total acceptance, as needed for the inclusive cross-section measurement, the binned acceptance is convolved with a full NNLO calculation of $d\sigma/dy$.

The geometric requirements on selected events are that two electron candidates are identified in either the central ($|\eta| < 1$) or forward regions of the detector. Events in which both electrons are reconstructed in the central region of the detector are referred to as central-central (CC), events with one central and one forward electron are referred to as central-forward (CF), and events in which both electrons are forward are referred to as forward-forward (FF). The three classes of events are shown schematically in Figure 10. Owing to low tracking efficiency in the forward region, forward-forward events are not included in all results and therefore in what follows, forward-forward events are dealt with somewhat separately from central-central and central-forward events. Central electron candidates are required to be in the fiducial region defined by the CES, which is within 21 cm of a calorimeter tower centre in the $r-\phi$ plane, and in the region $9\,\mathrm{cm} < |z_{\mathrm{CES}}| < 230\,\mathrm{cm}$, where $z_{\mathrm{CES}}$ is the $z$-coordinate measured by the CES. Candidates are excluded if their seed tower lies in the outer annulus of the central calorimeter ('tower 9' as described in Section 2.2.3 and Figure 7); and the small uninstrumented 'chimney' region of the central calorimeter that gives access for solenoid cryogenics, is also excluded. A fiducial requirement is made on forward electron candidates that their seed tower lies in the region $1.2 < |\eta| < 2.8$, in order to exclude detector edge-effects.

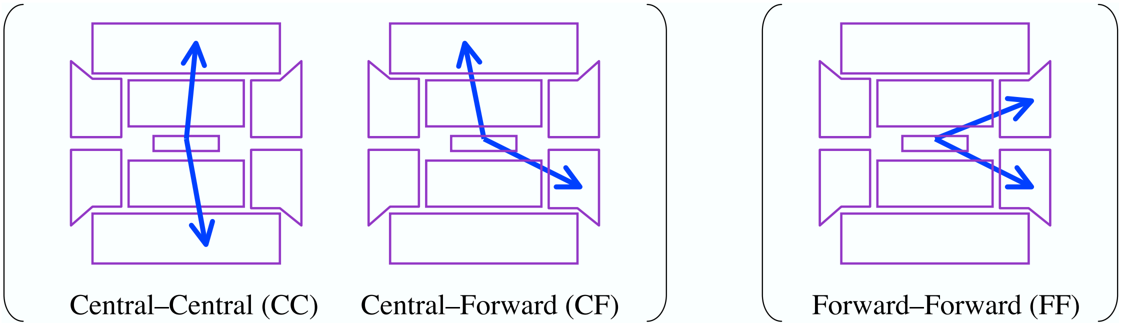

**Figure 10:** *Representation of central-central, central-forward and forward-forward events. Forward-forward events are not included in all results.*

The kinematic requirements on central electron candidates are that they have $E_T > 25\,\mathrm{GeV}$ and $p_T > 10\,\mathrm{GeV}/c$. Forward electron candidates are required to have $E_T > 20\,\mathrm{GeV}$ for central-forward events and $E_T > 30\,\mathrm{GeV}$ for forward-forward events, since the

$E_T$ spectrum is much harder for forward-forward events. An additional requirement on forward electron candidates, not strictly kinematic, is that they have the ratio of hadronic to electromagnetic energy $Had/EM < 0.125$. This requirement is part of the electron clustering for clusters having $E_{\mathrm{EM}} > 100\,\mathrm{GeV}$ and is included here for uniformity across the energy spectrum. Finally the reconstructed invariant mass of the electron pairs is required to fall in the range $66 < M_{ee}^{\mathrm{reco}} < 116\,\mathrm{GeV}/c^2$, central-central candidates are required to have opposite charge, and forward-forward candidates are required to have the two legs reconstructed on the same side of the detector to eliminate very low-rapidity forward-forward events.

The acceptance is defined in each bin of rapidity as $N_{\mathrm{reco}}/N_{\mathrm{gen}}$, where $N_{\mathrm{reco}}$ is defined by the geometric and kinematic requirements described above, and $N_{\mathrm{gen}}$ is the number of events having generator-level primary vertex falling in the region $z = \pm 60\,\mathrm{cm}$ around the interaction point, and generator-level mass $66 < M_{ee}^{\mathrm{gen}} < 116\,\mathrm{GeV}/c^2$.

Acceptance is shown in bins of generator-level rapidity of the Z in Figure 11. Uncertainties are not shown but are considered in the following sections. The fractions of events in each bin that come from different topologies are shown separately.

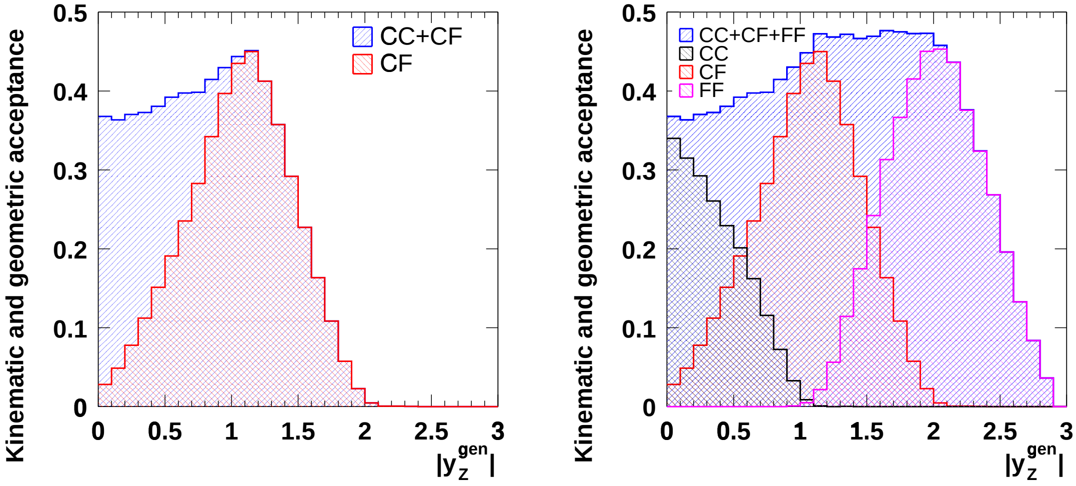

**Figure 11:** *Acceptance in bins of generator-level rapidity of the Z showing (left) central-forward and the sum of central-central and central-forward; and (right) central-central, central-forward and forward-forward, and their sum.*

Although a full NNLO calculation of $d\sigma/dy$ is used to determine the total acceptance for the inclusive cross-section measurement, systematic effects on the acceptance are evaluated using lower-order approximations from PYTHIA coupled with the CTEQ5L parton distributions.

The total cumulative effect of the acceptance cuts is shown for PYTHIA and CTEQ5L in Table 3, which also shows the large effect on statistics of including events with a forward electron: the total acceptance for central-central events is around 10% and for central-forward events around 20%.

| **Selection** | # of events | Acceptance |
|---|---|---|
| total generated $p\overline{p} \rightarrow Z \rightarrow ee$ | 507500 | |
| generated $z^{gen}_{vertex} < 60$cm | 490756 | |
| $66 < M^{gen}_{ee} < 116$ GeV/$c^2$ | 376523 | |
| **first electron** | | |
| cluster reconstructed in central detectors (CEM) | 363994 | 95.672% |
| cluster seed not in tower 9 | 350496 | 92.088% |
| cluster fiducial at CES | 299530 | 79.552% |
| $p_T > 10$GeV/$c$ | 252881 | 67.162% |
| $E_T > 25$GeV | 186318 | 49.484% |
| **second electron: central** | | |
| cluster reconstructed in central detectors (CEM) | 94418 | 25.076% |
| cluster seed not in tower 9 | 88806 | 23.586% |
| cluster fiducial at CES | 61908 | 16.442% |
| $p_T > 10$GeV/$c$ | 48410 | 12.857% |
| $E_T > 25$GeV | 43799 | 11.633% |
| $66 < M_{ee} < 116$ GeV/$c^2$ | 42123 | 11.187% |
| opposite charge | 41462 | **11.012**% † |
| **second electron: forward** | | |
| cluster reconstructed in forward detectors (PEM) | 109828 | 29.169% |
| $1.2 < \|\eta\| < 2.8$ | 94451 | 25.085 % |
| $E_T > 20$GeV | 81443 | 21.630 % |
| Had/EM < 0.125 | 81275 | 21.586 % |
| $66 < M_{ee} < 116$ GeV/$c^2$ | 78593 | **20.873**% †† |

**Table 3:** *Cumulative effect of acceptance cuts; values are total acceptances as given by* PYTHIA *and the* CTEQ5L *PDF set. At the line marked † all kinematic and geometric requirements for central-central candidate selection have been applied, and at the line marked †† all requirements for central-forward candidates have been applied. See Section 3.1 for discussion of CES fiduciality and tower 9.*

The convolution of acceptance as a function of rapidity with the NNLO calculation of

$d\sigma/dy$,

$$A = \frac{\int A(y)\frac{d\sigma}{dy}}{\int \frac{d\sigma}{dy}}, \tag{3.1.1}$$

gives a central value for the total acceptance of 31.82% when computed using the MRST 2002 NNLO PDF set.

## 3.2. Systematic Uncertainties

Uncertainties in energy scales and resolutions, in the momentum scale, in the material count in the simulation, in the modeling of the $p_T$ of the Z at generation, and in the parton distribution functions used are all taken into consideration in evaluating the systematic uncertainty on the acceptance and are described in the following sections.

### 3.2.1 Energy Scales

A change in the central and plug calorimeter scales can lead to a migration of events in and out of the $E_T$ event selection cuts and the mass window cut. To find the uncertainty on the CEM and PEM energy scales, the calorimeter scales are varied in small steps in the simulated data and the resulting Z mass peak monitored: for the CEM scale, the peak obtained from the central-central events, and for the PEM scale the central-forward events. At each scaling step a $\chi^2$ is calculated between the rescaled simulated Z mass peak and the data. The fit is made in the small mass window $86 < m_{ee} < 98\,\mathrm{GeV}/c^2$ to reduce bias from any mismodeling of the radiative tail in the simulation. The energy resolution is considered in the same way, by introducing extra smearing on top of the best-fitting value in the simulation, and calculating $\chi^2$ at each step. The mass peaks are shown in Figures 12 and 13 (with coarser binning than that used in the fit). Also shown in Figures 12 and 13 are the mass peaks found after shifting the scaling and smearing in the simulation to the extreme values found from the $\chi^2$ method. The $\chi^2$s are shown in Figure 14 and are seen to be reasonably parabolic. The method is used to fix the central values of scaling and smearing used in the simulation, such that the minima of Figure 14 are at zero. Then the scaling and smearing are applied to single electrons as

$$E_T' = E_T \cdot (1 + scale) \cdot \mathbf{G}(smear), \tag{3.2.1}$$

where $\mathbf{G}(smear)$ is a weighting generated from a Gaussian of mean $\mu = 1$ and $\sigma = smear$. The scalings and smearing applied to the simulation are given in Table 4, and the scalings applied to the data in Table 5. As part of this work, appropriate energy scalings were found for data in different run-periods and used in several CDF analyses before 'official' calibrations – as finally used in these analyses – were available.

| | scale | resolution | fit range | $\mu(m_{ee})$ / GeV/$c^2$ | $\sigma(m_{ee})$ / GeV/$c^2$ |
|---|---|---|---|---|---|
| CC | -0.2% | 0 | (86:98) | 91.11 ± 0.09 | 3.02 ± 0.09 |
| CF | E +2.5% | 2.7% | (86:98) | 91.14 ± 0.11 | 3.08 ± 0.11 |
| | W +2.5% | 2.7% | (86:98) | 91.14 ± 0.12 | 3.11 ± 0.12 |

**Table 4:** *Energy scaling applied to single electrons in simulation and resulting* $m_{ee}$ *means and widths from fitting the lineshape to a Gaussian; errors are* $\Delta\chi^2 = 1$ *errors from fitting.*

| | | scale | fit range | $\mu(m_{ee})$ / GeV/$c^2$ | $\sigma(m_{ee})$ / GeV/$c^2$ |
|---|---|---|---|---|---|
| 72 $\mathrm{pb}^{-1}$ | CC | 0 | (86:98) | 91.1 ± 0.1 | 3.0 ± 0.1 |
| 72 $\mathrm{pb}^{-1}$ | CF | E +3.6% | (86:98) | 91.1 ± 0.1 | 3.0 ± 0.1 |
| | | W +3.1% | (86:98) | 91.1 ± 0.1 | 3.1 ± 0.1 |
| 194 $\mathrm{pb}^{-1}$ | CC | 0 | (86:98) | 91.0 ± 0.1 | 2.9 ± 0.1 |
| 194 $\mathrm{pb}^{-1}$ | CF | E +3.5% | (86:98) | 91.1 ± 0.1 | 3.1 ± 0.1 |
| | | W +3.5% | (86:98) | 91.1 ± 0.1 | 3.0 ± 0.1 |
| 194 $\mathrm{pb}^{-1}$ | FF | E,W +3.5% | (86:98) | 91.1 ± 0.1 | 3.0 ± 0.1 |

**Table 5:** *Energy scaling applied to single electrons in data and resulting* $m_{ee}$ *means and widths from fitting the lineshape to a Gaussian; errors are* $\Delta\chi^2 = 1$ *errors from fitting.*

The 3-$\sigma$ or $\chi^2_{\mathrm{min}} + 9$ points are taken as conservative estimates of the energy scale uncertainty, and are found to be 0.3% for the CEM and 0.6% for the PEM. The corresponding change in acceptance is shown as a function of rapidity in Figure 15, and the change in the total acceptance $\delta(A)/A$ for CC+CF events is determined to be 0.226% for the CEM scale and 0.112% for the PEM scale. Although the uncertainty becomes large at $y \sim 2$, the acceptance is very small there and Monte Carlo statistical uncertainty also high.

The 3-$\sigma$ points for the smearing are found to be 1.5% for the CEM and 1.1% for the PEM. The corresponding change in acceptance is shown as a function of rapidity in Figure 16, and the change in the total acceptance determined to be 0.051% for the CEM resolution and 0.048% for the PEM resolution.

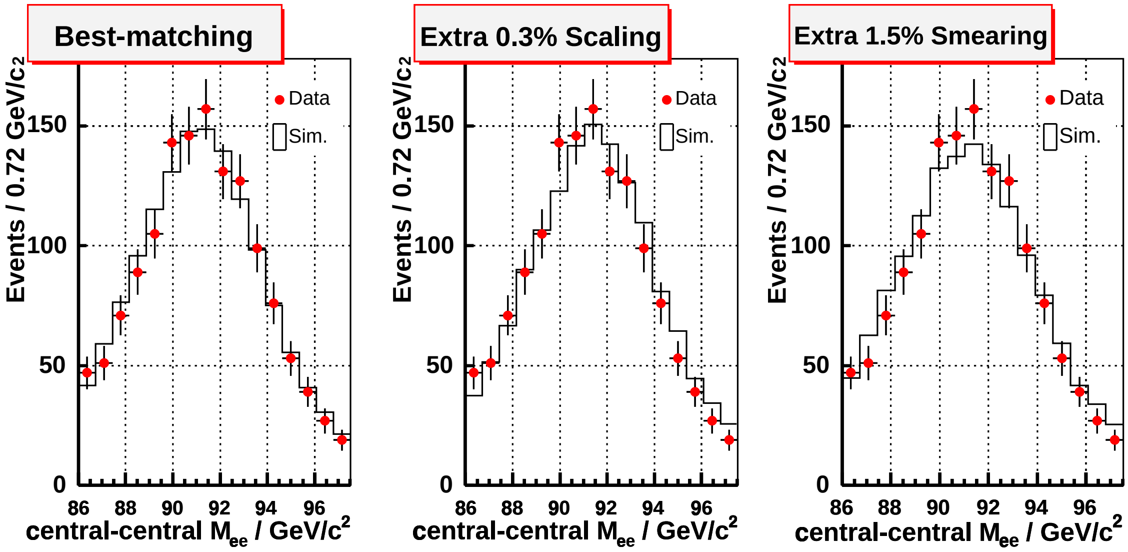

**Figure 12:** *$M_{ee}$ shown for central-central events. The left-hand plot shows the scaling and smearing (defined in Eqn 3.2.1) giving the best fit between data and simulation. In the central plot the simulation has 3-$\sigma$ extra scaling applied, and in the right-hand plot the simulation has 3-$\sigma$ extra smearing applied.*

The large change in acceptance for central-forward events that arises from a small change in the central energy scale is explained by the $E_T$ spectra for central electrons shown in Figure 17: as the central electron $E_T$ cut is at 25 GeV in a rapidly falling region of the spectrum for central-forward events, there can be considerable migration of events.

Finally, the muon group has used the same method and the reconstructed mass peak from Z $\rightarrow \mu\mu$ tracks to estimate a systematic uncertainty associated with the tracking $p_T$ scale (study by Jian Kang [25]). The 3-$\sigma$ point is found to be 0.3% and the resulting change in total acceptance $\delta(A)/A$ for CC+CF events is determined to be 0.038%.

The uncertainties from the CEM and PEM energy scales and resolutions, and from the $p_T$ scale, are all summed in quadrature. All of the systematic uncertainties on the total acceptance are summarised in Table 8.

### 3.2.2 Material

The amount of material in the detectors determines the extent of electron bremsstrahlung and thus affects the electron $p_T$ spectrum and the electromagnetic showering seen in the calorimeters. When using the simulation to determine the acceptance it is therefore nec-

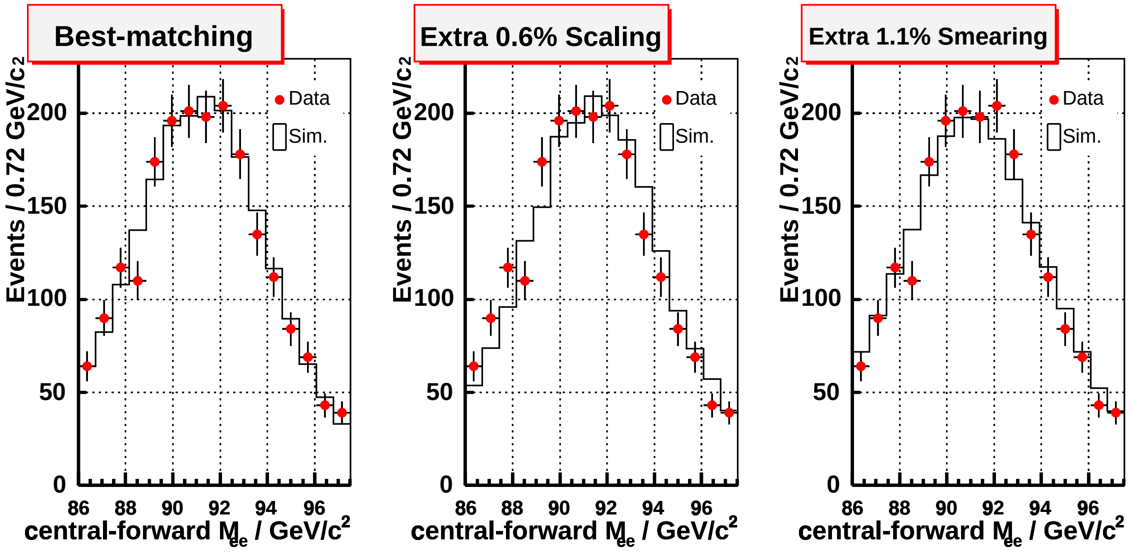

**Figure 13:** *$M_{ee}$ shown for central-forward events. The left-hand plot shows the scaling and smearing (defined in Eqn 3.2.1) giving the best fit between data and simulation. In the central plot the simulation has 3-$\sigma$ extra scaling applied, and in the right-hand plot the simulation has 3-$\sigma$ extra smearing applied.*

essary to understand the accuracy with which the detector simulation models the true amount of material in the detector. Furthermore, in the central region the electron identification variables that relate to calorimeter-track matching are particularly sensitive to the amount of material in the simulation. Although identification efficiencies are measured from the data, an important input that is taken from the simulation is the rate of same-sign Z events. These events can arise if an electron interacts to give off a hard photon that then converts and if, of the resulting tracks, it is a track of opposite sign from the original electron that is associated with the calorimeter cluster. Such electrons are referred to as 'tridents'.

Given the sensitivity of the $E/p$ distribution for electrons in the central region to the amount of bremsstrahlung, the tail of the $E/p$ distribution has been used to study the amount of material in front of the central calorimeters. Previous studies mapping $e^+e^-$ conversion pairs indicated insufficient material in the simulation and had resulted in thin copper cylinders being added to the detector description in the simulation. By varying their thickness and comparing the resulting $E/p$ distribution with data, the conclusion was made that a systematic variation of ± 1.5% $X_0$ of copper should be made on the material

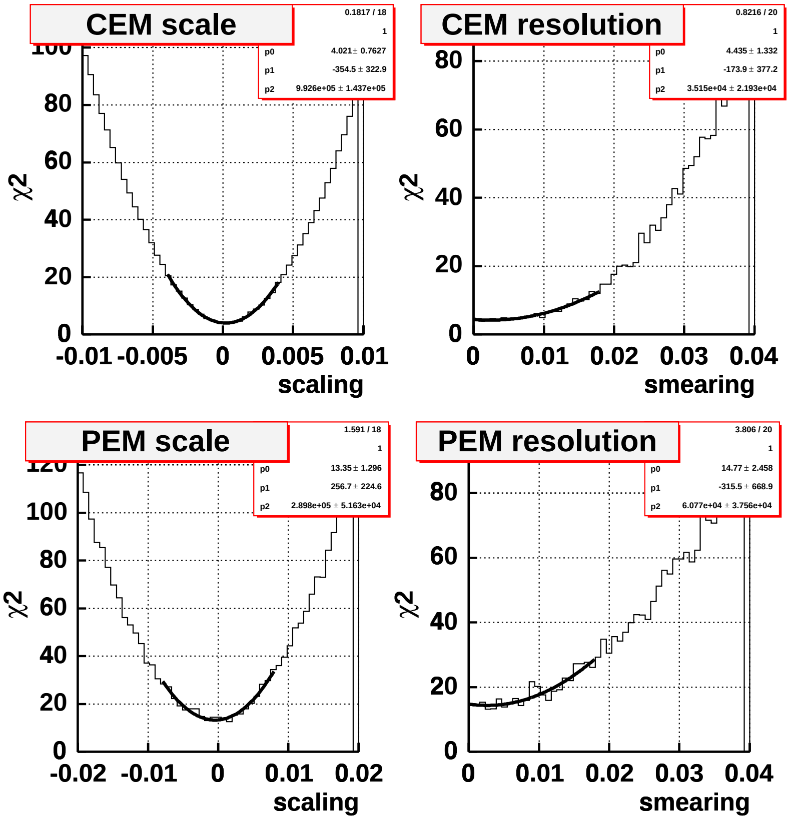

**Figure 14:** *$\chi^2$ fits for energy scaling and smearing as defined in Eqn 3.2.1, using $M_{ee}$. Fit parameters shown are for the polynomial* $p0 + p1 \cdot x + p2 \cdot x^2$.

in front of the COT (central region study by Greg Veramendi [26]). The $E/p$ distributions in the data and for the simulated data with different amounts of material are shown in Figure 18.

The energy deposited by electrons in the plug pre-radiator (PPR) is sensitive to the material in front of the forward detectors, and as part of this analysis it has been used to improve the simulation and estimate a systematic variation. Figure 19 shows the ratio of the PPR energy to the PEM energy for the forward legs of central-forward electrons, and Figure 20 shows the PPR energy. The data points are shown in red and in blue is the simulation before any tuning. It is found that to give reasonable agreement with the data, a significant amount of extra material should be added to the default simulation. The 'new default' resulting from this study is to have an extra $\frac{1}{3}X_0$ iron in front of the face of the plug, and this is shown in black in Figures 19 and 20. Varying the amount of material around this central value gave $\pm\frac{1}{6}X_0$ iron as a conservative systematic uncertainty,

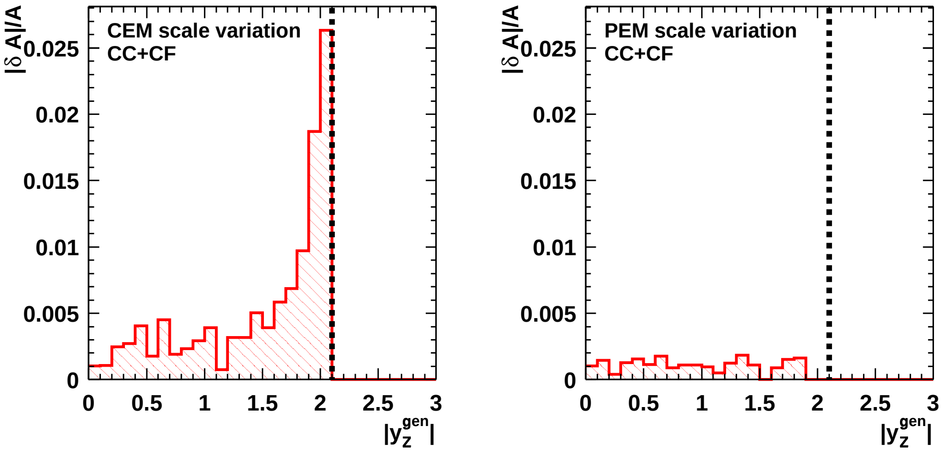

**Figure 15:** *The systematic effect on the acceptance for CC+CF events of varying the central and plug calorimeter energy scales in the simulation, shown in bins of rapidity of the Z at generator-level. The dotted line gives the upper limit on the acceptance.*

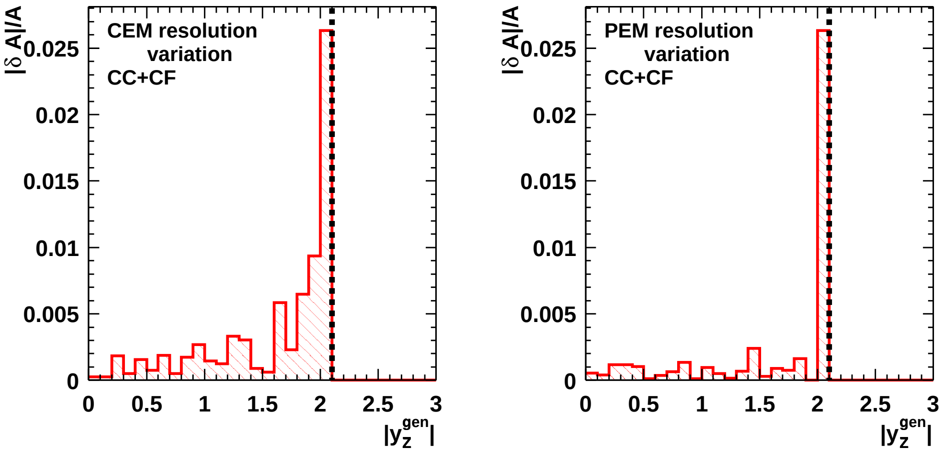

**Figure 16:** *The systematic effect on the acceptance for CC+CF events of varying the central and plug calorimeter resolutions in the simulation, shown in bins of rapidity of the Z at generator-level. The dotted line gives the upper limit on the acceptance.*

and the yellow bands show the effect of that variation on the PPR response. After the freezing of the simulation for these measurements, continuation of these studies resulted in further improvements to the simulation by identifying the ‘missing’ material with readout cables from the silicon system, and correspondingly replacing the iron with copper. A more

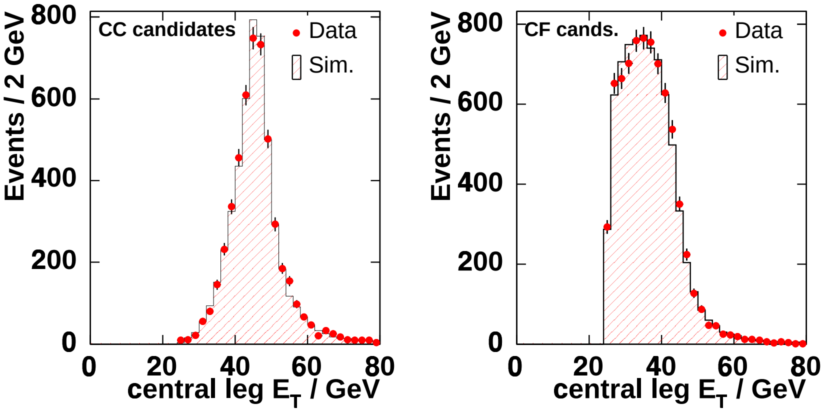

**Figure 17:** *$E_T$ spectra for central legs of selected CC and CF events; data (markers) and simulation (histogram).*

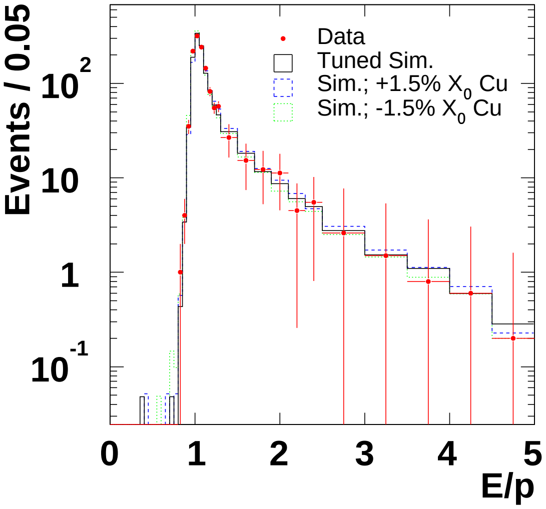

**Figure 18:** *E/p for central electrons, showing the data and simulation with different amounts of material in front of the tracker, which affects the high tail of the distribution.*

sophisticated geometry was also implemented.

The systematic effect on the acceptance is found by generating and fully simulating four datasets with material added and removed from the barrel and ends of the COT, for each sample recalculating the central value of the energy scaling and smearing, and measuring the acceptance. The changes to the total acceptance are shown in Table 8 and the rapidity dependence is shown in Figure 21. Most of the acceptance systematics discussed here are found from a reweighting of the principal simulated dataset. However since the material

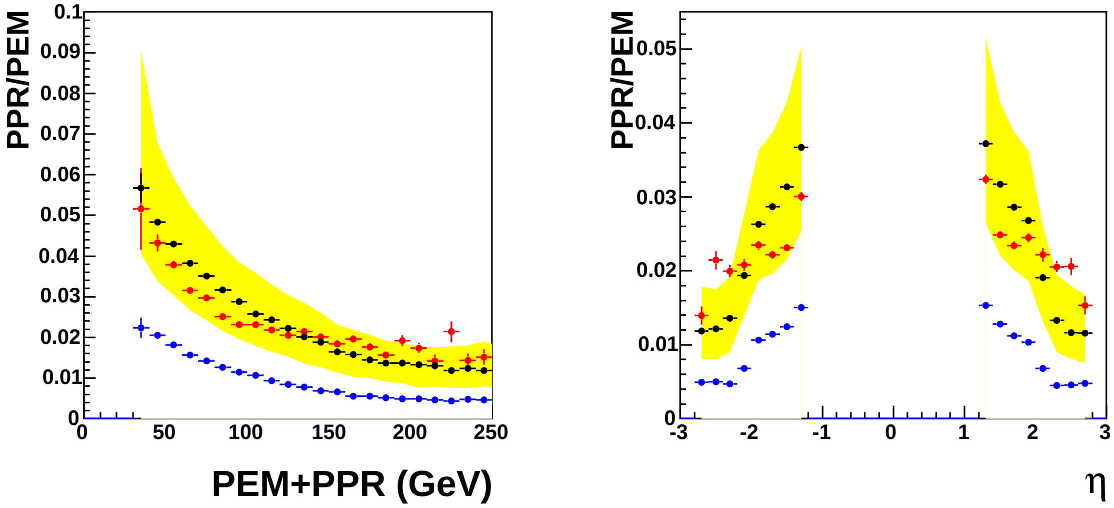

**Figure 19:** *Ratio of PPR to PEM cluster energy for forward legs of central-forward Zs, as a function of total cluster energy (left) and cluster $\eta$ (right). Data (red), tuned simulation* `zewk1e` *with $\frac{1}{3}X_0$ (Fe) (black) and yellow bands showing the spread of* `zewk7e` *and* `zewk8e` *($(\frac{1}{3} \pm \frac{1}{6})X_0$ (Fe) respectively); and untuned simulation* `ztop0e` *(blue).*

systematic uncertainty involves simulating new datasets and there is a resulting Monte Carlo statistical uncertainty, the distribution shown in Figure 21 is smoothed, and the smoothed values used rather than the bin contents. The smoothed distribution consists of two straight line fits to the regions $0 < |y_{\mathrm{Z}}^{\mathrm{gen}}| < 1$ and $1 < |y_{\mathrm{Z}}^{\mathrm{gen}}| < 2$. A straight line fit models the distribution reasonably for $|y_{\mathrm{Z}}^{\mathrm{gen}}| \lesssim 1.7$, and the fluctuations at higher values of $|y_{\mathrm{Z}}|$ are associated with the Monte Carlo statistical uncertainty, shown later in Figure 25.

### 3.2.3 Boson $p_T$

Initial state soft gluon radiation and intrinsic $p_T$ of partons in the proton are not very well known, so there is some uncertainty associated with the transverse momentum of the Z, $p_T^{\mathrm{Z}}$, which affects the angular distributions and energies of the decay electrons and hence the acceptance. The uncertainty is estimated by retuning Pythia [24] parameters PARP(62) and PARP(64) (parton shower evolution $Q^2$ parameters), and PARP(91) and PARP(93) (the '$k_{\mathrm{T}}$ smearing' parameters), forming $\chi^2$ between the resulting $p_T^Z$ distributions in simulation and data, and finding new best-fit values and 3-$\sigma$ points (study by Eva Halkiadakis [34]).

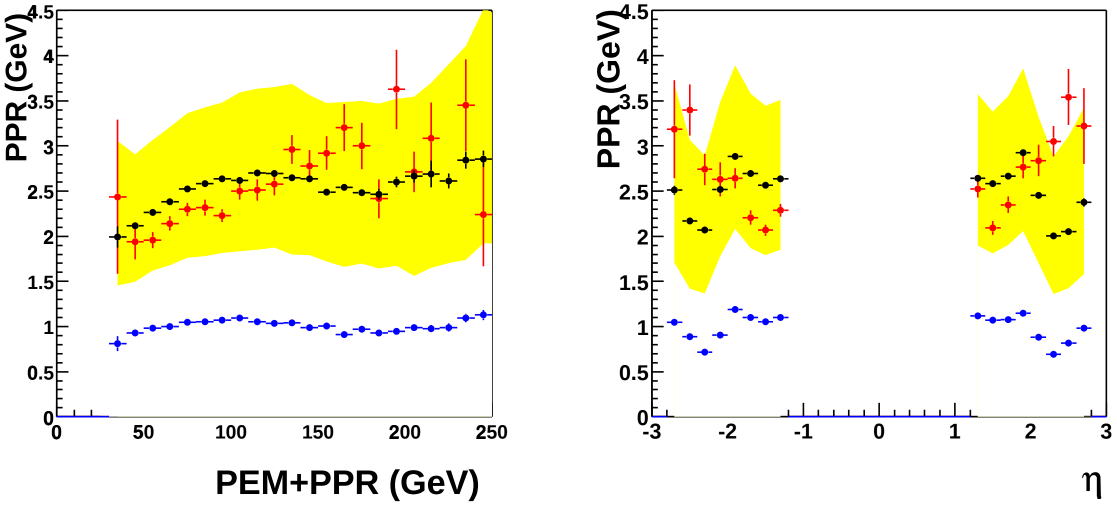

**Figure 20:** *Energy deposited in the PPR by forward legs of central-forward Zs, as a function of total cluster energy (left) and cluster $\eta$ (right). Data (red), tuned simulation* `zewk1e` *with* $\frac{1}{3}X_0$ *(Fe) (black) and yellow bands showing the spread of* `zewk7e` *and* `zewk8e` *(*$(\frac{1}{3} \pm \frac{1}{6})X_0$ *(Fe) respectively); and untuned simulation* `ztop0e` *(blue).*

The values of the parameters and their variations are shown in Table 6. The default $p_T^Z$ distribution is reweighted to the 3-$\sigma$ points as shown in Figure 22 and the resulting changes in acceptance reported in Table 7. PARP(93) is found to have a negligible effect and is discounted.

The total uncertainty from $p_T^Z$ modeling is taken to be the quadrature sum of the contributions from the different parameters and is included in the summary table, Table 8.

| Parameter | Description | Previous default | New default | $3\sigma$ |
|---|---|---|---|---|
| PARP(62) | $Q^2_{\mathrm{min}}$ for parton showers | 1.25 | 1.26 | 0.30 |
| PARP(64) | $K_T$ evolution scale factor | 0.2 | 0.02 | 0.03 |
| PARP(91) | $K_T$ $\sigma$ | 2.0 | 0.17 | 0.3 |
| PARP(93) | $K_T$ cutoff | 15 | 2 | 3 |

**Table 6:** Pythia *parameters used in boson* $p_T$ *tuning.*

### 3.2.4 NNLO Calculation

The total acceptance is found by the convolution given in Eqn. 3.1.1. The cross-section

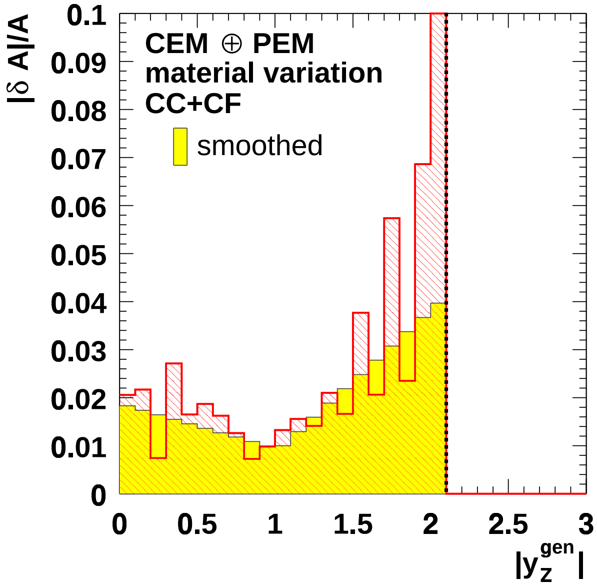

**Figure 21:** *The systematic effect on the acceptance for CC+CF events of varying separately the amount of material in front of the central and plug calorimeters, shown in bins of rapidity of the Z at generator-level. The vertical dotted line gives the upper limit on the acceptance.*

| CC+CF | $A_Z$ | $\Delta A_Z/A_Z$ |
|---|---|---|
| Default | 31.8860% | |
| PARP(62) + | 31.8864% | +0.001% |
| PARP(62) – | 31.8880% | +0.006% |
| PARP(64) + | 31.9010% | +0.047% |
| PARP(64) – | 31.8676% | –0.058% |
| PARP(91) + | 31.8811% | –0.015% |
| PARP(91) – | 31.8919% | +0.019% |

**Table 7:** *The change in acceptances from variations of* PYTHIA *parameters that tune $p_T^Z$. For each parameter the larger variation is taken and summed in quadrature.*

measurement used for the central value is at NNLO [27]. Uncertainties associated with the calculation include the electroweak parameters that go into it, and the renormalisation scale used. The calculation is repeated using a renormalisation scale of $M_Z/2$ and $2M_Z$ as well as the default $M_Z$, but the resulting uncertainty on $A$ is negligible (study by Willis Sakumoto, [29]).

The program is also used to compute the cross-section at NLO, and the result is

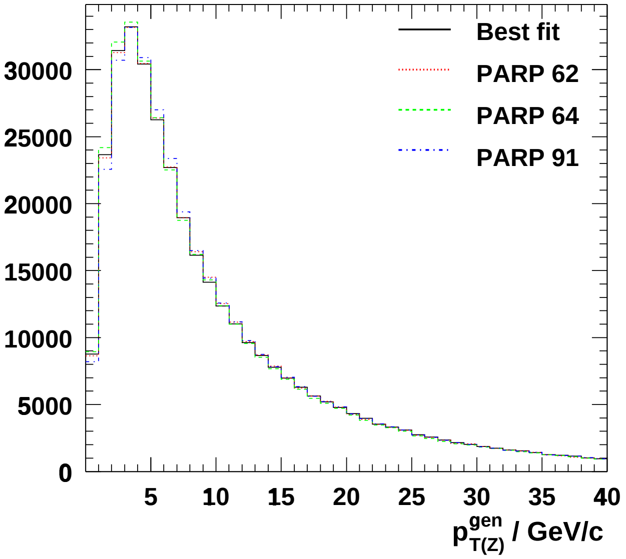

**Figure 22:** *Generator-level $p_T$ of the Z with the central values of the parameter tuning (black) and the 3-$\sigma$ values for* PARP62*,* PARP64 *and* PARP91*.*

compared to an alternative NLO calculation [28] (study by Willis Sakumoto, [29]). As the two NLO calculations are found to be in excellent agreement, no uncertainty is assigned to the calculation. However an uncertainty of the difference between NLO and NNLO, namely 0.06%, is assigned to cover any higher-order effects above NNLO.

### 3.2.5 PDFs

The central value for the total acceptance is found using a cross-section calculated at NNLO and as the only generally-used NNLO PDF set is that of MRST, that is the set used for the central value.

However PDF sets are constructed from fits to large numbers of sets of experimental data, which have associated uncertainties. Much of the data comes from the HERA experiments. There, effects such as the energy scales of the detectors, the relative positions of detectors, and the background estimates can move events between bins of proton momentum fraction $x$ and momentum transfer $Q^2$, changing the shapes of experimental distributions. Effects are correlated in a complicated way between bins and between experiments. Further results come from fixed target experiments and from the Tevatron, and these uncertainties must be taken into account in the fitting.

The CTEQ [11] and MRST [12] groups have attempted to propagate the errors on the experimental data into their NLO PDF sets by constructing sets of eigenvectors representing orthogonal combinations of different sources of uncertainty. The CTEQ collaboration constructs 20 eigenvectors, and the MRST collaboration 15 eigenvectors. From each eigenvector are generated two PDF sets, corresponding to variations in each direction along the eigenvector that lead to $\Delta\chi^2 = 100$ (CTEQ) or $\Delta\chi^2 = 50$ (MRST) with respect to the central or 'best-fit' PDF set parametrization.

Computing $d\sigma/dy$ at NLO using these 'error' PDF sets and adding the resulting changes in acceptance for each set in quadrature is advised by the CTEQ and MRST collaborations to be a theoretically sound prescription for estimating the fractional PDF uncertainty on the total acceptance.

The fractional changes in the cross-sections are shown as a function of boson rapidity in Figure 23, where the pairs in the plots correspond to the $\pm 3\sigma$ values of a particular CTEQ eigenvector. Figure 24 shows these fractional changes convolved with the Z boson acceptance.

For each eigenvector it is seen whether each of the two corresponding PDF sets is an 'up' set, leading to an increase in acceptance; or a 'down' set, leading to a decrease in acceptance. In many cases the two PDF sets for a single eigenvector are reflections of each other about $\delta A = 0$ (such as sets 1 and 2 shown in Figure 24). However in some cases the change in acceptance has the same sign for both PDF sets of an eigenvector pair.

For this reason an asymmetric uncertainty is constructed by summing in quadrature the 'up' changes in acceptance separately from the 'down' changes in acceptance; and in the same-sign cases the mean quadrature sum $\sqrt{\frac{1}{2}(\Delta A_i^{2\,(+3\sigma)} + \Delta A_i^{2\,(-3\sigma)})}$ is accumulated.

The MRST uncertainty is found to be encompassed by the CTEQ uncertainty so the latter is taken; it is $^{+0.69}_{-0.84}\%$.

Owing to the way in which the eigenvectors are constructed it is difficult to interpret the physical source of the uncertainty coming from a particular eigenvector. It is known that CTEQ eigenvector 15 represents the uncertainty on the gluon distribution; but its contribution to the acceptance uncertainty is small for this analysis.

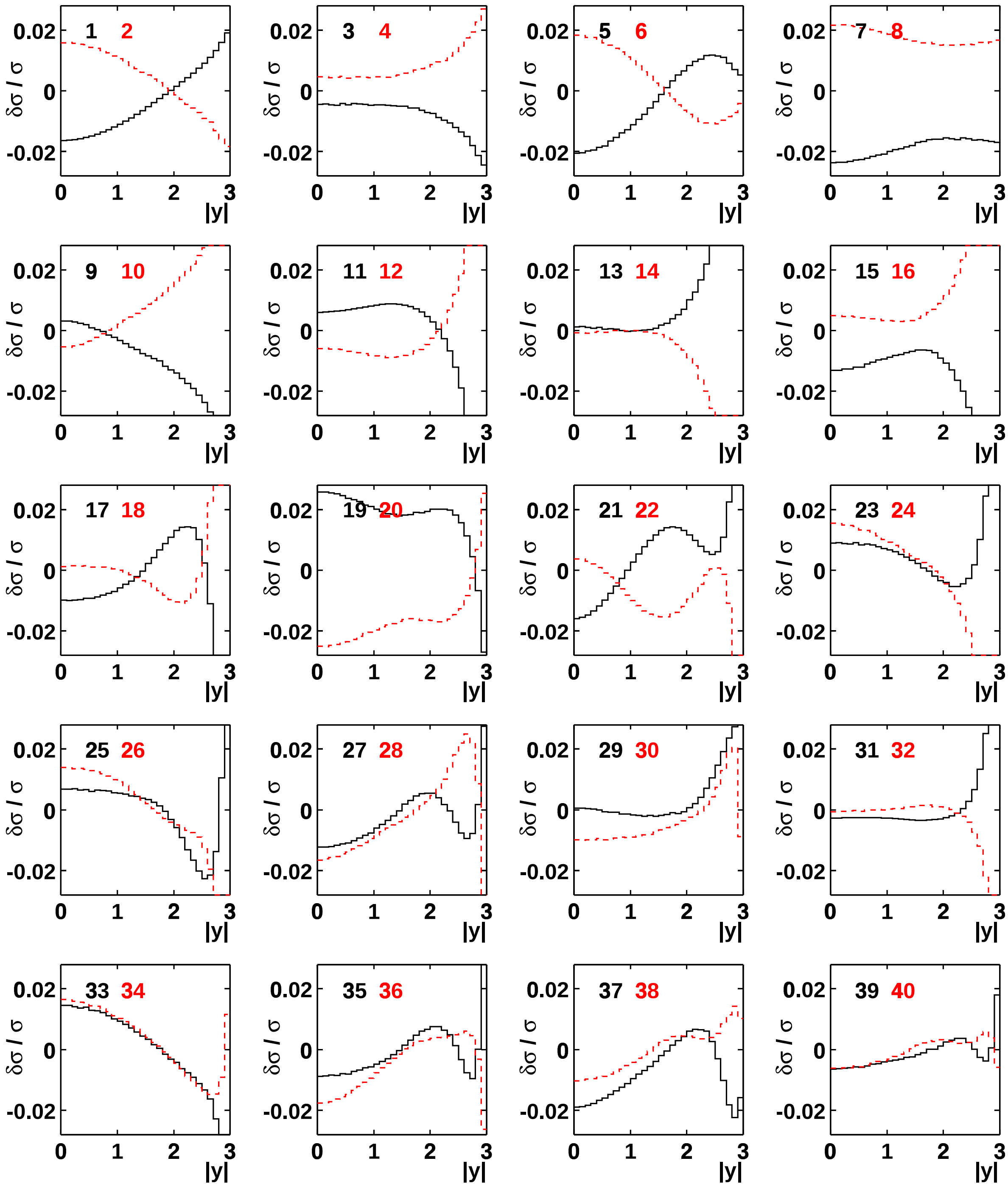

**Figure 23:** *Fractional uncertainty* $\frac{(\sigma_i - \sigma_0)}{\sigma_0}$ *from* CTEQ *error PDF sets. The pairs of lines in each sub-plot correspond to* $\pm 3\sigma$ *for each of 20 eigenvectors.*

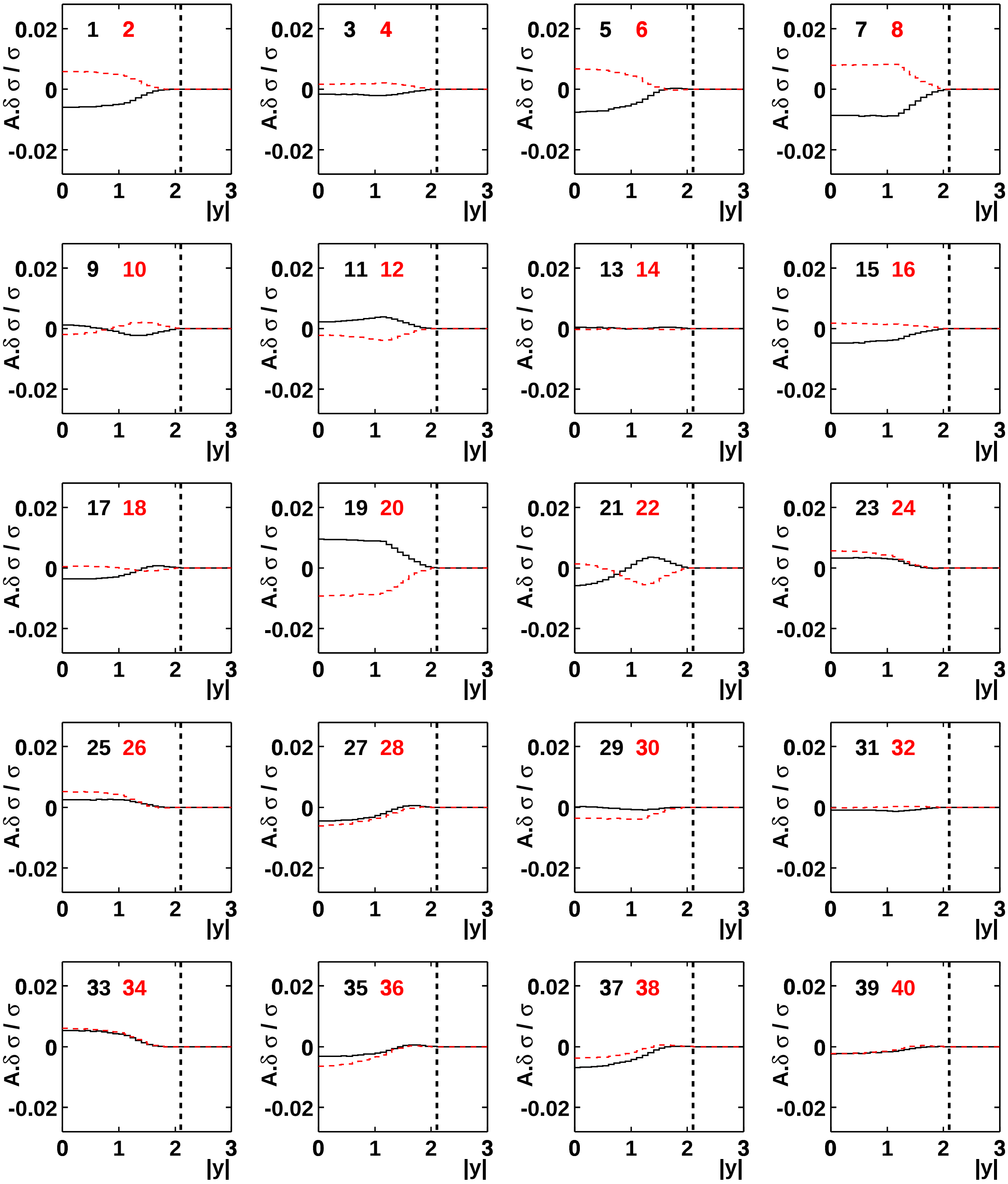

**Figure 24:** *Fractional uncertainty* $\frac{A\cdot(\sigma_i-\sigma_0)}{\sigma_0}$ *from* CTEQ *error PDF sets. The pairs of lines in each sub-plot correspond to* $\pm3\sigma$ *for each of 20 eigenvectors. The vertical dashed line indicates the upper limit of the acceptance.*

### 3.2.6 Summary of Systematic Uncertainties on the Acceptance

The systematic uncertainties on the total acceptance are summarised in Table 8, and on the acceptance as a function of rapidity in Figure 25, which also shows the acceptance uncertainty coming from Monte Carlo statistics. The sum of the systematic and MC statistical uncertainties is show in Figure 26, and the resulting value of the total acceptance is $0.3182 \pm 0.0041$.

It can be seen that the principal contributions to the acceptance systematic uncertainies are the PDFs and the knowledge of the central material, but that both effects are smaller using combined CC+CF data than they are using CC events alone. The effect of the CF events can be understood on the material systematic since no opposite-sign requirement is made on CF events, which are therefore insensitive to the 'tridents' described in Section 3.2.2. The PDF uncertainty manifests itself in a change in the calculated $d\sigma/dy$ used to determine the acceptance. By including CF events $d\sigma/dy$ is probed to higher values of $y$, and to some extent PDF differences are 'integrated out'.

| source | variation | $\Delta A_Z^{CC}/A_Z^{CC}$ | $\Delta A_Z^{CF}/A_Z^{CF}$ | $\Delta A_Z^{CC+CF}/A_Z^{CC+CF}$ |
|---|---|---|---|---|
| Monte Carlo statistics | | 0.463% | 0.317% | 0.238% |
| Central $E_T^e$ scale | 3-$\sigma$ variation | 0.073% | 0.320% | 0.226% |
| Plug $E_T^e$ scale | 3-$\sigma$ variation | negl. | 0.171% | 0.112% |
| Central $E_T^e$ res | 3-$\sigma$ extra smearing | 0.045% | 0.054% | 0.051% |
| Plug $E_T^e$ res | 3-$\sigma$ extra smearing | negl. | 0.073% | 0.048% |
| $p_T^e$ scale | 3-$\sigma$ variation | 0.048% | 0.034% | 0.038% |
| $p_T^Z$ model | PYTHIA retuning | 0.056% | 0.085% | 0.061% |
| Central material | extra material samples | 1.327% | 0.730% | 0.936% |
| Plug material | extra material samples | negl. | 0.323% | 0.211% |
| PDFs | CTEQ error PDFs | $^{+1.60\%}_{-2.03\%}$ | $^{+0.43\%}_{-0.58\%}$ | $^{+0.66\%}_{-0.76\%}$ |
| NNLO calculation | NNLO-NLO difference | | | 0.06% |
| Total | | $^{+2.133\%}_{-2.472\%}$ | $^{+1.035\%}_{-1.105\%}$ | $^{+1.219\%}_{-1.276\%}$ |

**Table 8:** *Acceptance Systematics*

**Forward-Forward Acceptance** The same procedures are used to determine the acceptance systematics for forward-forward events. The energy scale and resolution systematics

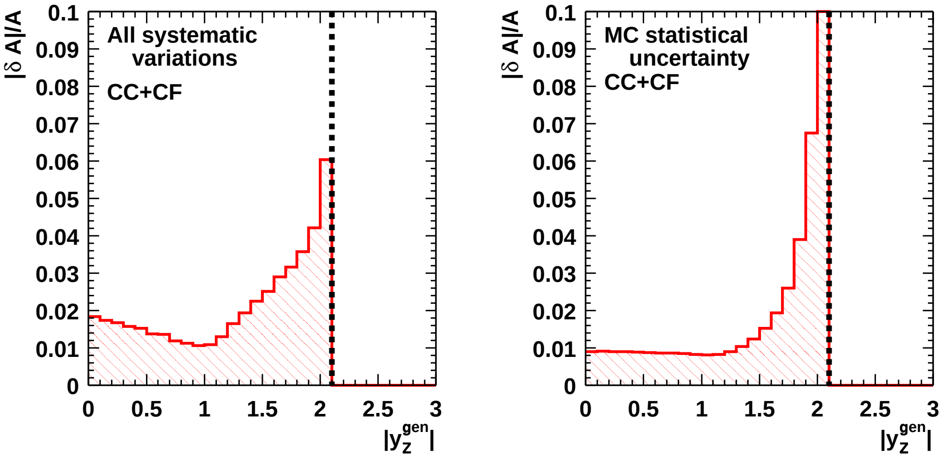

**Figure 25:** *Systematic effects on CC+CF acceptance. [left] All systematic effects on the acceptance (energy scale and resolution, material) summed in quadrature. [right] Acceptance uncertainty from MC statistics. The vertical dotted line gives the upper limit on the acceptance.*

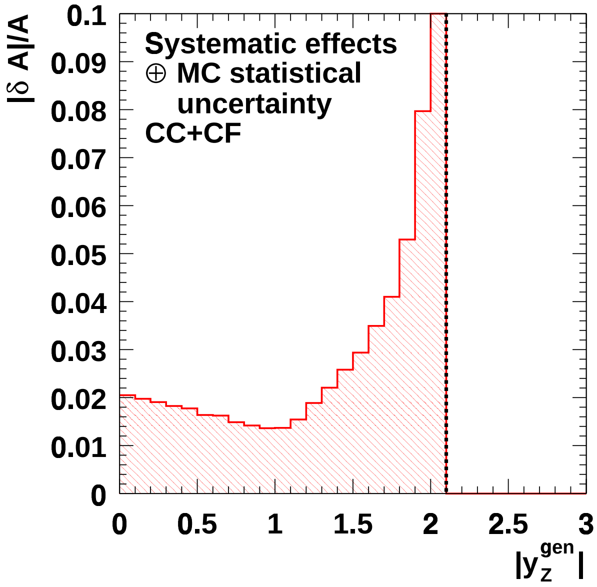

**Figure 26:** *Total systematic plus MC statistical uncertainty on CC+CF acceptance. The vertical dotted line gives the upper limit on the acceptance.*

are very small for the combined CC+CF+FF sample, and the dominant effects are the material and Monte Carlo statistical uncertainty. The combined systematic and MC statistical uncertainties are shown as a function of boson rapidity in Figures 27 and 28. As will be discussed later, one of the selection criteria for forward-forward events is that one leg have an associated silicon track. The efficiency of this requirement is measured in Section 4.5.2.1, but the result is anticipated in Figures 27 and 28 by the dash-dotted line indicating the highest values of rapidity that can be reconstructed, given this requirement.

The silicon tracking efficiency that is measured is in effect a convolution of silicon detector acceptance and track-finding efficiency, but since the coverage of the silicon system is complicated and not very well-modeled in the simulation, a single acceptance ⊗ efficiency is measured from the data to take account of both effects.

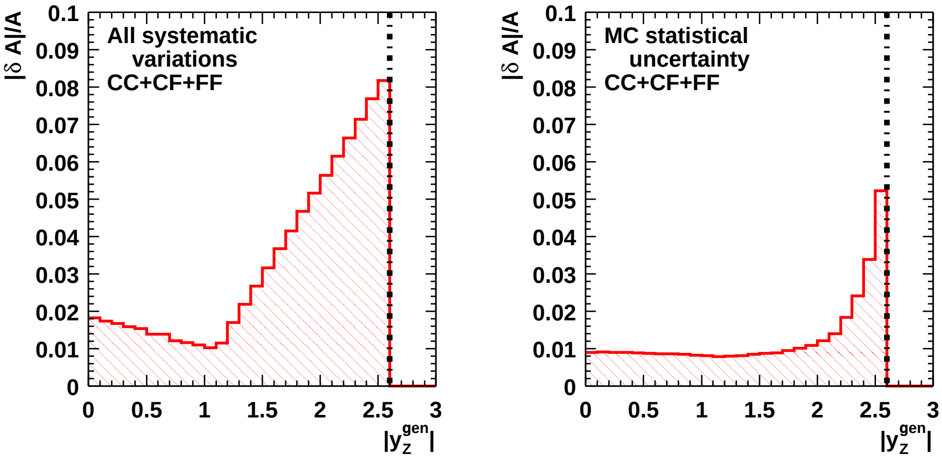

**Figure 27:** *Systematic effects on CC+CF+FF acceptance. [left] All systematic effects on the acceptance (energy scale and resolution, material) summed in quadrature. [right] Acceptance uncertainty from MC statistics. The vertical dash-dotted line gives the upper limit on the acceptance, determined by the silicon tracking.*

## 3.3. $z$ Vertex

One further quantity related to the acceptance concerns the fraction of the luminous region sampled by the $|z_{vertex}| < 60\,\text{cm}$ cut, which appears in the expression for the cross-section as $\epsilon_{zvertex}$. The $z$ vertex distribution of minimum-bias events is measured and fitted to the form of the p$\overline{\text{p}}$ luminosity function,

$$\frac{d\mathcal{L}}{dz} = N_0 \frac{\exp\left(-z^2/2\sigma_z^2\right)}{1+\left(\frac{z-z_{\text{min}}}{\beta^*}\right)^2} \tag{3.3.1}$$

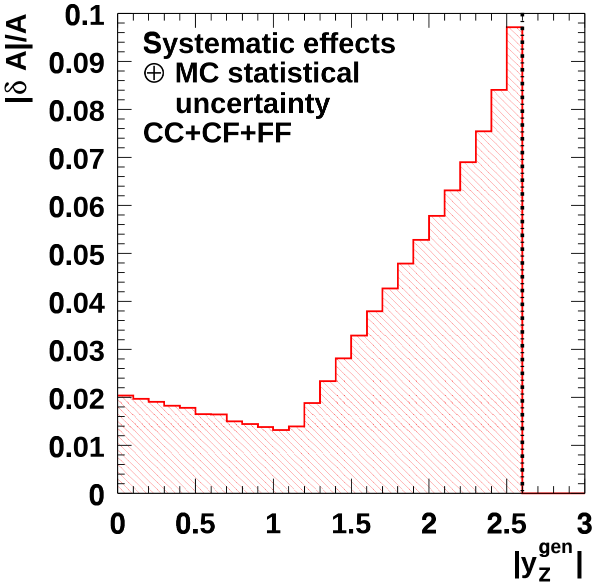

**Figure 28:** *Total systematic plus MC statistical uncertainty on CC+CF+FF acceptance.The dash-dotted line gives the upper limit on the acceptance, determined by the silicon tracking.*

where $\beta^*$ and $\sigma_z$ are beam parameters, $z_{\text{min}}$ is the average value of the $z$ vertex distribution, and $N_0$ normalises the distribution (study by Willis Sakumoto, [35]).

The resulting fraction of the luminosity sampled in $|z_{vertex}| < 60\,\text{cm}$ is measured for the run periods corresponding to the two datasets used and is found to be:

$$\epsilon_{zvertex} = 0.950 \pm 0.001\,(\text{stat}) \pm 0.004\,(\text{sys}) \quad (72\text{pb}^{-1})$$

$$\epsilon_{zvertex} = 0.948 \pm 0.001\,(\text{stat}) \pm 0.003\,(\text{sys}) \quad (194\text{pb}^{-1}).$$

## 3.4. Acceptance and Systematic Uncertainties for $\text{W} \to \text{e}\nu$

This section summarises the acceptance and systematic uncertainties obtained by Eva Halkiadakis [34] for her measurement of $\sigma(\text{p}\overline{\text{p}} \to \text{W}) \cdot Br(\text{W} \to \text{e}\nu)$, which will be used in the determination of the systematic uncertainty on the ratio of acceptances for W and Z events needed for the calculation of the ratio of cross-sections.

In the same way as for the Z cross-section measurement, the acceptance for W bosons is found as a function of boson rapidity and convolved with a NNLO calculation of $d\sigma/dy$ to obtain the total acceptance.

W bosons are selected by finding one electron candidate in the central region, with exactly the same geometric and kinematic requirements as made for the Z boson selection and described in Section 3.1. In addition a requirement is made that there is large missing transverse energy $\not\!\!E_{\mathrm{T}} > 25\,\mathrm{GeV}$. The colliding partons have $p_T \sim 0$ so $\not\!\!E_{\mathrm{T}}$ is identified with the $p_T$ of the neutrino, which escapes the detector without interacting.

The W → e$\nu$ acceptance is shown with that for Z → ee in Figure 29. As the central electron selection is the same as for Z boson events and the neutrino in W boson events can 'go anywhere', the W → e$\nu$ acceptance extends to a similar maximum value of boson rapidity as the CC+CF Z → ee acceptance.

The central value for the W boson acceptance, convolving $A(y)$ with a NNLO calculation, is found to be 23.97%.

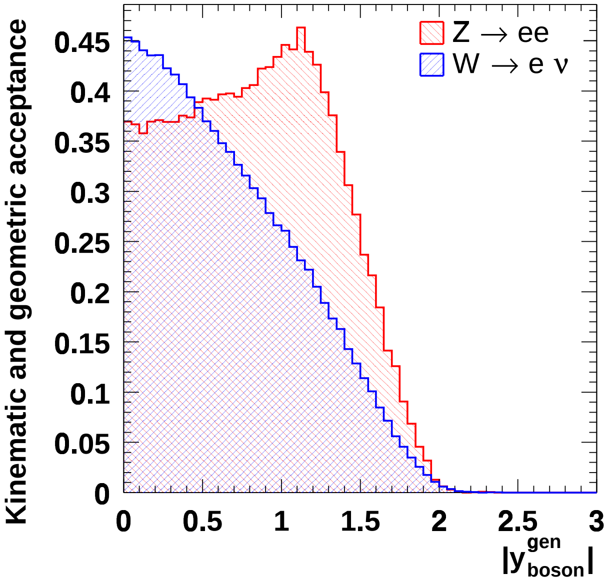

**Figure 29:** *W → e$\nu$ acceptance in bins of rapidity, shown for comparison with the CC+CF Z → ee acceptance.*

The systematic effects on the acceptance considered for Z boson events of energy scale, material count, boson $p_T$ modeling and PDF uncertainty are also obtained for W boson events and are summarised in Table 9.

For W events there is also an uncertainty from the $\not\!\!E_{\mathrm{T}}$ requirement that comes from the modeling of the boson recoil energy and hadronic showering, and also from multiple interaction and accelerator backgrounds that are not well-modeled in the simulation.

The transverse recoil energy $U$ is defined as the total energy in the calorimeter, except for the energy associated with the high-$p_t$ lepton. The modeling of the recoil energy is tuned in the simulation in a similar way to the lepton energy scale as described in Section 3.2.1. The recoil energy is separated into components parallel and perpendicular to the high-$p_T$ electron transverse direction, as shown in Figure 30, because effects such as the model for the W boson recoil and the electron energy deposition are expected to depend on the electron direction. As with the lepton energy scale uncertainty, the recoil energy is scaled and smeared to find the best fit and 3-$\sigma$ systematic points, and the acceptance is measured at the extreme values.

These extra effects for W bosons are also included in Table 9.

It can be seen that uncertainties such as the energy scale are similar for the W boson acceptance and Z boson acceptance. However the PDF uncertainty is larger for the W acceptance – more like that for central-central Z events – which is explained by the different shapes of the W and Z acceptance as a function of boson rapidity. The material count has a smaller effect on the W boson acceptance than on the Z boson acceptance, as in the W analysis there is only a single leg, and no concern over the measured charge of the electron as there is for central-central Z events. Clearly the W acceptance is only negligibly affected (through the recoil energy measurement) by uncertainties in the energy scale and resolution and the material count in the forward plug detectors, as the W analysis accepts only central electrons. Finally the difference between the uncertainties between NNLO and NLO $d\sigma/dy$ calculations is also an effect of the different coverage of the two analyses.

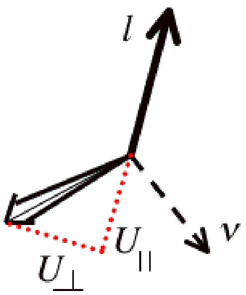

**Figure 30:** *Recoil energy in W events*

| source | variation | $\Delta A_W/A_W$ |
|---|---|---|
| Monte Carlo statistics | | 0.13% |
| Central $E_T^e$ scale | 3-$\sigma$ variation | 0.34% |
| Plug $E_T^e$ scale | 3-$\sigma$ variation | negl. |
| Central $E_T^e$ res | 3-$\sigma$ extra smearing | 0.03% |
| Plug $E_T^e$ res | 3-$\sigma$ extra smearing | negl. |
| $p_T^e$ scale | 3-$\sigma$ variation | 0.03% |
| $p_T^Z$ model | PYTHIA retuning | 0.04% |
| Central material | extra material samples | 0.73% |
| Plug material | extra material samples | negl. |
| PDFs | CTEQ error PDFs | $^{+1.16\%}_{-1.50\%}$ |
| NNLO $d\sigma/dy$ calculation | NNLO-NLO difference | 0.29% |
| Recoil energy model | 3-$\sigma$ variation | 0.25% |
| Total | | $^{+1.46\%}_{-1.75\%}$ |

**Table 9:** *W Acceptance Systematics*

## 3.5. Ratio of W and Z Acceptances

The W and Z cross-section measurements are designed to be as similar as possible in order that systematic effects cancel in their ratio. Owing to the correlations in systematic effects between W and Z boson acceptances, the uncertainty on the ratio of acceptances cannot be found by combining the uncertainties on the individual acceptances. Instead the ratio of acceptances is taken at each systematic point and the difference between that and the central value of the acceptance ratio gives the systematic. As an example, the central value of the Z boson acceptance from PYTHIA is 0.318860, the W boson acceptance is 0.242042 and hence their ratio is 1.31738. With 3-$\sigma$ extra energy smearing in the central region the Z acceptance is 0.318698, the W acceptance is 0.241974 and their ratio is 1.31711. The fractional effect on the Z acceptance of the energy resolution is therefore 0.05%, on the W acceptance 0.03%, and on the ratio of acceptances $\frac{1.31711-1.31738}{1.31738} = 0.03\%$.

The acceptance systematics on the ratio are summarised in Table 10 and for comparison the uncertainties on the W and Z boson acceptances are repeated there. It can be seen that owing to correlations between the W and Z boson acceptance systematics, the uncertainty on the ratio tends to be smaller than on the individual values.

| source | variation | $\Delta A_W/A_W$ | $\Delta A_Z/A_Z$ | $\Delta(A_Z/A_W)/(A_Z/A_W)$ |
|---|---|---|---|---|
| Monte Carlo statistics | | 0.13% | 0.24% | 0.28% |
| Central $E_T^e$ scale | 3-$\sigma$ variation | 0.34% | 0.23% | 0.16% |
| Plug $E_T^e$ scale | 3-$\sigma$ variation | negl. | 0.11% | 0.11% |
| Central $E_T^e$ res | 3-$\sigma$ extra smearing | 0.03% | 0.05% | 0.02% |
| Plug $E_T^e$ res | 3-$\sigma$ extra smearing | negl. | 0.05% | 0.05% |
| $p_T^e$ scale | 3-$\sigma$ variation | 0.03% | 0.04% | 0.02% |
| $p_T^Z$ model | PYTHIA retuning | 0.04% | 0.06% | 0.03% |
| Central material | extra material samples | 0.73% | 0.94% | 0.20% |
| Plug material | extra material samples | negl. | 0.21% | 0.21% |
| PDFs | CTEQ error PDFs | $^{+1.16\%}_{-1.50\%}$ | $^{+0.66\%}_{-0.76\%}$ | $^{+0.74\%}_{-0.56\%}$ |
| NNLO $d\sigma/dy$ calculation | NNLO-NLO difference | 0.29% | 0.06% | 0.20% |
| Recoil energy model | 3-$\sigma$ variation | 0.25% | negl. | 0.25% |
| Total | | $^{+1.46\%}_{-1.75\%}$ | $^{+1.219\%}_{-1.276\%}$ | $^{+0.95\%}_{-0.83\%}$ |

**Table 10:** *Systematics on the ratio of W and Z boson acceptances; for comparison the systematics on the individual W and Z boson acceptances are repeated here.*

# Chapter 4

# Efficiencies and Backgrounds

After having made geometric and kinematic cuts as described in the previous chapter, a further selection is made using electron identification variables in order to reduce the backgrounds. In this chapter the measurement of the efficiencies of these selection cuts, and of the remaining background fraction, is described.

## 4.1. Central Electron Selection

The central electron selection variables fall into two categories: variables measuring the shower shape, and variables measuring how well the calorimeter cluster matches its associated track.

The electron clustering is described in Section 2.2.3.1. The calorimetric selection variables are the following:

***Had/EM:*** the ratio of the cluster energy in the hadronic compartment of the calorimeter to the cluster energy in the electromagnetic compartment. Electrons deposit most of their energy in the electromagnetic calorimeter so this ratio is expected to be low for electrons compared to jets. To reduce the dependence of the cut efficiency on energy the cut value slides with energy as follows: Had/EM $< 0.055 + 0.00045 \times E_{\text{EM}}$, where the factor 0.00045 was measured in testbeam and $E_{\text{EM}}$ is measured in GeV. The energies used to compute $Had/EM$ are those obtained during the making of the clusters: further corrections such as face corrections (as described in Section 2.2.3.1) are not applied.

***Isolation:*** a measure of how much activity there is in the calorimeter around the electron candidate. $E_T^{0.4}$ is the transverse component of the sum of energies in towers that are centred within a cone of radius $\Delta R = 0.4$ about the cluster centroid. Then the isolation variable used is:

$$\frac{E_T^{0.4} - E_T^{\text{cluster}}}{E_T^{\text{cluster}}} < 0.1 \quad .$$

***$L_{shr}$:*** a comparison between the lateral profile of the calorimeter cluster and that expected from testbeam. The energies in towers adjacent to the cluster seed tower are summed in the following way:

$$L_{shr} = 0.14 \sum_{\text{adjacent towers } i} \frac{E_i - E_i^{\text{expected}}}{\sqrt{(0.14\sqrt{E_i})^2 + (\Delta E_i^{\text{expected}})^2}} \quad , \tag{4.1.1}$$

where $E_i^{\text{expected}}$ is parametrised from the testbeam data and $\Delta E_i^{\text{expected}}$ is its error, and $0.14\sqrt{E_i}$ is the uncertainty on the energy measurement [36]. A cut value of $L_{shr} < 0.2$ is used for the analysis selection.

***$\chi^2_{\text{strip}}$:*** a comparison between the shape of the pulse in the CES $r - z$ view and that expected from testbeam. A fit is made between the energies in the 11 strips of a CES cluster, taking account of the total energy of the cluster, and the $\chi^2$ of the fit is used as an identification variable, $\chi^2_{\text{strip}} < 10$.

The tracking selection variables are the following:

***Track Quality Cuts:*** the requirement that each track has at least 7 hits in each of 3 axial and 3 stereo super-layers of the COT. This ensures that the track is well-reconstructed.

***$E/p$:*** a comparison between the calorimeter cluster energy and the track momentum as a way of ensuring that a correct association has been made between cluster and track. However electrons radiate as they pass through the detector and although, for energetic electrons, bremsstrahlung photons tend to be measured in the same calorimeter tower as the electron, the track measured in the COT gives a $p_T$ measurement after radiation. There is therefore a long tail in $E/p$ and the cut value is chosen to be $E/p < 2$. The higher the energy of the track, the less reliable the curvature and hence $p_T$ measurement, so the cut is released for electron candidates that have $E_T > 100\,\mathrm{GeV}$.

***$q\Delta x$ and $\Delta z$:*** the separation between the track and cluster at the CES. The CES has good position resolution and can be used to determine how well a track points towards its associated cluster. The track is extrapolated to the plane of the CES and the separation between it and the CES cluster found in $r - z$ plane, $\Delta z$, and in the $r - \phi$ plane, $\Delta x$. The magnetic field in the $r - \phi$ plane gives an asymmetry in bremsstrahling for electrons and positrons, so an asymmetric cut is made on $q\Delta x$ rather than just on $\Delta x$: $-3.0 < q\Delta x < 1.5\,\mathrm{cm}$. The cut on $\Delta z$ is made at $|\Delta z| < 3.0\,\mathrm{cm}$.

Central electron identification cut values are chosen to give close to full efficiency for signal selection, while rejecting background.

Two sets of central electron identification cuts are defined for the analysis: 'tight' and 'loose' cuts, where the tight cuts are always used to select the first electron and the looser requirements are made on the second leg of central-central events. Furthermore a set of 'very tight' central electron cuts is defined for use in the determination of the forward electron efficiencies; this is discussed later. The tight electron cuts are common to the W and Z cross-section analyses, in order that systematic effects cancel in the ratio of the cross-sections.

The cut values are summarised in Table 11, and the $n - 1$ distributions – that is, distributions of selection variables with all cuts applied except for the variable being plotted – are shown in Figures 31 and 32. There is an ongoing effort to improve the simulation of $Lshr$, $Had/EM$ and the isolation fraction, but the agreement seen in these figures is already much better than in earlier versions. Since the efficiencies are measured in data, precise agreement in these distributions is not necessary.

## 4.2. Forward Electron Selection

The COT does not extend far enough forward to provide good coverage for forward electrons, and the complicated coverage provided by silicon tracking introduces large uncer-

| **Variable** | **Very Tight Central**<br>$72\,\mathrm{pb}^{-1}$ [$194\,\mathrm{pb}^{-1}$] | **Tight Central** | **Loose Central** | **Central Cluster** |
|---|---|---|---|---|
| $E_T$ | $> 25$ GeV | | | |
| Fiduciality | fidEle = 1<br>(ie within fiducial region defined by CES: see Section 3.1) | | | |
| $p_T$ | $p_T > 10$ GeV/$c$<br>($>50$ GeV/$c$ for $E_T > 100$ GeV) | | | |
| $z_{vertex}$ | $\lvert z_0^{electron}\rvert < 60.0$ cm | | | |
| Had/EM | $< 0.055 + 0.00045 \times E$ | | | – |
| Track Quality Cuts | at least 3 Axial and 3 Stereo<br>SL with at least 7 hits each | | | –<br>– |
| $E_T^{iso}/E_T$ | $<0.05$ [$<0.02$] | $<0.1$ | $<0.1$ | – |
| L$_{shr}$ | $<0.1$ [$<0.0$] | $<0.2$ | – | – |
| $E/p$ | $E/p < 2.0$ [$E/p < 1.2$] $^{(**)}$ | $E/p < 2.0$ $^{(**)}$ | – | – |
| $\chi^2_{strip}$ | $<10.0$ | | – | – |
| Q$\cdot\Delta X$ | $-3.0 < Q \cdot \Delta X < 1.5$ cm | | – | – |
| $\lvert\Delta Z\rvert$ | $<3.0$ cm | | – | – |

**Table 11:** *Criteria for central electron selection.* $^{(**)}$ *The* $E/p$ *cut is released for electrons that have* $E_T > 100$ *GeV. The reason for having different 'Very Tight' cuts for the 72 and 194* $pb^{-1}$ *datasets is discussed in Section 4.5.2.*

tainties and is therefore used only for reconstructing Z bosons with the highest rapidities (forward-forward), which are not included in all results. Thus for most of this work forward electron identification is based only on calorimetric information, and the variables used are the following:

***Had/EM:*** the same variable as used in central electron selection and described in Section 4.1. In the forward region the selection is $Had/EM < 0.05$.

***Isolation:*** the isolation variable used in forward electron selection is the total energy in a cone of 0.4, excluding the cluster:

$$E_T^{0.4} - E_T^{\mathrm{cluster}} < 4\,\mathrm{GeV} \quad .$$

Energies are adjusted with face corrections as described in Section 2.2.3.2. The isolation energy is also corrected for 'leakage' into adjacent towers outside the cone, using corrections derived from collision data [37].

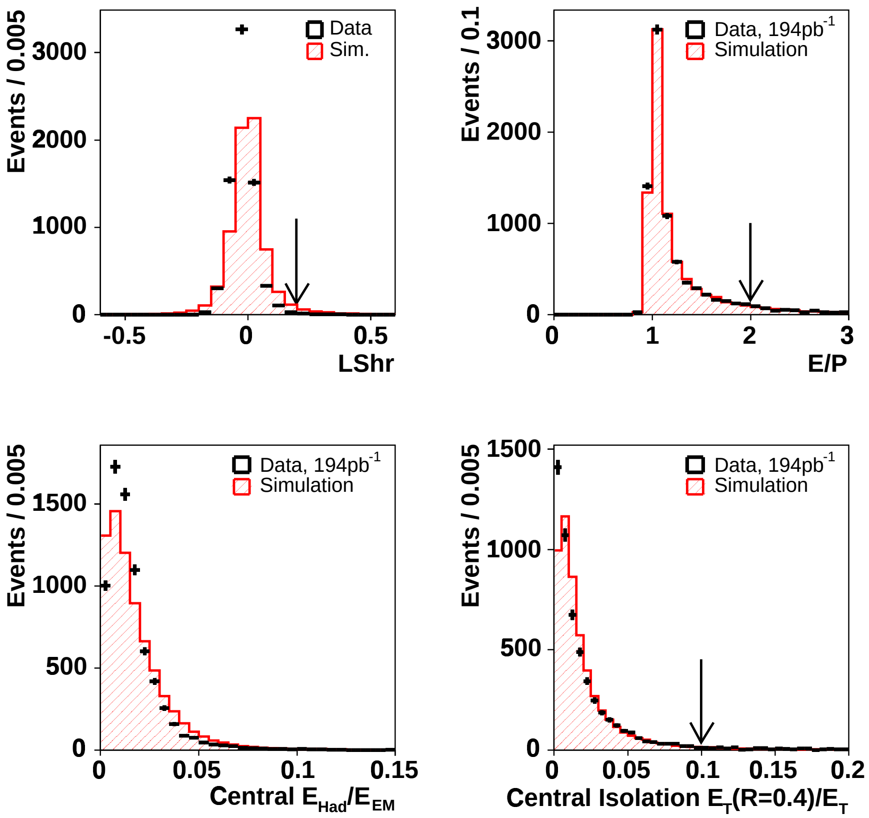

**Figure 31:** *n-1 distributions of central electron identification variables, shown for data (markers) and signal Monte Carlo (histogram). The cut applied on each variable is indicated by the arrow (a sliding cut is applied to $E_{Had}/E_{EM}$).*

**$\chi^2_{\mathrm{PEM}}$:** a shower shape variable. The energies in the towers of the 3×3 PEM cluster are compared to those expected from testbeam, and the $\chi^2$ of the fit used as an identification variable, $\chi^2_{\mathrm{PEM}} < 10$.

As with the central electron identification cuts, cut values are chosen to give high efficiency for signal selection, while rejecting background. The cut values are summarised in Table 12 and $n-1$ distributions are shown in Figure 33.

## 4.3. Efficiency Strategy

The efficiencies of the electron identification cuts are measured directly from the data. As Z decays are two-pronged it is possible after having made a loose kinematic event selection including an invariant mass requirement, to apply tight identification cuts to one leg to

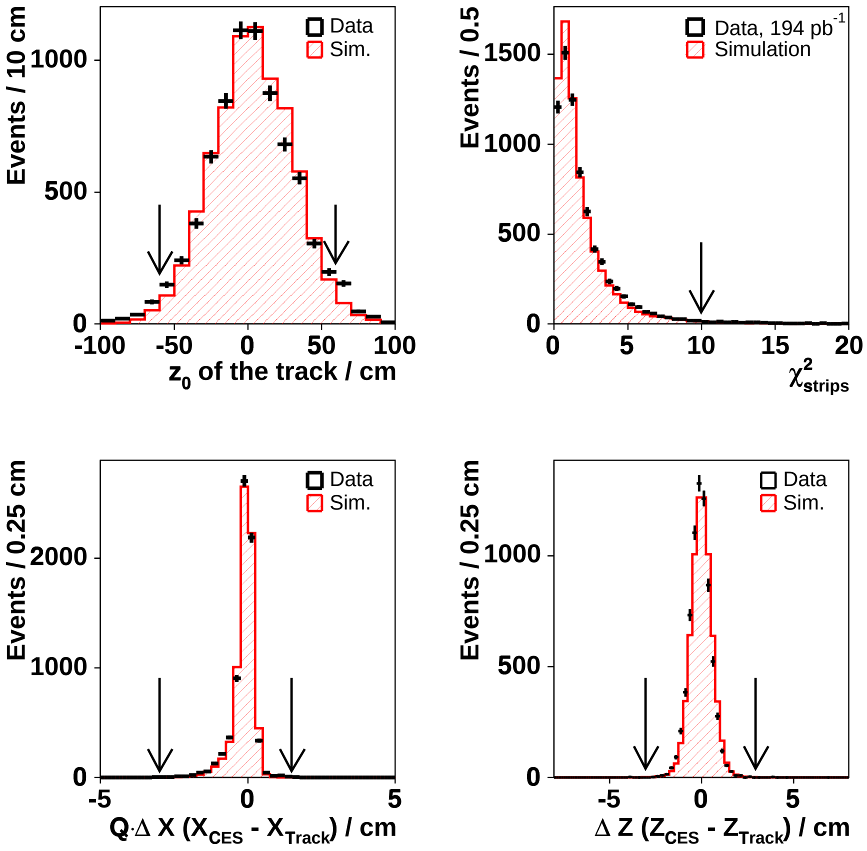

**Figure 32:** *n-1 distributions of central electron variables, shown for data (markers) and signal Monte Carlo (histogram). The cut applied on each variable is indicated by the arrow.*

| Variable | Forward Electron | Forward Cluster |
|---|---|---|
| $E_T$ | $> 20$ GeV | |
| Fiduciality | $1.2 < \|\eta\| < 2.8$ | |
| Had/EM | $< 0.05$ | $< 0.125$ |
| $E_T^{iso}$ | $< 4$ GeV | – |
| $\chi^2_{PEM}$ | <10.0 | – |

**Table 12:** *Criteria for forward electron selection.*

remove much of the background, and then to use the second leg as a probe to measure efficiencies.

The denominator for the efficiency must be the same as the numerator used in the acceptance calculation, as it is the product acceptance×efficiency that is used in the eval-

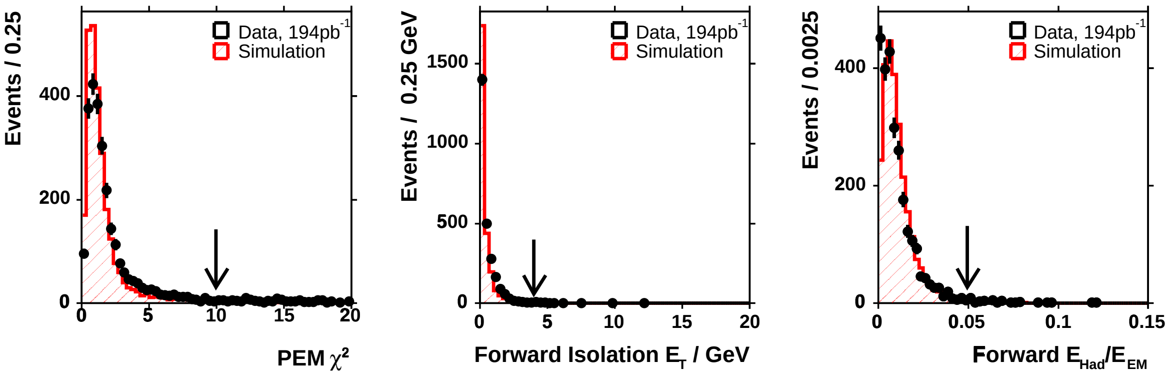

**Figure 33:** *n-1 distributions of forward electron variables, shown for data (markers) and signal Monte Carlo (histogram). The cut applied on each variable is indicated by the arrow.*

uation of the cross-sections. More generally, the identification cut efficiency takes the form

$$\epsilon = \frac{\text{electrons passing all ID cuts}}{\text{electrons passing kinematic cuts}}$$

However it is clear that both the numerator and the denominator of this expression may contain backgrounds, and before evaluating the identification efficiencies it is necessary to have a means of estimating the background contributions.

## 4.4. Backgrounds

Backgrounds to $Z \rightarrow ee$ events include misidentified events in which an object such as a hadron jet fakes an electron, and events with real electrons that have similar topologies to the signal. First of all QCD backgrounds will be considered, and then the electroweak backgrounds $W \rightarrow e\nu$, $Z \rightarrow \tau\tau$ and WW; and also $t\bar{t}$. Examples of lowest-order diagrams for QCD dijet, $W \rightarrow e\nu$ and $Z \rightarrow \tau\tau$ backgrounds to $Z \rightarrow ee$ events are given in Figure 34.

### 4.4.1 QCD Background

The QCD background is defined as events that pass all the cuts, but in which both apparent electrons are faked by jets. Backgrounds of one real electron and one fake electron such as W+jet events are considered in the next section.

Two methods are used to estimate the QCD background. The first, used only in the central region, where tracking information is available, assumes that the QCD background

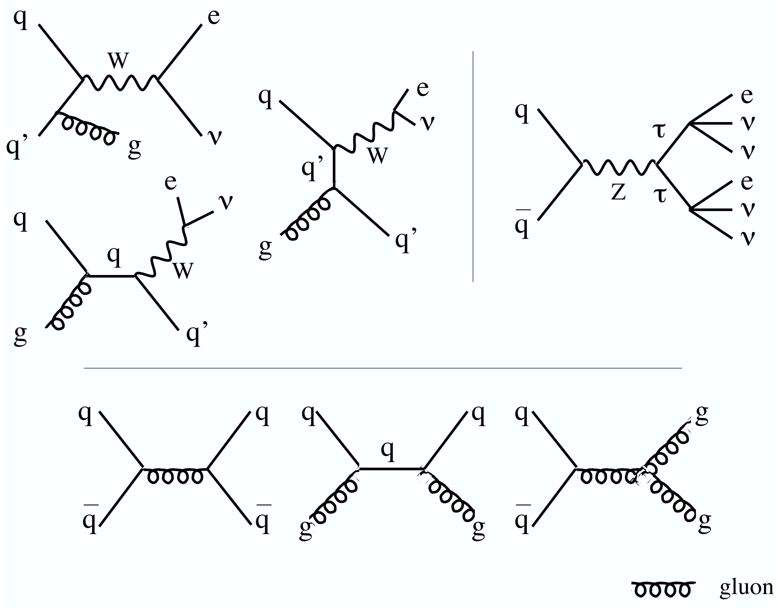

**Figure 34:** *Examples of diagrams of $W \to e\nu$, $Z \to \tau\tau$ and QCD dijet backgrounds to* Z→ee.

is charge-symmetric and that the oppositely-charged component that passes the signal selection requirements may be estimated from the number of events in which both electrons have the same charge (‘same-sign’ events).

As has been described in Section 3.2.2, signal events may also be measured as same-sign events when one electron has given off an energetic photon that has converted. Figure 35 shows the events in the data that pass all analysis cuts except that the two electrons have the same charge. If these events were all QCD background a peak would not be expected at $m_{\mathrm{Z}}$. The number of expected same-sign events is measured from the simulation and subtracted from the number of events observed in the data to give the background estimate. There is a large uncertainty associated with the expected number of same-sign signal events estimated from the simulation but since the background is small this method is adequate.

The second method of estimating the QCD background developed for this analysis is to measure a rate per jet for faking an electron. The fake rates may be convolved with the observed jet distributions to give an estimate of the total background and its shape in rapidity.

A fake rate is defined from the JET_20-triggered sample as the ratio of the number of jets passing central or forward electron cuts to the total number of jets in that region of the detector. Owing to the trigger prescale it is expected that there will be very few real

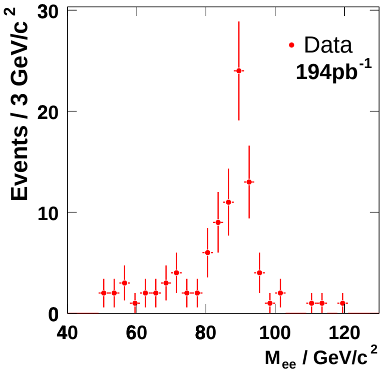

**Figure 35:** *Invariant masses of events passing all selection cuts, except that both electrons have the same charge (data).*

Zs or Ws in this sample, but any Z or W candidates are removed by looking only at events that have fewer than two loose electron candidates, and $\not\!\!E_{\mathrm{T}} < 15\,\mathrm{GeV}$.

Owing to the different clustering algorithms used for electrons and for jets, a jet will fake an electron with energy lower than that of the jet. To take account of this the distribution of $E_T^{\mathrm{ele}}/E_T^{\mathrm{jet}}$ is fitted with a Gaussian function for those jets passing the electron cuts. This scaling may then be applied to all jets, and the rescaled jet energy is referred to as $E_T^{\mathrm{scaled}}$.

Fake rates and energy scalings are obtained for each set of electron cuts used in the analyses: for example the tight and loose electron cuts in the central region, the set of very tight central cuts applied to the central-forward events for the forward efficiency measurements, forward electron analysis cuts, and foward electron kinematic cuts used in the efficiency measurements.

Having obtained the per-jet fake rates and energy scalings they are applied to multi-jet events. For the central-forward events the background is estimated in the following way: if a central jet has $E_T^{\mathrm{scaled}} > 25\,\mathrm{GeV}$ and a plug jet $E_T^{\mathrm{scaled}} > 20\,\mathrm{GeV}$, their (scaled) invariant mass is entered in a dijet mass distribution with weight equal to the product of the fake rates for the two legs, using parameterisations shown in Figure 36 (the forward cluster fake rate histogram is used directly). This is repeated for each combination of electron cuts used in different parts of the analysis.

Examples of the weighted dijet mass distributions are shown in Figure 37.

It is seen from Figure 36 that there is some uncertainty associated with fitting the fake rate. Based on different ways of fitting and on differences in measured fake rates from samples coming from different jet triggers, a systematic uncertainty of 30% is assigned to each fake rate.

The rapidity distribution is also formed from all combinations falling in the appropriate mass window and is shown for central-forward events in Figure 38.

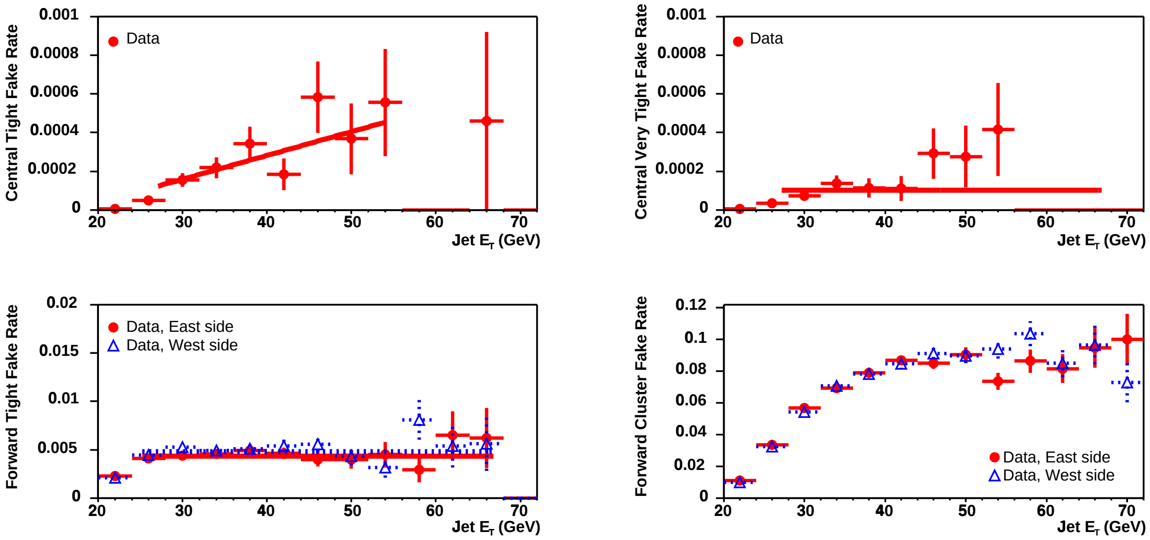

**Figure 36:** *Fake rates for sets of electron cuts used in the analyses (shown for the 72 pb$^{-1}$ dataset). The fake rates are parameterised as shown by lines; the forward cluster fake rate histogram is used directly.*

The background estimate for central-central events using this method is estimated to be 2.4 ± 1.0 events for the 72 pb$^{-1}$ dataset, in good agreement with the 1.6 ± 4.7 events estimated using the same-sign events method.

The background estimates are summarised in Table 13.

### 4.4.2 Non-QCD Backgrounds

Backgrounds from $W \rightarrow e\nu$, $Z \rightarrow \tau\tau \rightarrow ee\nu\nu\nu\nu$, WW, WZ and $t\bar{t}$ are estimated by generating and fully simulating large samples of each, applying all of the analysis cuts to see how many events pass, and then rescaling by the cross-section for each process. $W \rightarrow e\nu$ and $Z \rightarrow \tau\tau$ samples are generated using Pythia, $t\bar{t}$ using Herwig [38], and WW/WZ using Pythia.W$\gamma$ is checked separately with a specially-generated dataset $W\gamma \rightarrow e\nu\gamma$ using

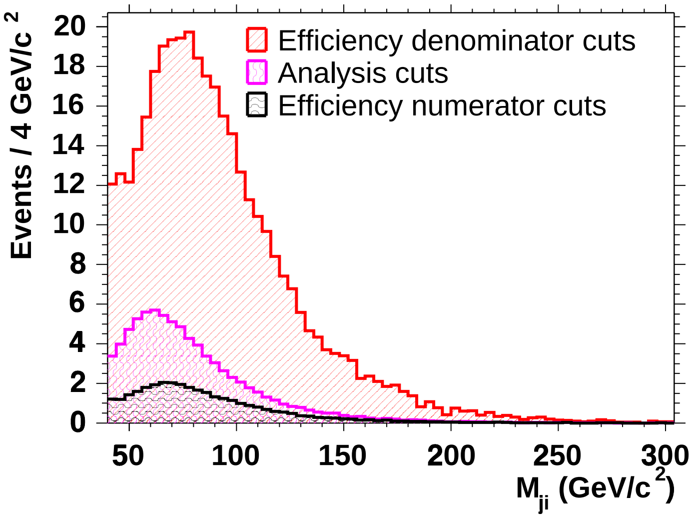

**Figure 37:** *Weighted dijet mass distributions for QCD background estimates used in total cross-section and forward efficiency measurements; shown for 72 pb$^{-1}$ dataset.*

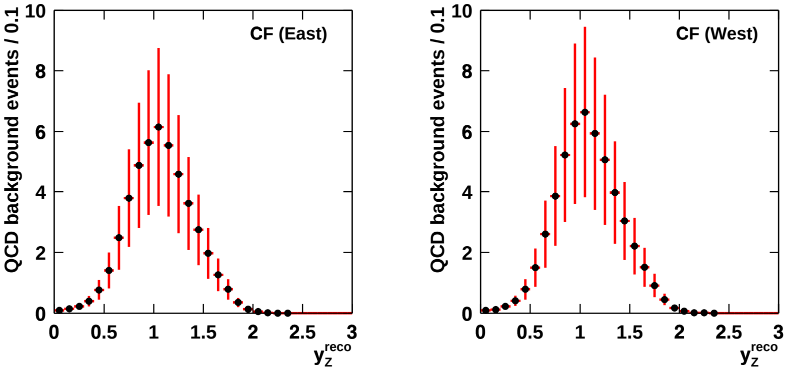

**Figure 38:** *Rapidity distribution of QCD background estimate for central-forward events (194 pb$^{-1}$ dataset).*

Uli Baur's NLO program [39], to verify that the PYTHIA inclusive W dataset does not underestimate the background to Z → ee.

The WW, WZ and $t\bar{t}$ contributions are found to be negligible. The total background is determined by writing

$$N^{\mathrm{signal}}_{\mathrm{e^+e^-}} = N^{\mathrm{candidates}}_{\mathrm{e^+e^-}} - N_{\mathrm{Z}\tau\tau} - N_{\mathrm{We}\nu} - N_{\mathrm{QCD}}. \tag{4.4.1}$$

Then

$$N_{\mathrm{Z}\tau\tau} = N^{\mathrm{signal}}_{\mathrm{e^+e^-}} \cdot \frac{r_{\mathrm{Z}\tau\tau}}{r_{\mathrm{Zee}}} \tag{4.4.2}$$

and

$$N_{\mathrm{We}\nu} = N^{\mathrm{signal}}_{\mathrm{e^+e^-}} \cdot \frac{r_{\mathrm{We}\nu}}{r_{\mathrm{Zee}}} \cdot R \tag{4.4.3}$$

where $r_{\mathrm{Zee}}$, $r_{\mathrm{Z}\tau\tau}$ and $r_{\mathrm{We}\nu}$ are the fractions of the Monte Carlo events passing the selection criteria and $R$ is the ratio of the cross-sections $\sigma_{\mathrm{W}} \cdot Br(\mathrm{W} \rightarrow \mathrm{e}\nu) : \sigma_{\mathrm{Z}} \cdot Br(\mathrm{Z} \rightarrow \mathrm{ee})$.

Solving this system of equations and using the theoretical value of $R$, $R = 10.67 \pm 0.15$, results in the background estimates shown in Table 13.

| | $72\,\mathrm{pb}^{-1}$ $(194\,\mathrm{pb}^{-1})$ | | | | | |
|---|---|---|---|---|---|---|
| source | central-central | | central-forward | | total | |
| QCD dijet | $1.6 \pm 7^{(\dagger)}$ | $(3.0 \pm 1.3)^{(\dagger)}$ | $39 \pm 17$ | $(98 \pm 42)$ | $41 \pm 24$ | $(101 \pm 42)$ |
| $\mathrm{W} \rightarrow \mathrm{e}\nu$ | $1.5 \pm 0.9$ | $(4.0 \pm 2.4)$ | $15.3 \pm 2.6$ | $(41.1 \pm 7.0)$ | $17 \pm 4$ | $(45 \pm 7)$ |
| $\mathrm{Z} \rightarrow \tau\tau$ | $1.4 \pm 0.3$ | $(3.8 \pm 0.8)$ | $2.3 \pm 0.3$ | $(6.2 \pm 0.8)$ | $4 \pm 1$ | $(10 \pm 1)$ |
| WW | $[\,0.59 \pm 0.01$ | $(1.57 \pm 0.02)\,]$ | $[\,0.63 \pm 0.01$ | $(1.70 \pm 0.02)\,]$ | | |
| WZ | $[\,0.98 \pm 0.02$ | $(2.62 \pm 0.05)\,]$ | $[\,1.10 \pm 0.02$ | $(2.95 \pm 0.05)\,]$ | | |
| $\mathrm{t\bar{t}}$ | $[\,0.44 \pm 0.02$ | $(1.17 \pm 0.05)\,]$ | $[\,0.27 \pm 0.02$ | $(1.17 \pm 0.05)\,]$ | | |
| total | $4.5 \pm 7.1$ | $(10.8 \pm 2.7)$ | $57 \pm 17$ | $(145 \pm 43)$ | $62 \pm 18$ | $(156 \pm 43)$ |

**Table 13:** *Summary of backgrounds, shown separately for the 72 and 194* $\mathrm{pb}^{-1}$ *datasets. Diboson and top backgrounds are not included in totals.* ( $^{(\dagger)}$ *Central-central QCD background: same-sign method used for* $72\,\mathrm{pb}^{-1}$ *and fake rate method used for* $194\,\mathrm{pb}^{-1}$*.)*

## 4.5. Electron Identification Efficiencies

The strategy for obtaining electron identification efficiencies was outlined in Section 4.3 and for estimating the background to any set of electron selection criteria in Section 4.4. In this section the efficiencies for central and forward electron selection are calculated.

### 4.5.1 Central Electron Identification Efficiencies

To measure the central electron identification efficiencies, the tight electron requirements of Table 11 are applied to one leg, the geometric and kinematic cuts of $E_T > 25\,\mathrm{GeV}$, $p_T > 10\,\mathrm{GeV}/c$ and fiduciality are applied to the second leg, and opposite sign and tight invariant mass cuts are made ($75 < m_{\mathrm{ee}} < 105\,\mathrm{GeV}/c^2$).

The number of events passing these requirements is labelled $N_{CC}$. The other cuts of Table 11 are applied to find the number of events $N_{Ti}$ in which the second electron candidate passes the $i^{th}$ cut, and in particular the numbers of events $N_{TL}$ in which the second candidate passes all of the loose cuts, and the number $N_{TT}$ in which both candidates pass all of the tight cuts.

The total number of Z→ee events is labelled $N$, $\epsilon_T$ is the probability for a single electron to pass the tight cuts, $\epsilon_L$ the probability for an electron to pass the loose cuts, and $\epsilon_{L\overline{T}} = \epsilon_L - \epsilon_T$ the probability for an electron to pass the loose cuts but not the tight cuts.

Then as the second electron candidate may or may not pass the tight cuts and there are two orderings, $N_{CC}$ may be written

$$N_{CC} = (2\epsilon_T(1 - \epsilon_T) + \epsilon_T^2) \cdot N. \tag{4.5.1}$$

Also,

$$N_{TT} = \epsilon_T^2 \cdot N. \tag{4.5.2}$$

The efficiency for central-central Z event selection may be written

$$\begin{aligned} \epsilon_{\mathrm{Z}} &= \epsilon_T\epsilon_T + \epsilon_T\epsilon_{L\overline{T}} + \epsilon_{L\overline{T}}\epsilon_T \\ &= \epsilon_T^2 + 2\epsilon_T(\epsilon_L - \epsilon_T) \\ &= \epsilon_T(2\epsilon_L - \epsilon_T) \ \ . \end{aligned} \tag{4.5.3}$$

It follows that

$$N_{TL} = \epsilon_T(2\epsilon_L - \epsilon_T) \cdot N. \tag{4.5.4}$$

Solving Equations 4.5.1, 4.5.2 and 4.5.4:

$$\epsilon_L = \frac{N_{TL} + N_{TT}}{N_{CC} + N_{TT}} \quad \text{and} \quad \epsilon_T = \frac{2N_{TT}}{N_{CC} + N_{TT}}, \tag{4.5.5}$$

and in general

$$\epsilon_i = \frac{N_{Ti} + N_{TT}}{N_{CC} + N_{TT}}. \tag{4.5.6}$$

Backgrounds are subtracted from $N_{Ti}$ and $N_{CC}$ by counting the number of corresponding same-sign events and correcting by the expected number of events from the simulation, as described in Section 4.4.

Uncertainties are evaluated by re-expressing the efficiencies in terms of the independent quantities $A_1 = N_{TL} - N_{TT}$, $A_2 = N_{TT}$, and $A_3 = N_{CC} - N_{TL}$, and computing

$$\delta(\epsilon) = \sqrt{\sum_{j=1}^{3} \left( \frac{\partial \epsilon}{\partial A_j} \delta(A_j) \right)^2}. \tag{4.5.7}$$

The $A_i$ are large enough to assume Gaussian uncertainties $\sqrt{A_1}$, $\sqrt{A_2}$ and $\sqrt{A_3}$ respectively.

Efficiencies are given in Table 14.

It is found that the central electron identification efficiencies have an $E_T$ dependence, as shown in Figure 39. The $E_T$-dependent efficiencies are obtained in a slightly different way from the total efficiencies, to avoid bias. As the electron candidates of an event are ordered in $E_T$ it is not sufficient to look for one leg passing all cuts, use a second leg as a probe and then, as previously described, correct for having already selected one leg. Instead, the kinematic 'central cluster' cuts of Table 11 are made on two electron candidates, a mass window cut is applied and then the tight cuts are applied to one of the two candidates, selected randomly according to whether the event number is odd or even. If that candidate passes the tight cuts, the event enters the efficiency calculation denominator, and the other leg is used as an unbiased probe.

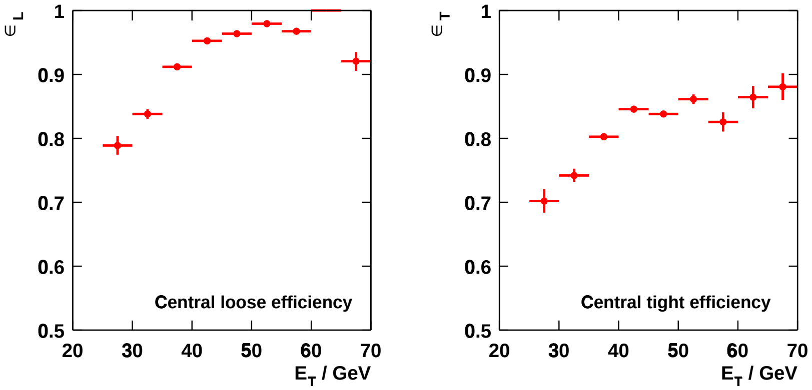

**Figure 39:** *$E_T$ dependence of central electron efficiencies, shown for 194 $pb^{-1}$ dataset.*

As the efficiencies are measured from the central-central Zs the $E_T$ dependence need not be considered for the cross-section measured from central-central Zs. However as shown in Figure 17 the $E_T$ spectrum for the central leg of central-forward Zs is much lower than for central-central Zs. A correction factor for the central efficiency is determined from the simulation to be $\epsilon_T^{\text{CF correction}} = 1.014 \pm 0.002$, to be used $\epsilon_T^{(\text{CF})} = \epsilon_T^{\text{CF correction}} \cdot \epsilon_T$.

Obtaining the correction factor from the simulation takes into account not only that the $E_T$ spectra are different in the CC and CF cases, but also that the electrons look different in the two cases: the $E_T$ spectrum for CF events is simply shifted lower than for CC events but in addition, lower $E_T$ electrons in CC events are likely to have radiated and thus have a lower measured efficiency than the low $E_T$ electrons in CF events.

These effects must be considered carefully in the determination of the ID efficiencies as a function of rapidity, to be used in the measurement of $\frac{d\sigma}{dy}$. The tight and loose electron $E_T$ spectra are obtained in each bin of generator-level rapidity of the Z ($y_Z^{gen}$) for CC events, and convolved with the efficiencies measured as a function of $E_T$ shown in Figure 39 to give $\epsilon_T(y)$ and $\epsilon_L(y)$. Similarly the $E_T$ spectra of the central legs of CF events are obtained in each rapidity bin and convolved with $\epsilon_T(E_T)$, but in this case a correction is also made for $\epsilon_T^{CF}(E_T)/\epsilon_T^{CC}(E_T)$, taken from the simulation. The correction is shown in Figure 40.

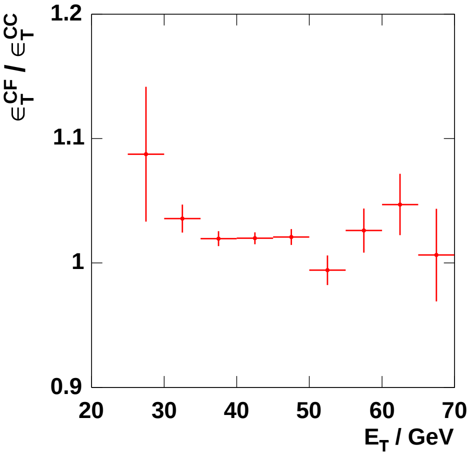

**Figure 40:** *Correction to central electron efficiency $E_T$ dependence for central-forward events.*

To check that the simulation models well the $E_T$ spectra in each bin of rapidity, the $E_T$ spectra are compared in data and simulation for bins of reconstructed rapidity of the Z, $y_Z^{reco}$ in Figures 41 and 42 and as can be seen the agreement is reasonably good.

Furthermore the efficiency as a function of $E_T$ is examined in bins of electron $|\eta|$, as shown in Figure 43. A fairly wide spread is seen and so the same quantity is checked in simulation, also shown in Figure 43. Although the simulation is expected to model the efficiency well in the central region, the 'ordering' of the $\eta$ bins does not match well between data and simulation and the uncertainties in data are large. Rather than using these measurements in bins of $\eta$, an extra systematic uncertainty is added to the efficiency measured as a function of $E_T$ as used for the rapidity measurement: the uncertainties on the efficiencies as a function of $E_T$ are inflated by a factor of three to match the spread in bins of $\eta$ seen in the simulation.

Efficiencies as a function of $y_Z^{gen}$ are shown in Figure 44.

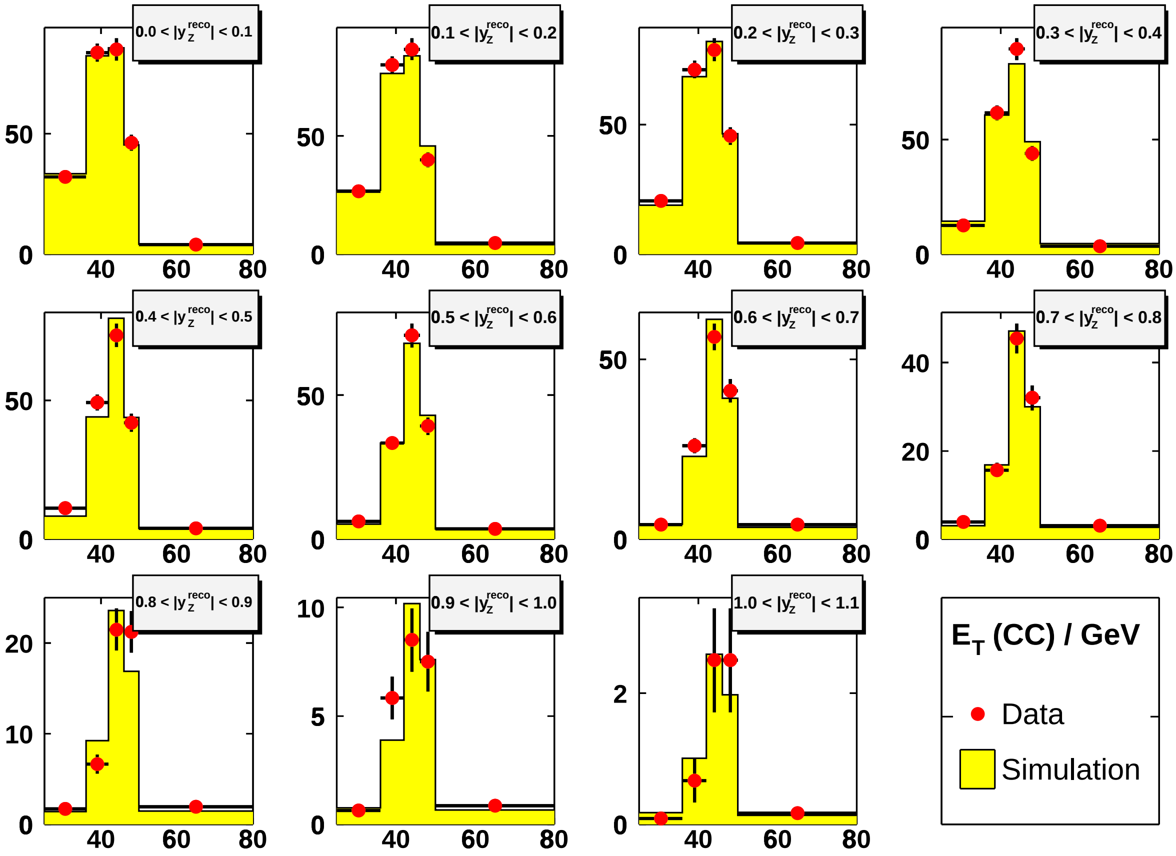

**Figure 41:** *Central electron $E_T$ in bins of the absolute reconstructed rapidity of the Z (CC events). Unequal bins corrected to events/GeV.*

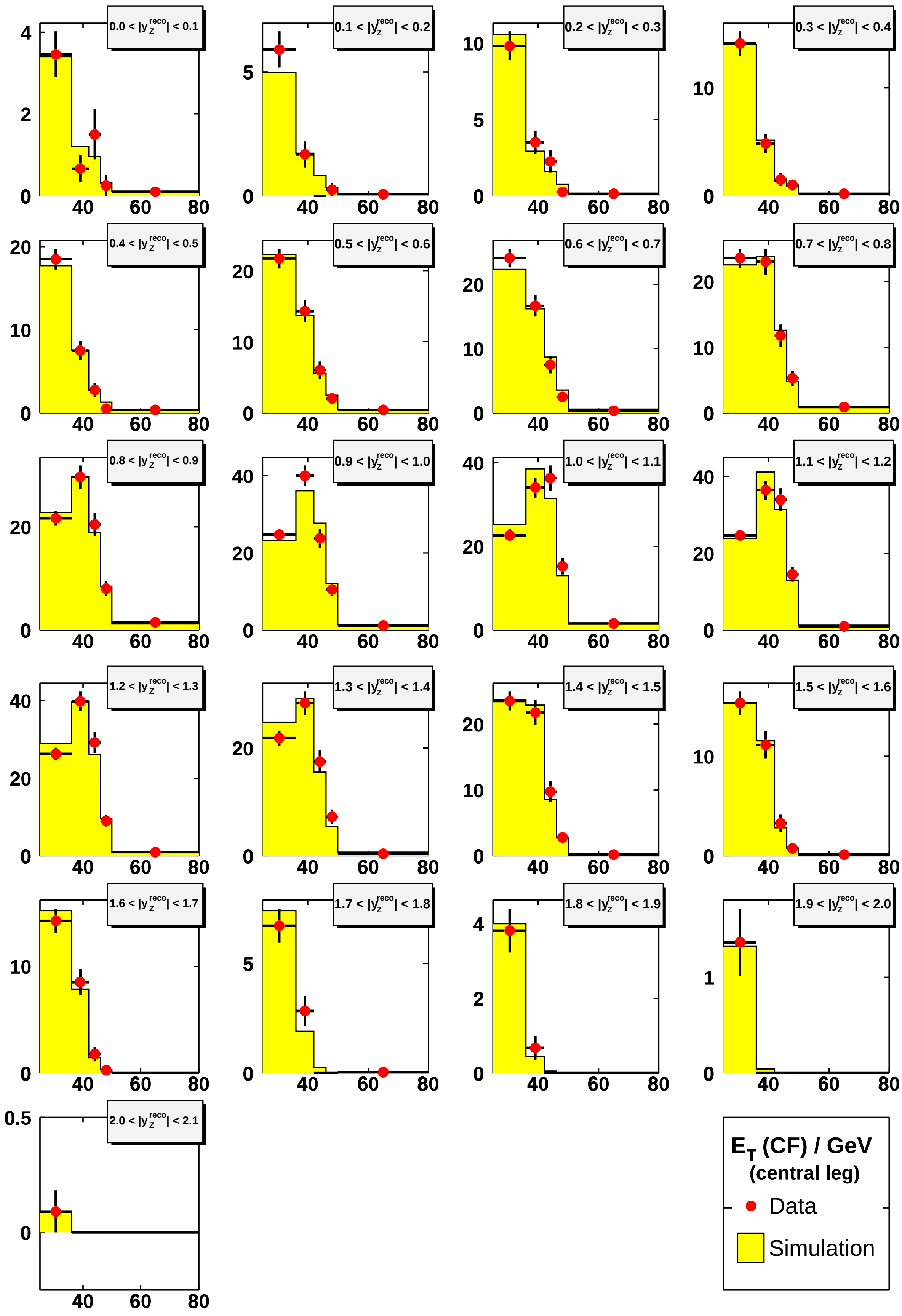

**Figure 42:** *Central electron $E_T$ in bins of the absolute reconstructed rapidity of the Z (CF events). Unequal bins corrected to events/GeV.*

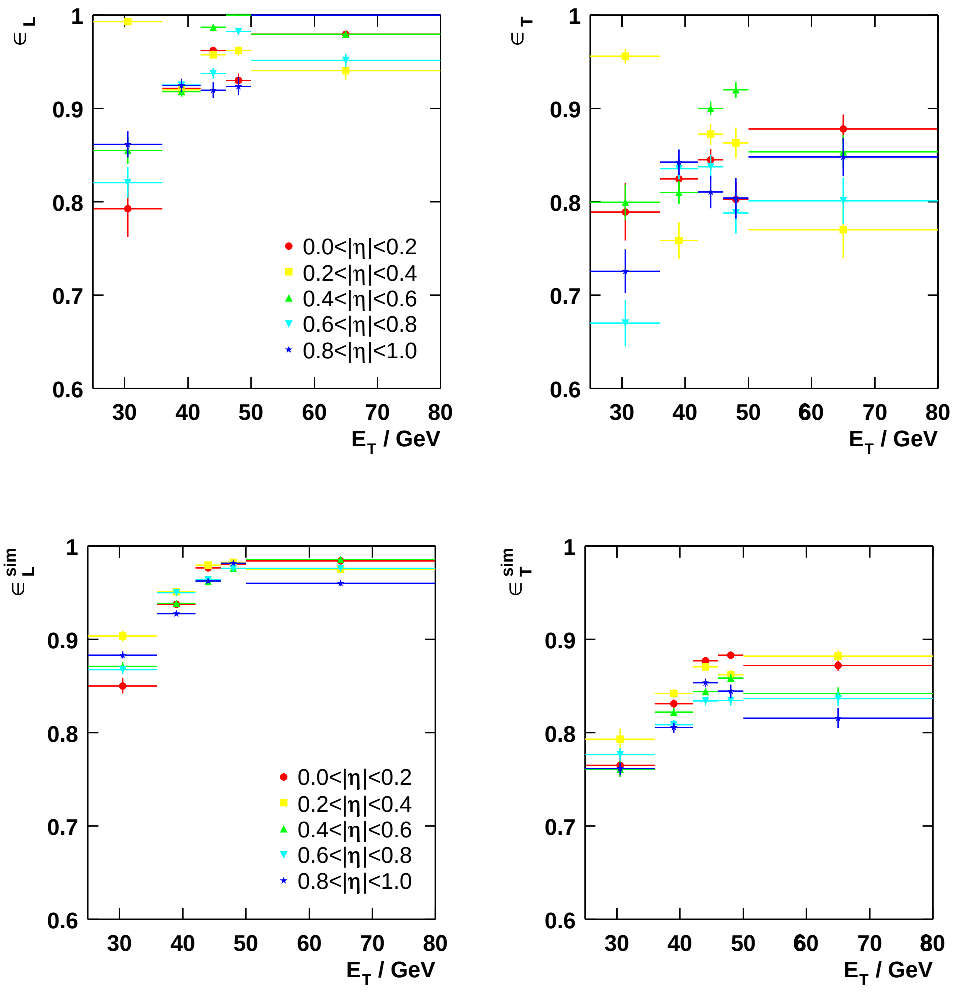

**Figure 43:** *$E_T$ dependence of central electron efficiencies, shown for 194 $pb^{-1}$ dataset and measured in bins of $\eta$ for the loose cuts (left) and the tight cuts (right), in data (top) and simulation (bottom).*

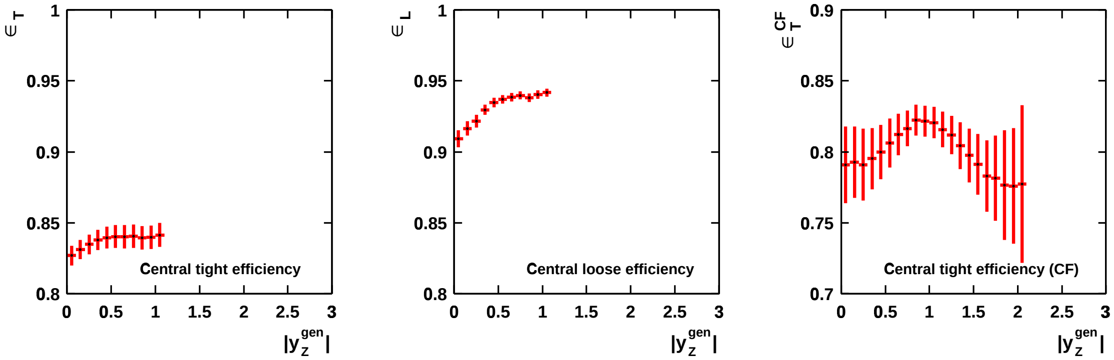

**Figure 44:** *Rapidity dependence of central electron efficiencies.*

### 4.5.2 Forward Electron Identification Efficiency

The forward electron identification efficiency $\epsilon_F$ is more straightforward to obtain than the central efficiencies as the selection of the central leg of central-forward events is independent of the forward leg used as the probe. However even more care must be taken over the backgrounds, which are greater.

The very tight electron requirements of Table 11 are applied to one leg, the forward geometric and kinematic cuts of $E_T > 20\,\mathrm{GeV}$ and fiduciality are applied to the second leg, and a tight invariant mass cut is made ($80 < m_{\mathrm{ee}} < 100\,\mathrm{GeV}/c^2$). The systematic uncertainty from the background subtraction is large and scales with the number of background events. Thus removing as much background as possible using the central selection and the mass window reduces the systematic uncertainty on the efficiency. The tightened central electron cuts and mass window are chosen to balance the final systematic and statistical uncertainties and give the lowest total uncertainty. This is the reason for further tightening the 'very tight' central electron cuts for the $194\,\mathrm{pb}^{-1}$ dataset with respect to those used for the $72\,\mathrm{pb}^{-1}$ dataset. It is verified from the simulation that the tightened invariant mass cut does not bias the efficiency measurement. The efficiency is given in Table 14.

As part of this work the forward electron efficiencies were measured using slightly different selection requirements in order to be used in many other CDF analyses, such as top quark and diboson cross-section measurements [31].

As with the central electron identification efficiencies, an $E_T$ dependence is seen for the forward electrons, as shown in Figure 45. This is important for the rapidity distribution, as the $E_T$ spectrum is changing from bin to bin. Again the simulation is used to find the $E_T$ spectrum for forward electrons passing acceptance cuts in each bin of generator-level rapidity of the Z ($y_Z^{gen}$). The efficiencies are measured as a function of $E_T$ as shown in Figure 45. Again the $E_T$-dependent efficiencies are checked in bins of $\eta$ as shown in Figure 46 and an extra systematic uncertainty is added to cover the spread: the uncertainties on the efficiency as a function of $E_T$ are inflated by a factor of three.

The dependences of the total and $n-1$ efficiencies on run-number, $\eta$ and $\phi$ are given at the end of this section in Figures 51 and 52. It is seen that the efficiencies are fairly stable with time, but that the simulation does not model the $\eta$ dependence very well, nor the overall scale.

However the $E_T$ spectra should be modeled well in the simulation and to check this, the $E_T$ spectra for the forward electrons are compared in data and simulation for bins of reconstructed rapidity of the Z, $y_Z^{reco}$ in Figure 47.

Finally the $E_T$-dependent forward identification efficiency is convolved with the $E_T$ disbributions to give the rapidity dependence of the efficiency, shown in Figure 48.

| | $72\,\mathrm{pb}^{-1}$ | $194\,\mathrm{pb}^{-1}$ |
|---|---|---|
| $\epsilon_L$ | $0.934 \pm 0.005$ | $0.939 \pm 0.002$ |
| $\epsilon_T$ | $0.818 \pm 0.007$ | $0.827 \pm 0.005$ |
| $(\epsilon_T^{\mathrm{CF\ correction}})$ | $(1.014 \pm 0.002)$ | $(1.014 \pm 0.002)$ |
| $\epsilon_F$ | $0.871 \pm 0.015$ | $0.874 \pm 0.007$ |

**Table 14:** *Single-electron identification efficiencies, shown separately for the 72 and 194* $\mathrm{pb}^{-1}$ *datasets.* $\epsilon_T^{\mathrm{CF\ correction}}$ *is a correction to* $\epsilon_T$ *to be applied in central-forward events, to take account of the different central electron* $E_T$ *distributions in central-central and central-forward events.*

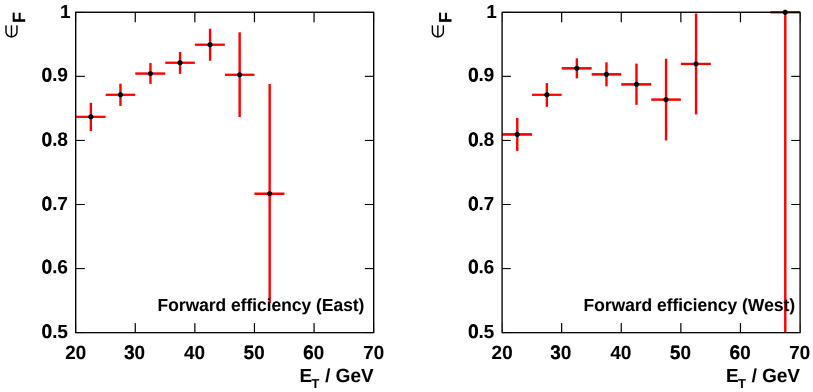

**Figure 45:** $E_T$ *dependence of forward electron efficiencies.*

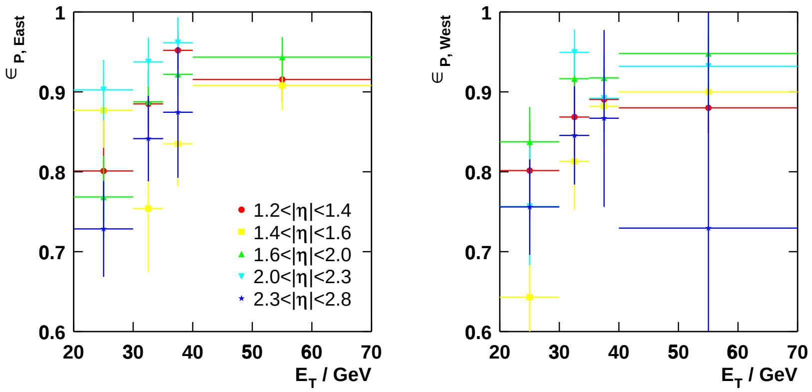

**Figure 46:** *$E_T$ dependence of forward electron efficiencies, measured in bins of $\eta$ on the East side (left) and the West (right).*

#### 4.5.2.1 Forward Electron Tracking Efficiency and Forward-Forward Backgrounds

Forward-forward events selected only using calorimetric information are found to have a large background that is difficult to model. In order to clean up the forward-forward sample, the additional requirement is made that one of the candidate clusters have a silicon stand-alone track associated with it. The associated efficiency is a convolution of the silicon tracking coverage and the track-finding efficiency. Although in the sense that the terms have been used here the silicon coverage is a quantity that is more acceptance-like than efficiency-like, the coverage is in practice complicated and not well-modeled in the simulation and must therefore be measured in data.

The tracking efficiency is measured from the forward legs of central-forward events and is defined as:

$$\epsilon = \frac{\text{electrons passing all calorimetric ID cuts and having an associated silicon track}}{\text{electrons passing all calorimetric ID cuts}}.$$

The efficiency is measured as a function of $\eta$ and convolved with $\eta$ distributions from the simulation to give the efficiency as a function of boson rapidity; both distributions are shown in Figure 49.

The $E_T$ spectra of forward-forward events are compared in data and simulation in bins of reconstructed rapidity of the Z in Figure 50 and are found to be in reasonable agreement.

The fake rate for forward electrons with an associated silicon track is measured from jet data in the same way as the other fake rates described in Section 4.4.1, and is found to be $0.0002 \pm 0.0002$. When combined with the fake rate for forward tight electrons and all dijet events having two jets with $E_T > 30\,\mathrm{GeV}$, this translates into an estimated QCD background for forward-forward events of $0 \pm 1$ events for $191\,\mathrm{pb}^{-1}$. This is lower than the corresponding central-central background estimate owing to the higher $E_T$ requirement on the two legs.

The non-QCD backgrounds to forward-forward events are determined from the simulation, as described in Section 4.4.2. This relies on the modeling of the silicon detector acceptance and efficiency in the simulation, but the backgrounds are found to be so small that this method is sufficient. The $\mathrm{W} \to \mathrm{e}\nu$ background is found to be negligible, and the $\mathrm{Z} \to \tau\tau$ background is estimated to be $4 \pm 2$ events for the $191\,\mathrm{pb}^{-1}$ dataset.

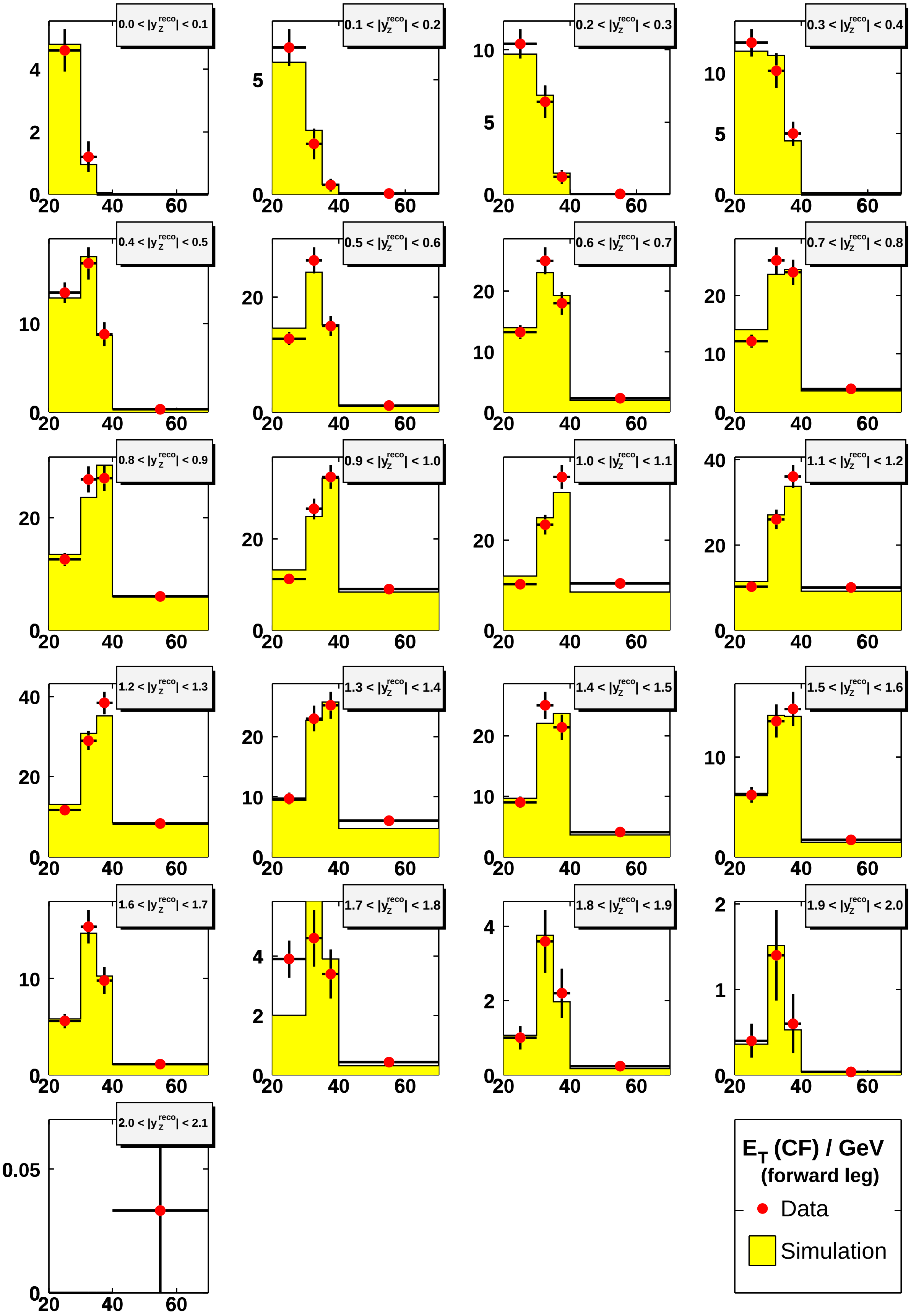

**Figure 47:** *Forward electron $E_T$ in bins of absolute reconstructed rapidity of the Z (CF events). Unequal bins corrected to events/GeV.*

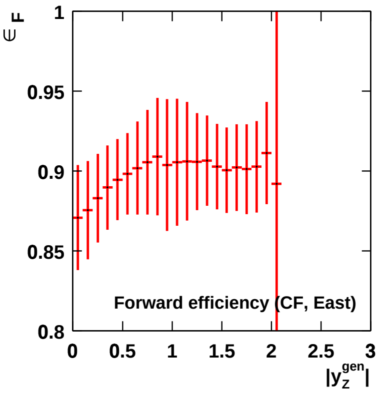

**Figure 48:** *Rapidity dependence of forward electron efficiencies.*

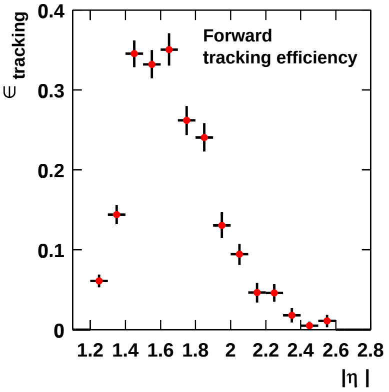

**Figure 49:** *Forward electron tracking efficiency as a function of [left] electron $\eta$ and [right] boson rapidity.*

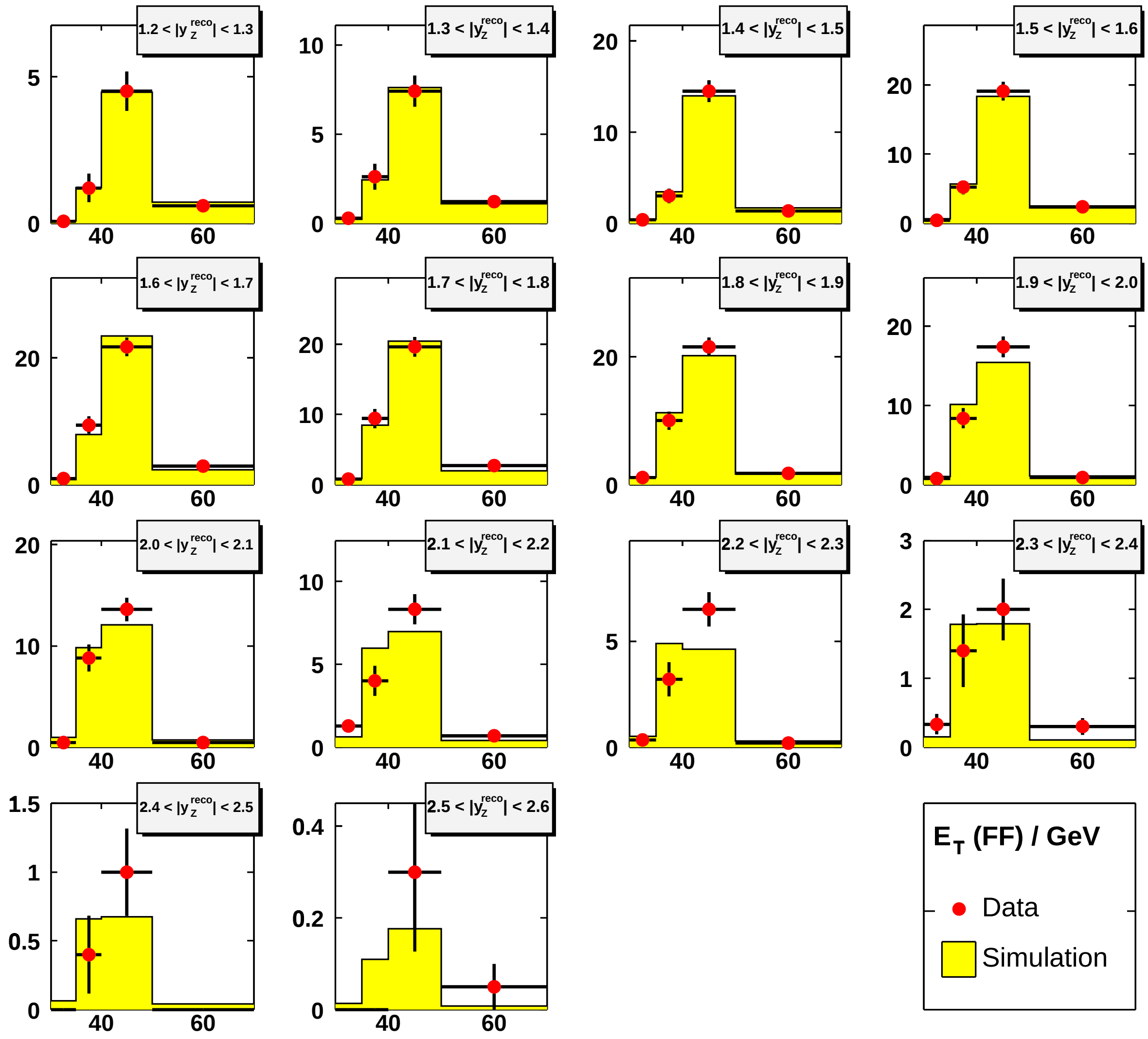

**Figure 50:** *Forward electron $E_T$ in bins of absolute reconstructed rapidity of the Z (FF events). Unequal bins corrected to events/GeV.*

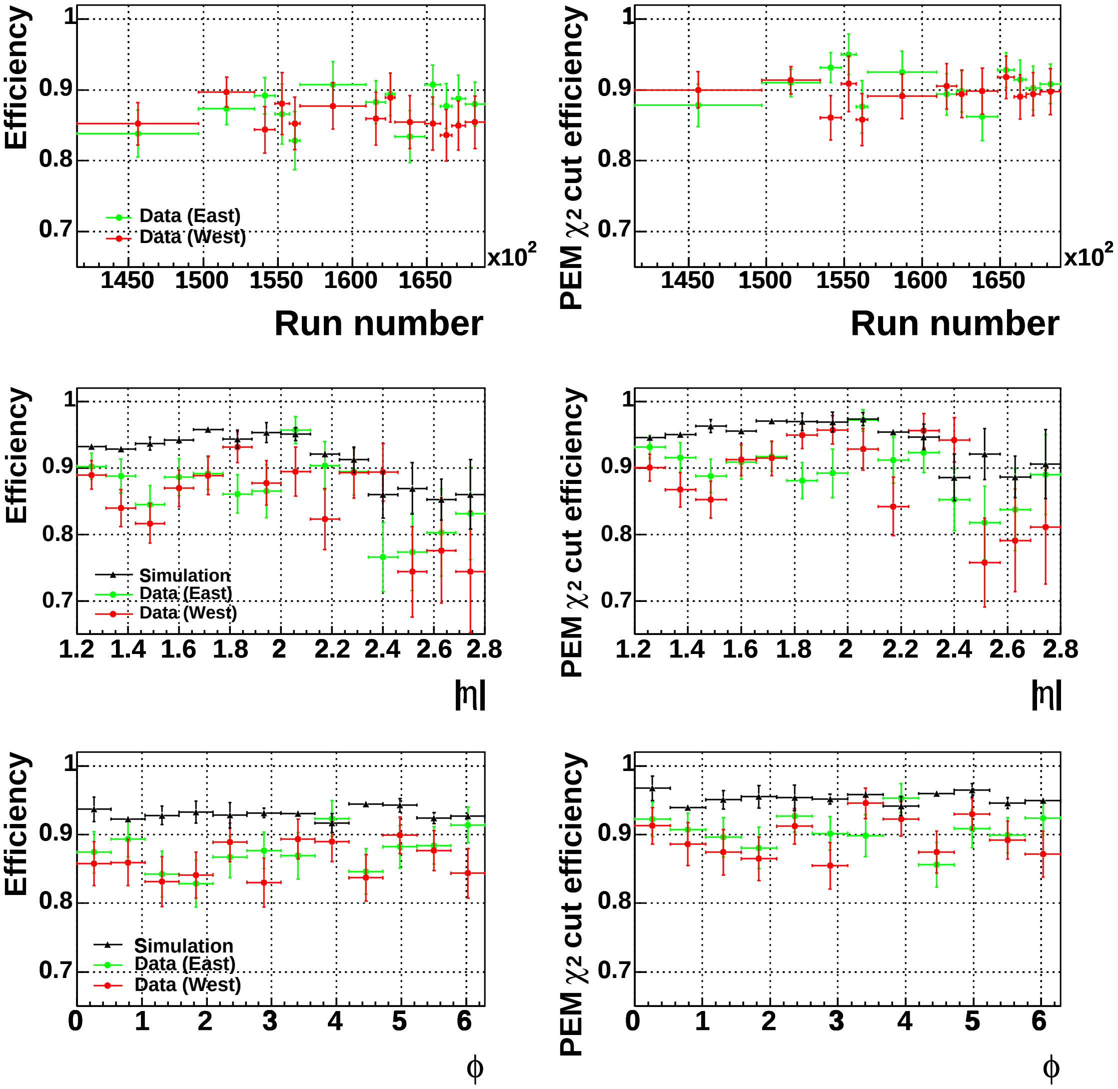

**Figure 51:** *Forward total and $n-1(\chi^2)$ electron identification efficiencies as functions of run number, $\eta$ and $\phi$, shown for data (green East and red West plugs) and signal Monte Carlo (black). Bins of runnumber contain approximately equal numbers of events.*

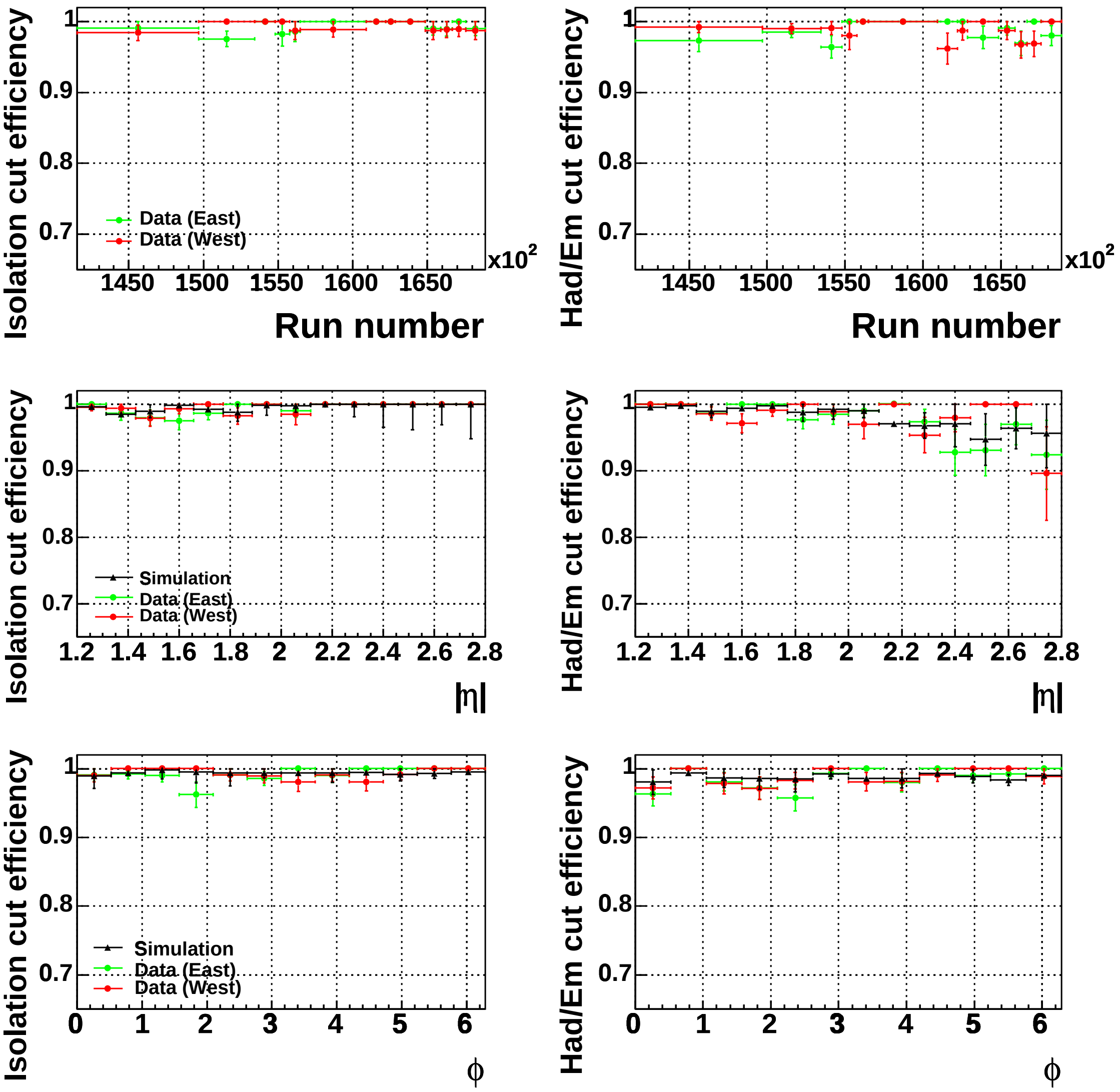

**Figure 52:** *Forward $n-1$ (isolation and Had/EM) electron identification efficiencies as functions of run number, $\eta$ and $\phi$, shown for data (green East and red West plugs) and signal Monte Carlo (black). Bins of run number contain approximately equal numbers of events.*

## 4.6. Electron Reconstruction Efficiencies

The acceptance calculation described in Chapter 3 determines from the simulation the number of $\mathrm{Z} \to \mathrm{ee}$ events reconstructed with the geometric and kinematic cuts used in the analysis. This chapter is concerned with the measurement from the data of the efficiency of electron selection variables applied to reconstructed electron candidates. However to make these acceptance and efficiency numbers match up before they may be multiplied together, there must be a correction made for any difference between data and simulation in the efficiency of reconstructing electrons at all.

**Track Reconstruction** The efficiency for track reconstruction is measured by the Tracking Group by identifying $\mathrm{W} \to \mathrm{e}\nu$ candidates from the W_NOTRACK trigger using only calorimetric information, and then seeing how often there is a matching COT track. In order to reduce background an independently reconstructed silicon track is also required to point towards the electron candidate. The efficiency is found to be $\epsilon_{\mathrm{COT}}^{\mathrm{data}} = 99.63^{+0.35}_{-0.40}\%$, and the corresponding number in simulation is $\epsilon_{\mathrm{COT}}^{\mathrm{sim}} = 99.66^{+0.15}_{-0.24}\%$. The appropriate tracking efficiency term to appear in the overall efficiency for finding Z boson events is therefore

$$\epsilon_{tracking} = \frac{\epsilon_{\mathrm{COT}}^{\mathrm{data}}}{\epsilon_{\mathrm{COT}}^{\mathrm{sim}}} = 1.000 \pm 0.004.$$

**Calorimeter Cluster Reconstruction** The calorimeter cluster reconstruction efficiency is checked by Giulia Manca [34] by looking at events with one very tight electron and a second track passing tight track cuts that forms a Z boson candidate with the first electron in the tight invariant mass window ($80 < M_{\mathrm{e-track}} < 100\,\mathrm{GeV}/c^2$). The cluster reconstruction efficiency is then the fraction of these events that has a calorimeter cluster reconstructed within $\Delta R < 0.4$ of the track. The efficiencies are found to be $\epsilon_{\mathrm{EMC}}^{\mathrm{data}} = 99.0 \pm 0.4\%$ and $\epsilon_{\mathrm{EMC}}^{\mathrm{sim}} = 99.2 \pm 0.1\%$ so the cluster reconstruction term in the cross-section calculation is

$$\epsilon_{clustering} = \frac{\epsilon_{\mathrm{EMC}}^{\mathrm{data}}}{\epsilon_{\mathrm{EMC}}^{\mathrm{sim}}} = 0.998 \pm 0.004.$$

Investigations of the invariant mass reconstructed between central tight electrons and forward silicon tracks showed it to be very broad and the background difficult to understand, so this method cannot be applied to find a forward electron reconstruction efficiency. Instead Eva Halkiadakis checked that there were no hot or dead phototubes found by the Calorimeter Group in the forward detectors in any of the runs used in the analysis, and the forward cluster reconstruction efficiency is assumed to be 100% [32].

## 4.7. Electron Trigger Efficiencies

### 4.7.1 Central Electron Trigger Efficiency

As mentioned in Section 2.2.5.1, trigger efficiencies are measured by comparing the numbers of events passing the principal trigger to those passing 'backup triggers' consisting of elements of the principal trigger.

The total and $E_T$-dependent trigger efficiency measurements described here were made by the LBNL group [33], using ntuples provided by this author.

The principal ELECTRON_CENTRAL_18 trigger has been described in Section 2.2.5.1. The three backup triggers are the W_NOTRACK, W_NOTRACK_NO_L2, and INCLUSIVE MUON. The triggers are compared in Table 15.

| | ELECTRON_CENTRAL_18 | ELECTRON_CENTRAL_18_NOL2 | W_NOTRACK | W_NOTRACK_NO_L2 | INCLUSIVE MUON |
|---|---|---|---|---|---|
| L1 | CEM cluster, $E_T > 8\,\mathrm{GeV}$<br>XFT track, $p_T > 8\,\mathrm{GeV}/c$ | CEM clus, $E_T > 8\,\mathrm{GeV}$<br>XFT trk, $p_T > 8\,\mathrm{GeV}/c$ | EM clus, $E_T > 8\,\mathrm{GeV}$<br>$\not\!\!E_T > 15\,\mathrm{GeV}$ | EM clus, $E_T > 8\,\mathrm{GeV}$<br>$\not\!\!E_T > 15\,\mathrm{GeV}$ | muon stub<br>XFT trk, $p_T > 8\,\mathrm{GeV}/c$ |
| L2 | CEM cluster, $E_T > 16\,\mathrm{GeV}$<br>XFT track, $p_T > 8\,\mathrm{GeV}/c$ | Auto-accept<br>(prescale 50) | CEM clus, $E_T > 20\,\mathrm{GeV}$ | Auto-accept<br>(prescale 50) | Auto-accept |
| L3 | CEM cluster, $E_T > 18\,\mathrm{GeV}$<br>COT track, $p_T > 9\,\mathrm{GeV}/c$ | CEM clus, $E_T > 18\,\mathrm{GeV}$<br>COT trk, $p_T > 9\,\mathrm{GeV}/c$ | EM clus, $E_T > 25\,\mathrm{GeV}$<br>$\not\!\!E_T > 25\,\mathrm{GeV}$ | EM clus, $E_T > 25\,\mathrm{GeV}$<br>$\not\!\!E_T > 25\,\mathrm{GeV}$ | muon stub<br>COT trk, $p_T > 12\,\mathrm{GeV}/c$ |

**Table 15:** *Backup triggers for trigger efficiency measurement.*

The tracking efficiency is measured using the W_NOTRACK trigger. An offline $\mathrm{W} \to e\nu$ selection is applied, which consists of the single tight electron selection of Table 11 and the additional requirement $\not\!\!E_\mathrm{T} > 25\,\mathrm{GeV}$.

As the L1 calorimeter requirement is satisfied in both the trigger and offline cuts, the L1 XFT tracking efficiency L1_XFT8_PT8 is measured as:

$$\epsilon(\textsc{l1\_xft8\_pt8}) = \frac{\#\ \mathrm{W\ candidates\ passing\ \textsc{l1\_cem8\_pt8}}}{\#\ \mathrm{W\ candidates}}. \tag{4.7.1}$$

Owing to the 'spacer' in the centre of the COT mentioned in Section 2.2.2 the tracking efficiency is lower in the centre of the detector. The data are divided into six run-periods corresponding to different trigger conditions and listed in Table 16, and in each period the efficiency is fitted to the form:

$$\epsilon(\text{L1\_XFT8\_PT8}) = A - \frac{C}{2\pi\sigma} \cdot \exp(-\frac{\eta^2}{2\sigma^2}). \tag{4.7.2}$$

A total efficiency is found by convolving these fits with $\eta$ distributions from the simulation (total or binned in rapidity), weighted by the luminosities collected in the different run periods.

The XFT track information is passed through L2 with efficiency $99.99 \pm 0.01\%$.

The L3 tracking efficiency is measured analagously to the L1 efficiency of Eqn 4.7.1 but with the additional requirement that the L1 and L2 trigger bits be set:

$$\epsilon(\text{L3\_PT9}) = \frac{\#\text{ W candidates passing L1\_CEM8\_PT8 \& L2\_CEM16\_PT8 \& L3\_CEM18\_PT9}}{\#\text{ W candidates passing L1\_CEM8\_PT8 \& L2\_CEM16\_PT8}}. \tag{4.7.3}$$

The only dependence found is for $|\eta| > 0.9$ during run periods 1-3, which is fitted as:

$$\epsilon(\text{L3\_PT9}) = (-3.83 \pm 0.12) + (11.24 \pm 0.14) \cdot |\eta| + (-6.53 \pm 0.13) \cdot |\eta|^2 \ . \tag{4.7.4}$$

| Period | Run Range | $\mathcal{L}dt$ / pb$^{-1}$ |
|---|---|---|
| 1 | $\leq$ 147869 | 11.6 |
| 2 | 148153 – 152629 | 18.9 |
| 3 | 152630 – 156487 | 42.2 |
| 4 | 159603 – 163527 | 51.4 |
| 5 | 163955 – 167715 | 53.3 |
| 6 | 167717 – 168889 | 12.6 |
| Total | | 189.9 |
| Total with offline factor 1.9% | | 193.5 |

**Table 16:** *Run periods for trigger efficiency measurement.*

The inclusive muon trigger, which makes no requirement on calorimetery, is used to measure the calorimeter trigger efficiency. The L1 calorimetric trigger efficiency is found to be 100% for electrons with $E_T > 20\,\text{GeV}$.

The L2 calorimeter efficiency is found by comparing events from the L2_CEM16_PT8 trigger and the auto-accept L2_PS50_L1_CEM8_PT8 trigger. The efficiency is fitted to the form:

$$\epsilon(\textsc{l2\_cem16}) = 1 - p_0 \cdot \exp\left(-p_1 \cdot E_T\right) \ . \tag{4.7.5}$$

The L2 calorimeter trigger is found to be consistent with 100% efficiency for $E_T >$ 30 GeV.

The calorimeter component of the L3 trigger is looked at using events passing the ELECTRON_CENTRAL_8 and L2_CEM16_PT8 triggers. The L3 calorimeter trigger is found to be compatible with 100% efficiency for $E_T > 23\,\mathrm{GeV}$, so is taken to be 100% efficient for events selected in these analyses.

The total efficiency for triggering on electron events is:

$$\epsilon_{trig}^{\mathrm{CEN18}} = 0.966 \pm 0.001 \qquad (72\,\mathrm{pb}^{-1}) \ .$$

For the larger dataset the fits are convolved separately for CC and CF central event $E_T$ and $\eta$ distributions, to give:

$$\epsilon_{trig}^{\mathrm{CEN18}} = 0.965 \pm 0.001 \qquad (\mathrm{CC\ events}, 194\,\mathrm{pb}^{-1}) \ ,$$
$$\epsilon_{trig}^{\mathrm{CEN18}} = 0.963 \pm 0.001 \qquad (\mathrm{CF\ events}, 194\,\mathrm{pb}^{-1}) \ .$$

The rapidity dependence of the trigger efficiency is found by convolving the $\eta$- and $E_T$-dependent efficiencies with $\eta$ and $E_T$ distributions found from the simulation for events passing the acceptance cuts in each bin of rapidity. The rapidity dependence for triggering on single electrons is shown in Figure 53, separately for central-central and central-forward events.

### 4.7.2 Forward Electron Trigger Efficiency

The central electron trigger is used for central-central and for central-forward events, however for forward-forward events the Z_NOTRACK trigger is used.

The CENTRAL_ELECTRON_18 and Z_NOTRACK triggers are compared in Table 17. The Z_NOTRACK trigger efficiency is measured from central-forward Z events that have been selected from the ELECTRON_CENTRAL_18 trigger using all central and forward electron identification cuts. The Level-1 8 GeV calorimetry trigger has already been found to be fully efficient, and the central leg of central-forward events satisfies the requirements for

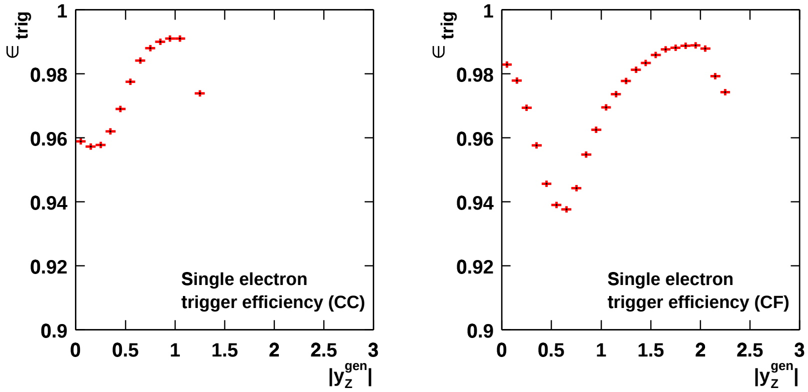

**Figure 53:** *Rapidity dependence of single electron trigger efficiencies, for CC and CF events.*

one leg of the Z_NOTRACK trigger by virtue of having passed the ELECTRON_CENTRAL_18 trigger.

The efficiency of the Z_NOTRACK trigger on a single forward leg is therefore given by the fraction of central-forward events selected from the ELECTRON_CENTRAL_18 trigger, that also passed the Z_NOTRACK trigger. The efficiency for triggering on forward-forward Z events is then the square of this 'single-leg' trigger efficiency.

| | ELECTRON_CENTRAL_18 | Z_NOTRACK |
|---|---|---|
| L1 | CEM cluster, $E_T > 8\,\mathrm{GeV}$<br>XFT track, $p_T > 8\,\mathrm{GeV}/c$ | CEM cluster, $E_T > 8\,\mathrm{GeV}$ |
| L2 | CEM cluster, $E_T > 16\,\mathrm{GeV}$<br>XFT track, $p_T > 8\,\mathrm{GeV}/c$ | Two CEM clusters, $E_T > 16\,\mathrm{GeV}$ |
| L3 | CEM cluster, $E_T > 18\,\mathrm{GeV}$<br>COT track, $p_T > 9\,\mathrm{GeV}/c$ | Two CEM clusters, $E_T > 18\,\mathrm{GeV}$ |

**Table 17:** *Triggers for forward trigger efficiency measurement.*

The trigger efficiency is measured as a function of $E_T$ and convolved with $E_T$ distributions from the simulation to give the efficiency as a function of boson rapidity. Both distributions are shown in Figure 54.

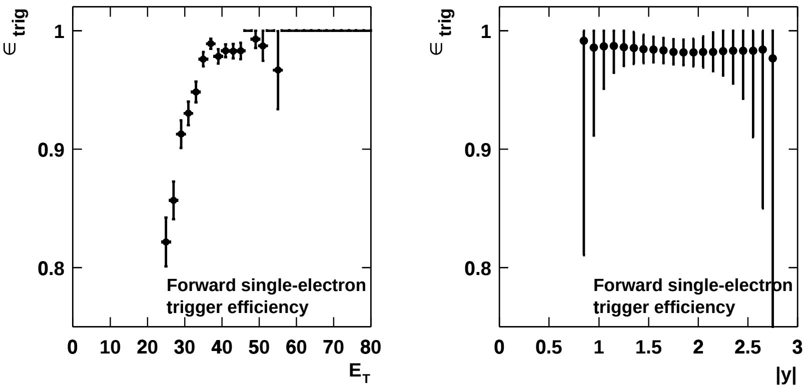

**Figure 54:** *Forward electron trigger efficiency, given for a single electron as a function of [left] electron $\eta$ and [right] boson rapidity. This efficiency must be applied to each of the two legs for an event to pass the* Z_NOTRACK *trigger.*

## 4.8. Total Efficiency

For a measurement using central-central and central-forward events only, the trigger and lepton identification efficiencies enter the total cross-section in the form:

$$\epsilon_{trig} \cdot \epsilon_Z = f_{CC} \cdot \epsilon_{trig}^{CC} \cdot \epsilon_Z^{CC} + f_{CF} \cdot \epsilon_{trig}^{CF} \cdot \epsilon_Z^{CF}, \tag{4.8.1}$$

where $f_{CC}$ and $f_{CF}$ are the fractions of the total number of accepted events that are central-central and central-forward respectively, as measured from the simulation; that is, $f_{CF} = 1 - f_{CC}$.

Equation 4.8.1 may be expressed in terms of experimentally-measured quantities as:

$$\begin{aligned}\epsilon_{trig} \cdot \epsilon_Z = {} & f_{CC} \cdot \epsilon_{trig}^{\text{CEN18}}(2 - \epsilon_{trig}^{\text{CEN18}}) \cdot (2\epsilon_L\epsilon_T - \epsilon_T^2) \cdot \epsilon_{clustering}^2 \cdot \epsilon_{tracking}^2 \\ & + f_{CF} \cdot \epsilon_{trig}^{\text{CEN18}} \cdot \epsilon_T \epsilon_T^{\text{CF correction}} \cdot \epsilon_P \cdot \epsilon_{clustering} \cdot \epsilon_{tracking}\end{aligned} \tag{4.8.2}$$

where each $\epsilon$ has been defined in the previous sections: $\epsilon_{trig}^{\text{CEN18}}$ is the single electron trigger efficiency, $\epsilon_L$, $\epsilon_T$ and $\epsilon_P$ are the loose, tight and forward single electron identification efficiencies respectively, $\epsilon_{clustering}$ is the central clustering efficiency, and $\epsilon_{tracking}$ is the central tracking efficiency.

$\epsilon_L$ and $\epsilon_T$ are not independent but the total uncertainty on the combined trigger and lepton identification efficiency may be found by differentiating Equation 4.8.2 with respect to the independent variables $A_1$, $A_2$ and $A_3$ defined in Section 4.5.1 , $\epsilon_P$, $\epsilon_T^{\text{CF correction}}$, $\epsilon_{trig}^{\text{CEN18}}$, $\epsilon_{clustering}$, $\epsilon_{tracking}$ and $f_{CC}$.

The total efficiency is found to be:

$$\epsilon_{trig} \cdot \epsilon_Z = 0.750 \pm 0.011 \ (72\text{pb}^{-1}) \ ,$$

$$\epsilon_{trig} \cdot \epsilon_Z = 0.760 \pm 0.006 \ (194\text{pb}^{-1}) \ .$$

The principal contribution to the total efficiency uncertainty comes from the electron identification efficiency uncertainties, and as this has a statistical component, the total efficiency uncertainty is significantly smaller for the 194 $\text{pb}^{-1}$ dataset than for the 72 $\text{pb}^{-1}$ dataset.

Putting together the rapidity dependences of the identification and triggering efficiencies and adding the tracking and clustering efficiencies gives the total rapidity-dependent efficiency shown for central-central and central-forward events in Figure 55. Finally the rapidity-dependent efficiency is shown for CC+CF events combined in Figure 56. Here, correlated uncertainties between the two classes of event are taken into account and the fraction of events in each bin that come from CC and CF events is taken from PYTHIA and CTEQ5L. From this plot only the uncertainties in each bin are used in the determination of $\frac{d\sigma}{dy}$ – to obtain the total cross-section in each bin, efficiencies for each category of event are applied directly to the number of candidates for each category of event to avoid model dependence in the measurement.

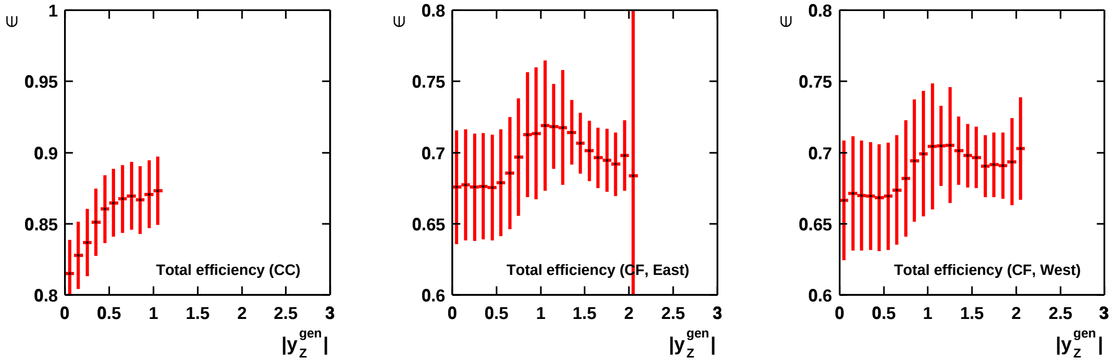

**Figure 55:** *Rapidity dependence of total efficiency.*

The expression analagous to Equation 4.8.1 for forward-forward events is:

$$(\epsilon_{trig} \cdot \epsilon_Z)^{(\text{FF})} = \epsilon_{\text{trig}}^{\text{Z\_NOTRK}} \cdot \epsilon_F^2 \cdot \epsilon_{\text{fwd tracking}}(2 - \epsilon_{\text{fwd tracking}}).$$

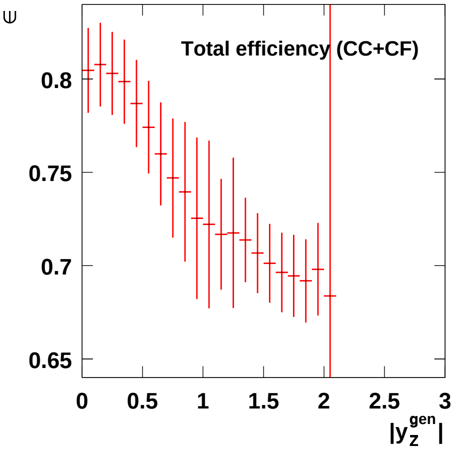

**Figure 56:** *Rapidity dependence of total efficiency for CC+CF events, taking the fraction of each class of event from simulation and computing correlated uncertainties. Only used for total uncertainty.*

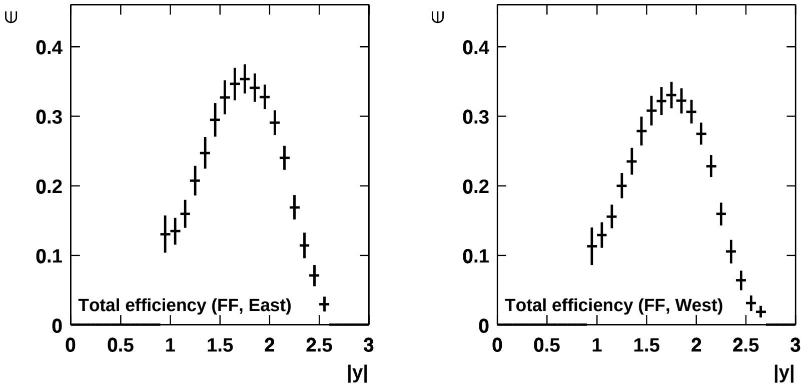

**Figure 57:** *Rapidity dependence of total efficiency for forward-forward events.*

This total efficiency is shown as a function of boson rapidity in Figure 57.

A total efficiency for CC, CF and FF events may be obtained by combining the above results, and again taking into account correlated uncertainties among the three classes of event. This is shown in Figure 58. As for Figure 56 the fractions of events in each bin that come from CC, CF and FF events are taken from Pythia and cteq5l, and from this plot only the uncertainties in each bin are used in the determination of $\frac{d\sigma}{dy}$.

## 4.9. Efficiency for $\mathrm{W} \rightarrow e\nu$ Selection

The efficiency for $\mathrm{W} \rightarrow e\nu$ selection is given simply by the efficiency for finding a tight

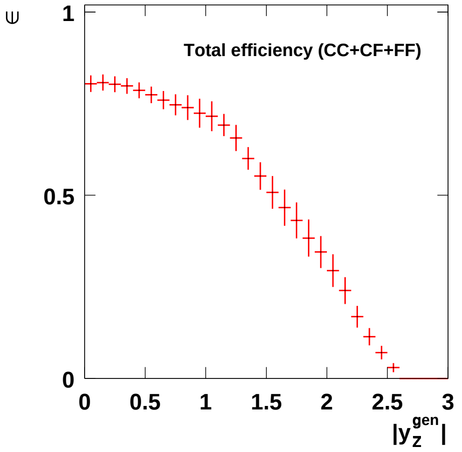

**Figure 58:** *Rapidity dependence of total efficiency for CC+CF+FF events, taking the fraction of each class of event from simulation and computing correlated uncertainties. Only used for total uncertainty.*

electron in the central region, $\epsilon_T \cdot \epsilon_{clustering} \cdot \epsilon_{tracking} \cdot \epsilon_{trig}^{\mathrm{CEN18}}$.

## 4.10. Ratio of W and Z efficiencies

In taking the ratio of W and Z cross-sections the terms from the efficiency of selecting W events cancel completely with terms in the Z selection, so the resulting efficiency expression that enters the ratio is:

$$\frac{\epsilon_{trig} \cdot \epsilon_{\mathrm{Z}}}{\epsilon_{trig} \cdot \epsilon_{\mathrm{W}}} = f_{CC} \cdot (2 - \epsilon_{trig}^{\mathrm{CEN18}}) \cdot (2\epsilon_L - \epsilon_T) \cdot \epsilon_{clustering} \cdot \epsilon_{tracking} + f_{CF} \cdot \epsilon_T^{\mathrm{CF\ correction}} \cdot \epsilon_P, \tag{4.10.1}$$

which for the $72\,\mathrm{pb}^{-1}$ dataset has value $0.952 \pm 0.011$ where the uncertainty is dominated by the electron identification efficiencies.

# Chapter 5

# Results

In this chapter, all of the results obtained in the preceding sections are put together in the physics measurements, which are then interpreted and their significance discussed.

The total cross-section and the ratio of W and Z boson cross-sections are measured using central-central and central-forward events, and $d\sigma/dy$ is measured both with these events and with the addition of forward-forward events. Owing to the large uncertainties associated with the forward-forward events, the total cross-section is measured from them only as a cross-check.

## 5.1. Z Cross-section

The expression given for the Z cross-section in Eqn 1.2.3 is repeated here:

$$\sigma_{\mathrm{Z}/\gamma^*} \cdot Br(\mathrm{Z} \rightarrow \mathrm{e}^+\mathrm{e}^-) = \frac{N_{\mathrm{Z}}^{\mathrm{candidates}} - N^{\mathrm{background}}}{A_{\mathrm{Z}} \cdot \epsilon_{\mathrm{Z}} \cdot \epsilon_{trig} \cdot \epsilon_{zvertex} \cdot \int \mathcal{L}dt} \quad . \tag{5.1.1}$$

The acceptance $A_Z$ and the luminosity correction $\epsilon_{zvertex}$ were discussed in Chapter 3; and the reconstruction and identification efficiencies $\epsilon_Z$ and trigger efficiency $\epsilon_{trig}$ discussed in Chapter 4. The luminosity measurement was discussed in Section 2.5.

The invariant mass distribution of the candidates in the $72\,\mathrm{pb}^{-1}$ dataset is compared to the simulation in Figure 59. All the values entering the cross-section are summarised in Tables 18 and 19 for the two samples comprising $72\,\mathrm{pb}^{-1}$ and $194\,\mathrm{pb}^{-1}$ respectively. In addition the result is multiplied by a term to remove the contribution from $\gamma^*$ exchange; this is discussed in Section 5.1.1.

| | CC | CF | CC+CF |
|---|---|---|---|
| $N_Z^{candidates}$ | $1730 \pm 42\,(\mathrm{stat})$ | $2512 \pm 50\,(\mathrm{stat})$ | $4242 \pm 65\,(\mathrm{stat})$ |
| $N^{background}$ | $4.5 \pm 7.1$ | $57 \pm 17$ | $62 \pm 18$ |
| $A_Z$ | $0.1099 \pm 0.0027\,(\mathrm{sys})$ | $0.2083 \pm 0.0023\,(\mathrm{sys})$ | $0.3182 \pm 0.0041$ |
| $\epsilon_Z \cdot \epsilon_{trig}$ | $0.853 \pm 0.013\,(\mathrm{sys})$ | $0.696 \pm 0.014\,(\mathrm{sys})$ | $0.750 \pm 0.011\,(\mathrm{sys})$ |
| $\epsilon_{zvertex}$ | $0.950 \pm 0.004(\mathrm{sys})$ | | |
| $\int \mathcal{L}dt\,/\mathrm{pb}^{-1}$ | $72 \pm 4.3(\mathrm{lum})$ | | |
| $\frac{I_2}{I_1}$ | $1.004 \pm 0.001(\mathrm{sys})$ | | |

**Table 18:** *Summary of values for the cross-section calculation, 72 pb*$^{-1}$.

| | CC | CF | CC+CF |
|---|---|---|---|
| $N_Z^{candidates}$ | $4449 \pm 67\,(\mathrm{stat})$ | $7011 \pm 84\,(\mathrm{stat})$ | $10460 \pm 102\,(\mathrm{stat})$ |
| $N^{background}$ | $11 \pm 5$ | $145 \pm 50$ | $156 \pm 54$ |
| $A_Z$ | $0.1099 \pm 0.0027\,(\mathrm{sys})$ | $0.2083 \pm 0.0023\,(\mathrm{sys})$ | $0.3182 \pm 0.0041$ |
| $\epsilon_Z \cdot \epsilon_{trig}$ | $0.864 \pm 0.010\,(\mathrm{sys})$ | $0.705 \pm 0.006\,(\mathrm{sys})$ | $0.760 \pm 0.006\,(\mathrm{sys})$ |
| $\epsilon_{zvertex}$ | $0.948 \pm 0.004(\mathrm{sys})$ | | |
| $\int \mathcal{L}dt\,/\mathrm{pb}^{-1}$ | $193.5 \pm 11.6(\mathrm{lum})$ | | |
| $\frac{I_2}{I_1}$ | $1.004 \pm 0.001(\mathrm{sys})$ | | |

**Table 19:** *Summary of values for the cross-section calculation, 194 pb*$^{-1}$.

### 5.1.1 Removing Drell-Yan Contributions from $\gamma^*$ Exchange

A correction needs to be applied to the number of candidates to account for the fact that some of the $\mathrm{e}^+\mathrm{e}^-$ pairs in the selected invariant mass window come from the continuum $p\overline{p} \rightarrow \gamma^* \rightarrow e^+e^-$ or the interference term between $\gamma^*$ and $Z^0$, and not from $\mathrm{Z}^0$ resonant production. The correction factor is obtained from the ratios of the integrals

$$I_1 \equiv \int_{66}^{116} |\mathrm{Z}^0 + \gamma|^2 dM \quad \text{and} \quad I_2 \equiv \int_{0}^{\infty} |\mathrm{Z}^0|^2 dM$$

at $\sqrt{s}$=1.96 TeV. The most recent theoretical calculation at NNLO [40] gives:

$$\frac{I_2}{I_1} = 1.004 \pm 0.001 \ \ .$$

As a cross-check the ratio of integrals is evaluated using the Pythia generator, which gives $\frac{I_2}{I_1} = 1.003 \pm 0.002$, where the error is statistical.

Finally we have

$$\sigma_{\mathrm{Z}} \cdot Br(\mathrm{Z} \rightarrow \mathrm{e}^{+}\mathrm{e}^{-}) = \frac{I_2}{I_1} \cdot \frac{N_{\mathrm{Z}}^{\mathrm{candidates}} - N^{\mathrm{background}}}{A_{\mathrm{Z}} \cdot \epsilon_{\mathrm{Z}} \cdot \epsilon_{trig} \cdot \epsilon_{zvertex} \cdot \int \mathcal{L}dt}. \tag{5.1.2}$$

### 5.1.2 Results

The resulting measurement of $\sigma_{\mathrm{Z}} \cdot Br(\mathrm{Z} \rightarrow \mathrm{e}^{+}\mathrm{e}^{-})$ is:

$$(255.7 \pm 2.4_{\mathrm{stat}} \pm 5.2_{\mathrm{sys}} \pm 15.2_{\mathrm{lum}})\,\mathrm{pb} \qquad (194\,\mathrm{pb}^{-1}) \ \ .$$

This is in good agreement with the NNLO calculation provided by Stirling, which gives $253 \pm 9$ pb [41]. Cross-checking in the CC and CF topologies separately and making the measurement only in the smaller, 72 pb$^{-1}$ dataset gives:

$$(255.7 \pm 3.8_{\mathrm{stat}} \pm 8.1_{\mathrm{sys}} \pm 15.3_{\mathrm{lum}})\,\mathrm{pb} \qquad (194\,\mathrm{pb}^{-1},\ \mathrm{CC\ only}) \ \ ,$$

$$(255.7 \pm 3.1_{\mathrm{stat}} \pm 5.1_{\mathrm{sys}} \pm 15.3_{\mathrm{lum}})\,\mathrm{pb} \qquad (194\,\mathrm{pb}^{-1},\ \mathrm{CF\ only}) \ \ ,$$

$$(255.8 \pm 3.9_{\mathrm{stat}} \pm 5.3_{\mathrm{sys}} \pm 15.3_{\mathrm{lum}})\,\mathrm{pb} \qquad (72\,\mathrm{pb}^{-1},\ \mathrm{Winter\ 2004}) \ .$$

These are all in excellent agreement and should be compared in precision to the earlier CDF measurement of

$$(267.0 \pm 6.3_{\mathrm{stat}} \pm 15.2_{\mathrm{sys}} \pm 16.0_{\mathrm{lum}})\,\mathrm{pb} \qquad (72\,\mathrm{pb}^{-1},\ \mathrm{Summer\ 2003}) \ \ [42]\ .$$

The 35% improvement in the statistical uncertainty of the 72 pb$^{-1}$ measurement comes from the work described in this thesis of understanding the forward detectors and bringing central-forward events in to the analysis. The 65% improvement in the systematic uncertainty comes from the improvements in the systematic analysis carried out on the central-central events and described in this thesis, as well as the inclusion of the central-forward events, which dilutes some of the larger systematic effects on the central-central measurement.

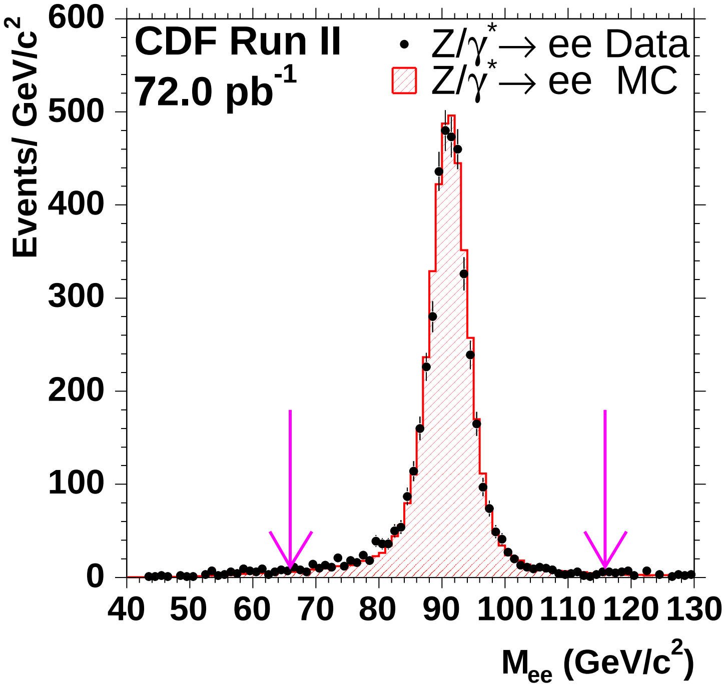

**Figure 59:** *$M_{ee}$ for the final event selection, shown for the $72\,pb^{-1}$ dataset.*

### 5.1.3 Combination with $\mu$ channel

CDF has also measured the Z cross-section in the muon channel using $72\,\text{pb}^{-1}$, analagously to the electron measurement presented here. The muon system coverage is smaller than the electron coverage, and an extra background in the muon channels that requires detailed understanding is that from cosmic rays.

The muon channel measurement is as follows [25]:

$$(248.0 \pm 5.9_{\text{stat}} \pm 8.0_{\text{sys}} \pm 14.9_{\text{lum}})\,\text{pb} \qquad (72\,\text{pb}^{-1}, \mu\ \text{channel}).$$

The cross-section is not yet measured in the muon channel with the larger dataset.

The electron and muon channel measurements are compatible and have been combined [48]. The following components were taken to be completely correlated between the electron and muon channels: the boson $p_T$ model, the PDF uncertainty, the $p_T$ scale and resolution and the recoil energy model, all used in the acceptance measurement; the vertex $z_0$ cut and the track reconstruction used in the efficiency measurement; and the hadronic background determination.

The combined cross-section measurement is as follows:

$$(253.9 \pm 3.3_{\text{stat}} \pm 4.6_{\text{sys}} \pm 15.2_{\text{lum}})\,\text{pb} \qquad (72\,\text{pb}^{-1}, \text{e} + \mu \text{ channels}).$$

The cross-section measurement is shown alongside previous measurements in Figure 60. Also shown is the W boson cross-section, which is discussed in the following section.

## 5.2. Ratio

The ratio of W and Z boson cross-sections is of interest as its measurement may be designed such that the large luminosity uncertainty common to all cross-section measurements at the Tevatron, cancels. It may be used to test the Standard Model, and further physical quantities of interest may be extracted from it.

The ratio of W and Z boson cross-sections times branching ratios is evaluated as:

$$R = \frac{1}{I_2/I_1} \cdot \frac{N_{\text{W}}^{\text{cand}} - N_{\text{W}}^{\text{bck}}}{N_{\text{Z}}^{\text{cand}} - N_{\text{Z}}^{\text{bck}}} \cdot \frac{A_{\text{Z}}}{A_{\text{W}}} \cdot \frac{\epsilon_{trig} \cdot \epsilon_{\text{Z}}}{\epsilon_{trig} \cdot \epsilon_{\text{W}}}. \tag{5.2.1}$$

The ratio of W and Z boson acceptances is discussed in Section 3.5, and the ratio of trigger and selection efficiencies $\frac{\epsilon_{trig} \cdot \epsilon_{\text{Z}}}{\epsilon_{trig} \cdot \epsilon_{\text{W}}}$ discussed in Section 4.10. The numbers are summarised in Table 20 and give the result:

$$R = 10.82 \pm 0.18_{\text{stat}} \pm 0.16_{\text{sys}} \; (72\,\text{pb}^{-1}, \text{ electron channel}). \tag{5.2.2}$$

| | |
|---|---|
| $N_{\text{W}}^{\text{cand}}$ | 37584 |
| $N_{\text{W}}^{\text{bck}}$ | 1656 ± 300 |
| $N_{\text{Z}}^{\text{cand}}$ | 4242 |
| $N_{\text{Z}}^{\text{bck}}$ | 62 ± 18 |
| $\frac{A_{\text{Z}}}{A_{\text{W}}}$ | 1.3273 ± 0.0109 |
| $\frac{\epsilon_{trig} \cdot \epsilon_{\text{Z}}}{\epsilon_{trig} \cdot \epsilon_{\text{W}}}$ | 0.952 ± 0.011 |
| $\frac{I_2}{I_1}$ | 1.004 ± 0.001 |

**Table 20:** *Summary of values for ratio calculation in the electron channel.*

### 5.2.1 Combination with $\mu$ channel

The W cross-section and ratio of the W and Z cross-sections have also been measured in the muon channel.

The ratio measurement is as follows [25]:

$$R = 11.12 \pm 0.27_{\text{stat}} \pm 0.18_{\text{sys}} \ (72\,\text{pb}^{-1},\ \text{muon channel}). \tag{5.2.3}$$

A combination has been made [48] in which in addition to the correlations discussed for the Z cross-section combination above, the Z and $W \to \tau\nu$ backgrounds to the W measurements are taken to be fully correlated between the electron and muon channels.

The combined W cross-section is shown alongside previous measurements and the Z cross-section in Figure 60.

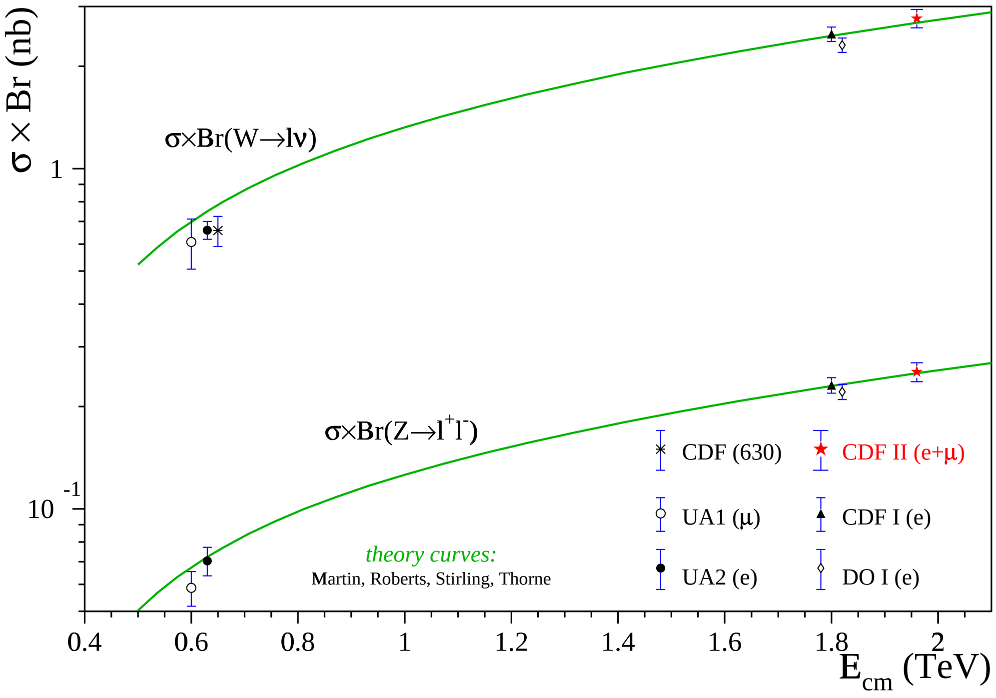

**Figure 60:** *$W \to \ell\nu$ and $Z \to \ell\ell$ cross-sections as a function of* $p\bar{p}$ *centre-of-mass energy ($\ell = e/\mu$). 'CDF II' indicates the results from this thesis. The curves show NNLO calculations.*

The combined ratio measurement is as follows:

$$R = 10.92 \pm 0.15_{\text{stat}} \pm 0.14_{\text{sys}} \ (72\,\text{pb}^{-1}, e + \mu \text{ channels}), \tag{5.2.4}$$

which may be compared with measurements from previous collider experiments shown in Table 21.

| Experiment | mode | R |
|---|---|---|
| UA1 [43] | e+$\mu$ | $9.5^{+1.1}_{-1.0}$ |
| UA2 [44] | e | $9.38 \pm 0.86$ |
| CDF Run I [45] | e | $10.94 \pm 0.45$ |
| D0 Run Ia [46] | e+$\mu$ | $10.9 \pm 0.49$ |
| D0 Run Ib [47] | e | $10.43 \pm 0.27$ |

**Table 21:** *Measurements of R from previous collider experiments.*

### 5.2.2 Extraction of $Br(\mathrm{W} \to \ell\nu)$

Whereas the branching ratio of Z to leptons is well-measured from LEP, the W branching ratio is not so well-known and may be extracted from the measured cross-section ratio.

As given in Eqn. 1.2.4 the ratio measured here may be expressed:

$$R = \frac{\sigma_{\mathrm{W}} \cdot Br(\mathrm{W} \to \ell\nu)}{\sigma_{\mathrm{Z}} \cdot Br(\mathrm{Z} \to \ell\ell)}. \tag{5.2.5}$$

The ratio of total cross-sections $\frac{\sigma_{\mathrm{Z}}}{\sigma_{\mathrm{W}}}$ is calculable in the Standard Model, so the W branching ratio may be expressed:

$$Br(\mathrm{W} \to \ell\nu) = \frac{1}{I_2/I_1} \cdot \frac{N_{\mathrm{W}}^{\mathrm{cand}} - N_{\mathrm{W}}^{\mathrm{bck}}}{N_{\mathrm{Z}}^{\mathrm{cand}} - N_{\mathrm{Z}}^{\mathrm{bck}}} \cdot \frac{\epsilon_{trig} \cdot \epsilon_{\mathrm{Z}}}{\epsilon_{trig} \cdot \epsilon_{\mathrm{W}}} \cdot \left(\frac{A_{\mathrm{Z}}\sigma_{\mathrm{Z}}}{A_{\mathrm{W}}\sigma_{\mathrm{W}}}\right) \cdot Br(\mathrm{Z} \to \ell\ell). \tag{5.2.6}$$

$A_{\mathrm{Z}}\sigma_{\mathrm{Z}}$ and $A_{\mathrm{W}}\sigma_{\mathrm{W}}$ have PDF uncertainties that may be studied in the same way as $A_{\mathrm{Z}}$ and $\sigma_{\mathrm{Z}}$. As suggested by Figures 23 and 24 the uncertainty on $A\sigma$ is found to be slightly larger than on $A$ alone [48].

The 2002 PDG value for $Br(\mathrm{Z} \to \ell\ell)$ is $0.033658 \pm 0.000023$ [51]. The ratio of total cross-sections is calculated at NNLO to be 3.3696 with 0.56% PDF uncertainty and 0.43% uncertainty from electroweak parameters. This results in a measurement [48]:

$$Br(\mathrm{W} \to \ell\nu) = 0.1089 \pm 0.0022 \quad (\ell = \mathrm{e}, \mu). \tag{5.2.7}$$

The measurement is in good agreement with both the Standard Model value $0.1081 \pm 0.0002$, and the current world average $0.1068 \pm 0.0012$ (for $\ell =$e, $\mu, \tau$) [51]. However it is interesting to note that the most recent results from the LEP Electroweak Working Group – not included in the current world average – give a $\tau$ measurement that is around $3\sigma$ from the e and $\mu$ measurements: $Br(\mathrm{W} \to \mathrm{e}\nu) = 0.1066 \pm 0.0017$, $Br(\mathrm{W} \to \mu\nu) = 0.1060 \pm 0.0015$ and $Br(\mathrm{W} \to \tau\nu) = 0.1141 \pm 0.0022$ [49].

### 5.2.3 Extraction of $\Gamma(\mathrm{W})$

The value obtained for $Br(\mathrm{W} \rightarrow \ell\nu)$ may be used with a measured value of $\Gamma(\mathrm{W} \rightarrow \ell\nu)$ to extract a value for the total width of the W, $\Gamma(\mathrm{W})$. The 2002 PDG value for $\Gamma(\mathrm{W} \rightarrow \ell\nu)$ is $226.4 \pm 0.4\,\mathrm{MeV}$ [51], giving the indirect measurement:

$$\Gamma(\mathrm{W}) = 2078.8 \pm 41.4\,\mathrm{MeV}. \tag{5.2.8}$$

This is in good agreement with the Standard Model prediction $2092.1 \pm 2.5\,\mathrm{MeV}$, and the world average $2118 \pm 42\,\mathrm{MeV}$ (direct and indirect measurements) [51].

### 5.2.4 Extraction of $V_{cs}$

The total width of the W is a sum of partial widths for leptons and quarks [51]:

$$\Gamma_{\mathrm{W}} \simeq 3\,\Gamma^0_{\mathrm{W}} + 3\left\{1 + \frac{\alpha_s(M_{\mathrm{W}})}{\pi} + 1.409\left(\frac{\alpha_s(M_{\mathrm{W}})}{\pi}\right)^2 - 12.77\left(\frac{\alpha_s(M_{\mathrm{W}})}{\pi}\right)^3\right\} \sum_{u,d,c,s,b} |V_{qq'}|^2 \Gamma^0_{\mathrm{W}}\ , \tag{5.2.9}$$

where $V_{qq'}$ are elements of $V_{CKM}$ defined in Equation 1.1.7. The top quark is kinematically excluded from the summation.

The measured value of $\Gamma_{\mathrm{W}}$ may therefore be used to constrain the term that is measured the least well, which is $V_{cs}$. Using $\alpha_s(M_W) = 0.120$, $\Gamma^0_{\mathrm{W}} = \Gamma(\mathrm{W} \rightarrow \ell\nu) = 226.4\,\mathrm{MeV}$ and CKM matrix element elements from the Particle Data Group [51] this gives:

$$|V_{cs}| = 0.967 \pm 0.030\ . \tag{5.2.10}$$

For comparison the most recent LEP EWWG preliminary measurement is $|V_{cs}| = 0.976 \pm 0.014$ [49] and the combined LEP and Tevatron Run I measurement is $|V_{cs}| = 0.998 \pm 0.013$ [50].

## 5.3. $d\sigma/dy$

In each bin of reconstructed boson rapidity the differential cross-section is evaluated in a similar way to the total cross-section.

The rapidity-dependence of the $\mathrm{Z}/\gamma^*$ correction $\frac{I_2}{I_1}$ is checked explicitly by generating two million $\mathrm{Z} \rightarrow \mathrm{ee}$ and two million $\mathrm{Z}/\gamma^* \rightarrow \mathrm{ee}$ events using Pythia, and taking the ratio of events in bins of boson rapidity, applying the invariant mass window $66 < M^{gen}_{\mathrm{Z}/\gamma^*} <$

116 GeV/$c^2$ to the $Z/\gamma^*$ sample. Figure 61 shows the ratio, where the first bin has been fixed at 1.004 to match the total ratio $\frac{I_2}{I_1}$. As expected, no evidence of any rapidity dependence is found, and $\frac{I_2}{I_1}$ is taken to be constant for all rapidities.

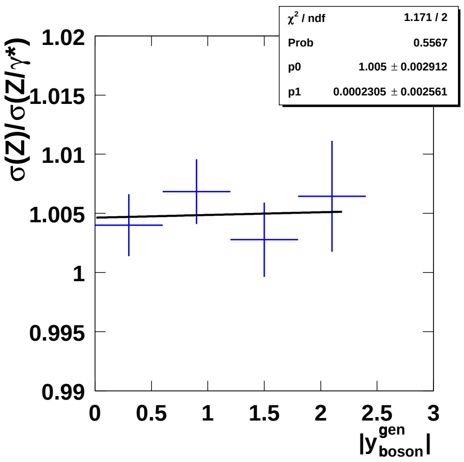

**Figure 61:** *Rapidity dependence of* $\gamma^*$ *correction. Fit shown is to a first-degree polynomial* $p0{+}p1{\cdot}x$.

In order to avoid any assumptions about the fractions of CC and CF events in each bin when combining uncertainties, the numbers of candidate and background events and the efficiency are treated separately for CC, CF(East) and CF(West) in the following way:

$$[\sigma_{\mathrm{Z}} \cdot Br(\mathrm{Z}\to \mathrm{ee})]_{(\text{bin } i)} = \frac{I_2}{I_1}\cdot \frac{\sum_{CC,CF(E),CF(W)} \left(\frac{N_{\mathrm{Z}}^{\text{cand}}-N^{\text{bck}}}{\epsilon_{\mathrm{Z}}\cdot\epsilon^{e}_{trig}}\right)_{(\text{bin } i)}}{A_{\mathrm{Z};\,(\text{bin } i)}\cdot \epsilon_{zvertex}\cdot\int\mathcal{L}dt} \quad . \tag{5.3.1}$$

The number of candidate events in each class is shown for the 194 pb$^{-1}$ dataset in Figure 62.

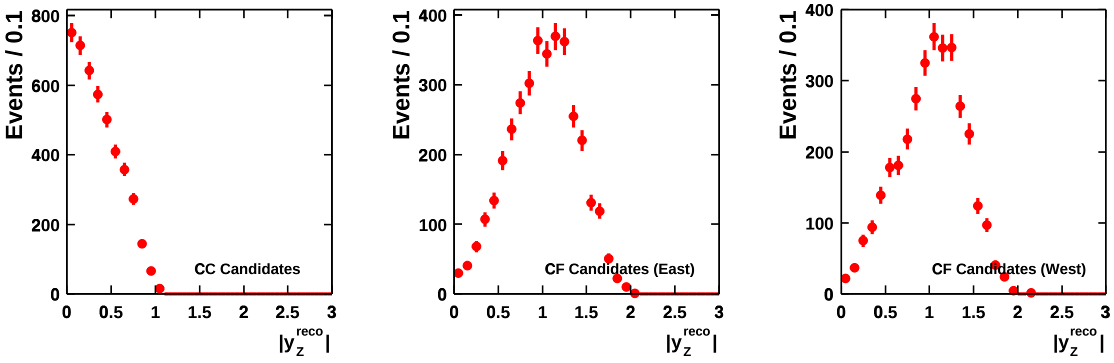

**Figure 62:** *Rapidity dependence of candidate events.*

As a cross-check the total cross-section is determined by integrating the $d\sigma/dy$ measurement. This has a large statistical uncertainty, but is largely independent of PDF uncertainty, which is the main contribution to the systematic uncertainty on the direct cross-section calculation. A correction must be made as the $d\sigma/dy$ measurement presented here does not cover the full kinematic range, and that correction does have a small PDF set dependence.

The total cross-section that comes from integrating $d\sigma/dy$ is:

$$(238.0 \pm 31.3_{\rm stat} \pm 14.3_{\rm lum})\,{\rm pb} \qquad (0 < |y| < 2.1) \ \ ,$$

which on correcting for the range of $y$ sampled gives:

$$(251 \pm 33_{\rm stat} \pm 15.1_{\rm lum})\,{\rm pb} \ \ .$$

Noting that there is only a single event in the final bin, the integral is also calculated omitting the final bin, giving:

$$(236.5 \pm 27.4_{\rm stat} \pm 14.2_{\rm lum})\,{\rm pb} \qquad (0 < |y| < 2.0) \ \ ,$$

which on correcting for the range of $y$ sampled gives:

$$(256 \pm 30_{\rm stat} \pm 15.4_{\rm lum})\,{\rm pb} \ \ ,$$

in good agreement with the cross-section previously measured.

In order to make a comparison with theoretical calculations, a correction is applied to the cross-section so that the quoted result is the cross-section value at the centre of each bin, rather than averaged across the bin. This correction is shown in Figure 63 and it may be seen to reach $\sim 1\%$ at the highest values of $y$ probed by the CC+CF events.

The effect of bin migration is studied in the simulation by comparing the generated and reconstructed rapidities of the Z. It is found that events do not migrate by more than one bin, and that the net migration is $< 0.5\%$, which is much smaller than the statistical uncertainty in the bins. In the highest three or four bins of rapidity the net migration is larger (a few percent) but the statistical uncertainty is also large in these bins. Bin migration is therefore ignored.

The measured $d\sigma/dy$ is given in Table 22.

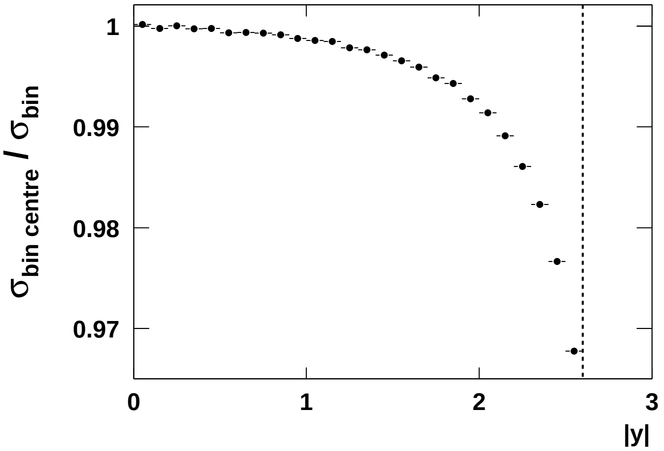

**Figure 63:** *Bin centring correction.*

| $\lvert y\rvert$ | $d\sigma/d\lvert y\rvert$ / pb | stat.$\oplus$ sys. / pb | stat. only /pb |
|---|---|---|---|
| 0.05 | 148.3 | 7.4 | 5.2 |
| 0.15 | 146.9 | 7.3 | 5.2 |
| 0.25 | 144.7 | 7.1 | 5.2 |
| 0.35 | 142.4 | 7.0 | 5.1 |
| 0.45 | 140.7 | 7.0 | 5.1 |
| 0.55 | 141.6 | 7.2 | 5.1 |
| 0.65 | 139.7 | 7.5 | 5.0 |
| 0.75 | 139.1 | 8.1 | 5.0 |
| 0.85 | 127.9 | 8.3 | 4.8 |
| 0.95 | 130.8 | 9.3 | 4.8 |
| 1.05 | 120.9 | 8.9 | 4.5 |
| 1.15 | 119.4 | 6.9 | 4.5 |
| 1.25 | 129.6 | 9.1 | 4.9 |
| 1.35 | 110.2 | 6.5 | 4.8 |
| 1.45 | 116.2 | 7.2 | 5.5 |
| 1.55 | 85.8 | 6.5 | 5.4 |
| 1.65 | 102.6 | 8.5 | 7.0 |
| 1.75 | 65.5 | 7.6 | 6.8 |
| 1.85 | 62.1 | 9.9 | 9.2 |
| 1.95 | 50.5 | 13.8 | 13.1 |
| 2.05 | 15.2 | 15.9 | 15.2 |

**Table 22:** *$d\sigma/dy$ (CC+CF events), with bin-centring corrections applied. A common 6% luminosity uncertainty is not shown.*

Figures 64 to 71 show the measured $d\sigma/dy$, with different comparisons to NLO [28] and NNLO [27] calculations. The errors shown are statistical and statistical $\oplus$ systematic; a common luminosity uncertainty of 6% is not included.

Figure 64 shows a comparison with NLO and NNLO calculations using the MRST2004 NLO and NNLO PDF sets, respectively. As has been mentioned previously, in $\sqrt{s} = 1.96\,\mathrm{TeV}$ $\mathrm{p\overline{p}}$ collisions the Drell-Yan cross-section is enhanced by NNLO corrections, as seen in the figure, and the data are in better agreement with the NNLO calculation than the NLO calculation. The NLO calculation is made for Z exchange only, over the complete mass range. The NNLO calculation is made for $\mathrm{Z}/\gamma^*$ exchange in the mass window of the analysis, so the same factor $\frac{I_2}{I_1}$ is applied to it as to the data.

Figure 65 shows a comparison with NLO calculation and the effect of varying the renormalisation scale $\mu_F$ and factorisation scale $\mu_R$ of the calculation such that $\mu_F = \mu_R = \mu$ and $M_Z/2 < \mu < M_Z$. This band is an estimate of the uncertainty on the theoretical calculation. The corresponding band for the NNLO calculation is much narrower.

Figure 66 shows a comparison with NLO calculations using a range of PDF sets, from the more recent CTEQ6M and MRST2004 back to MRS96. The theoretical calculations are plotted as returned by the program, with no normalisation to the experimental result. MRS96 is included because it dates from before the CDF Run I W charge asymmetry measurement, which was an important new constraint on the PDFs in the regions relevant to the Tevatron. MRST 2004 is dubbed the ‘physical gluon’ PDF set and gives a better description of the Tevatron inclusive jet data than previous sets. MRST 2003c is dubbed the ‘conservative’ PDF set as it is constructed only from a subset of the DIS data for which the evolution in $Q^2$ is known to be valid. $\chi^2$ is formed between the data and the cross-section calculated using each PDF set, defined as

$$\chi^2 = \sum_{\text{populated bins}} \left( \frac{N_{\text{observed}} - N_{\text{expected}}}{\sigma_{\text{observed}}} \right)^2 . \tag{5.3.2}$$

The uncertainty, $\sigma_{\text{observed}}$, is statistical plus systematic (no luminosity) and is taken to be uncorrelated bin-to-bin, since the correlated part is small compared to the uncorrelated part. The theoretical uncertainty on the calculation, such as the renormalisation and factorisation scale shown in Figure 65, is not included in the $\chi^2$. The result is divided by the number of bins and shown in Table 23. It is seen that MRS96 gives the least-good match to the data, but that CTEQ5 seems to fit better than CTEQ6. The best $\chi^2$/dof is 1.3 for the CTEQ5M PDF set, which has probability 16%. However inclusion of the luminosity uncertainty improves the agreement for all PDF sets.

Figure 67 is similar to Figure 66, except that the calculation using each PDF set has been normalised to the data in the region $|y| < 0.5$. This has two motivations: first to take account of the possible overall shift in normalisation arising from the common luminosity uncertainty of 6%, and secondly to take account of the 'K-factor' between NLO and NNLO calculations. Changing the normalisation in this way is in attempt to see differences in shape in the region where the slope of the distribution is changing. Again $\chi^2$ are formed between the data and the calculation using each PDF set, and is shown in Table 24. To take account of the normalisation the number of degrees of freedom is reduced by one. No PDF set is particularly favoured, and MRS96 is not disfavoured as it was in the above case when no normalisation was applied. The best $\chi^2$/dof is 1.0 for the CTEQ5M PDF set, which has probability 45%.

The CTEQ6 error PDF sets have already been used in the determination of the PDF uncertainty on the total cross-section. Figure 68 shows the spread of $d\sigma/dy$ calculated at NLO using each of the error PDF sets from CTEQ6, in order to compare to the spread from the different generations of MRST and CTEQ PDF sets shown above. In Figure 69 each of the error PDF calculations has been scaled using a scale factor determined from the central PDF set in the region $|y| < 0.5$, and in Figure 70, each error PDF calculation has been normalised in the region $|y| < 0.5$.

Finally Figure 71 shows a coarser binning, to try to see whether the steeper fall seen in the data compared to the calculation is significant, but this is inconclusive.

It can be seen that the measurement of $d\sigma/dy$ using central-central and central-forward events does not favour one PDF set over another, by eye or from computing $\chi^2$, and in particular it is not sensitive enough to make an immediate constraint on the CTEQ6 error PDF sets.

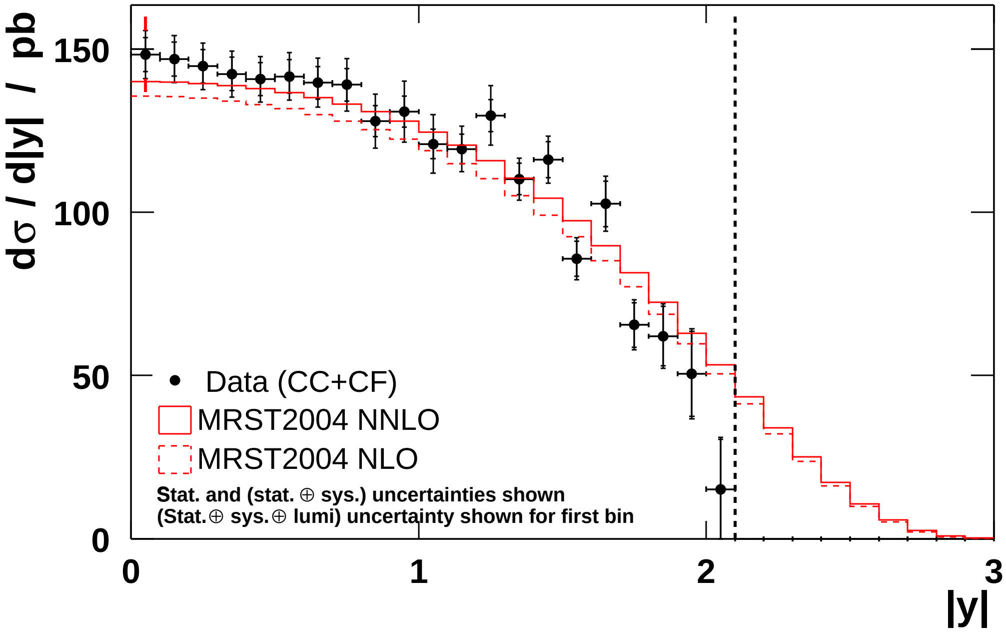

**Figure 64:** *$d\sigma/dy$, compared to NNLO and NLO calculations made with* MRST *PDF sets (no normalisation). The vertical dashed line gives the acceptance limit and a common 6% luminosity uncertainty is not shown except in the first bin.*

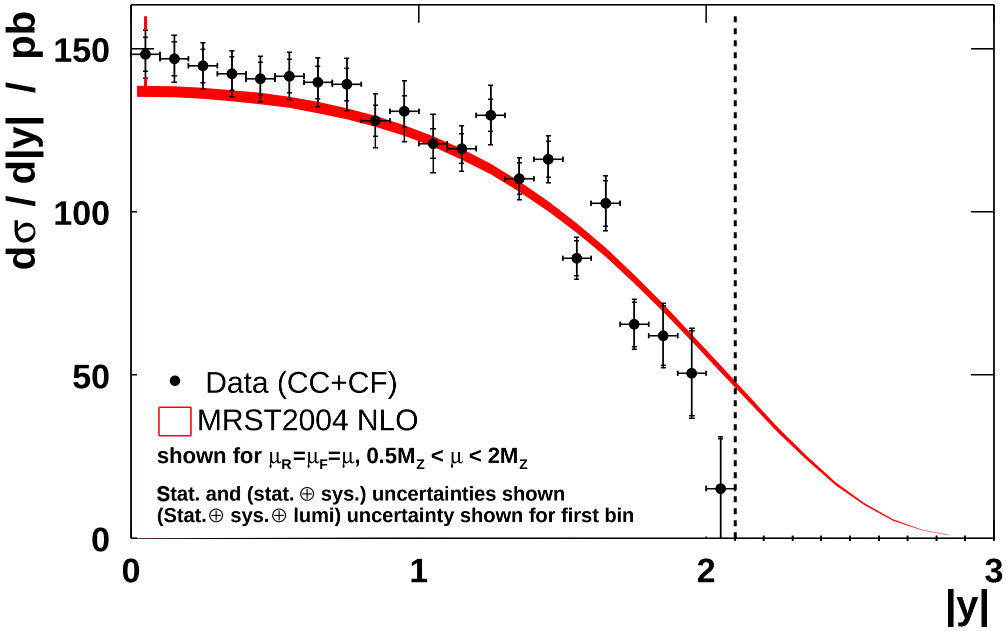

**Figure 65:** *$d\sigma/dy$, compared to NLO calculation and showing the effect of varying the renormalisation and factorisation scales between $M_Z/2$ and $2M_Z$. The vertical dashed line gives the acceptance limit and a common 6% luminosity uncertainty is not shown except in the first bin.*

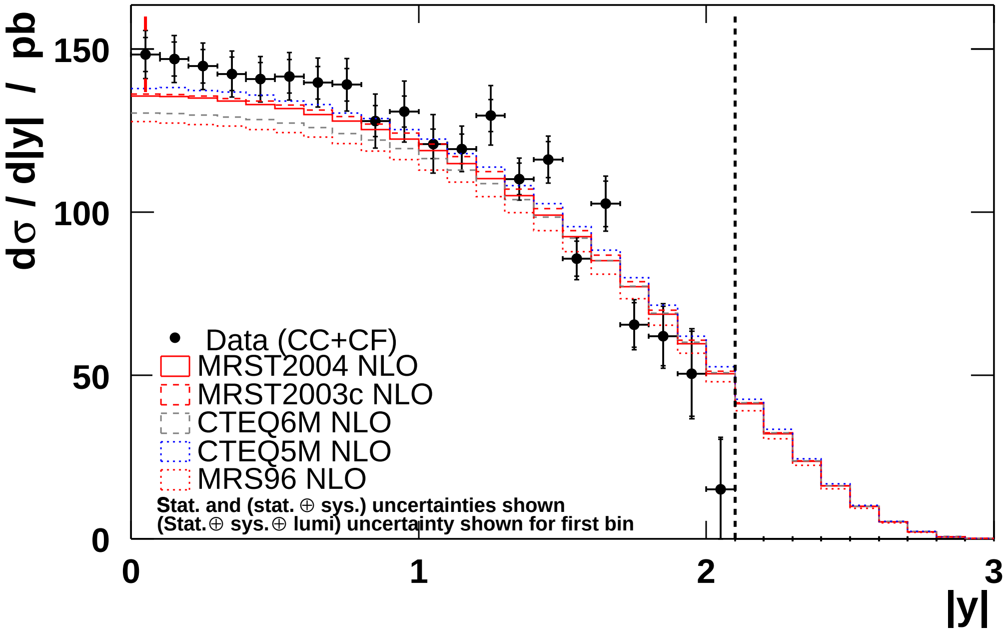

**Figure 66:** *$d\sigma/dy$, compared to NLO calculations made with* CTEQ *and* MRST *PDF sets (no normalisation). The vertical dashed line gives the acceptance limit and a common 6% luminosity uncertainty is not shown except in the first bin.*

| PDF set | $\chi^2$ / dof |
|---|---|
| NLO | |
| MRST2004 | 1.8 |
| MRST2003C | 1.5 |
| CTEQ6M | 2.8 |
| CTEQ5M | 1.3 |
| MRS96 | 4.0 |

**Table 23:** *$\chi^2$ between data and the calculations of $d\sigma/dy$ using different PDF sets shown in Figure 66 (no normalisation between measurement and calculation).*

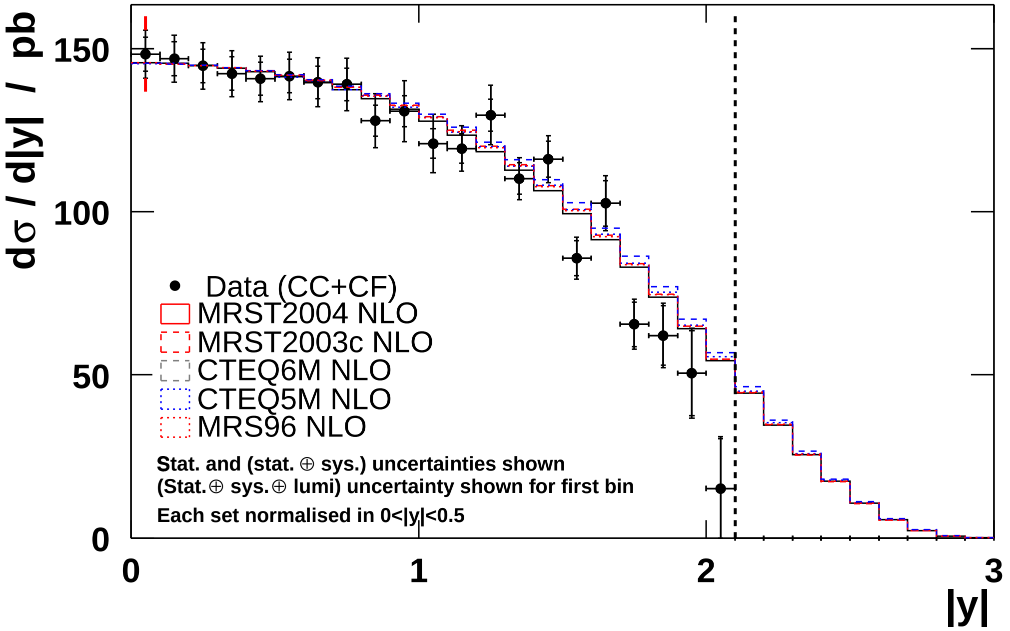

**Figure 67:** *$d\sigma/dy$, compared to NLO calculations made with* CTEQ *and* MRST *PDF sets. The calculation using each PDF set is normalised to the data in the region $|y| < 0.5$. The vertical dashed line gives the acceptance limit and a common 6% luminosity uncertainty is not shown except in the first bin.*

| PDF set | $\chi^2$ / dof |
|---|---|
| NLO | |
| MRST2004 | 1.0 |
| MRST2003C | 1.1 |
| CTEQ6M | 1.3 |
| CTEQ5M | 1.1 |
| MRS96 | 1.1 |

**Table 24:** *$\chi^2$ between data and the calculations of $d\sigma/dy$ using different PDF sets shown in Figure 67 (measurement and each PDF set normalised in the region $|y| < 0.5$.)*

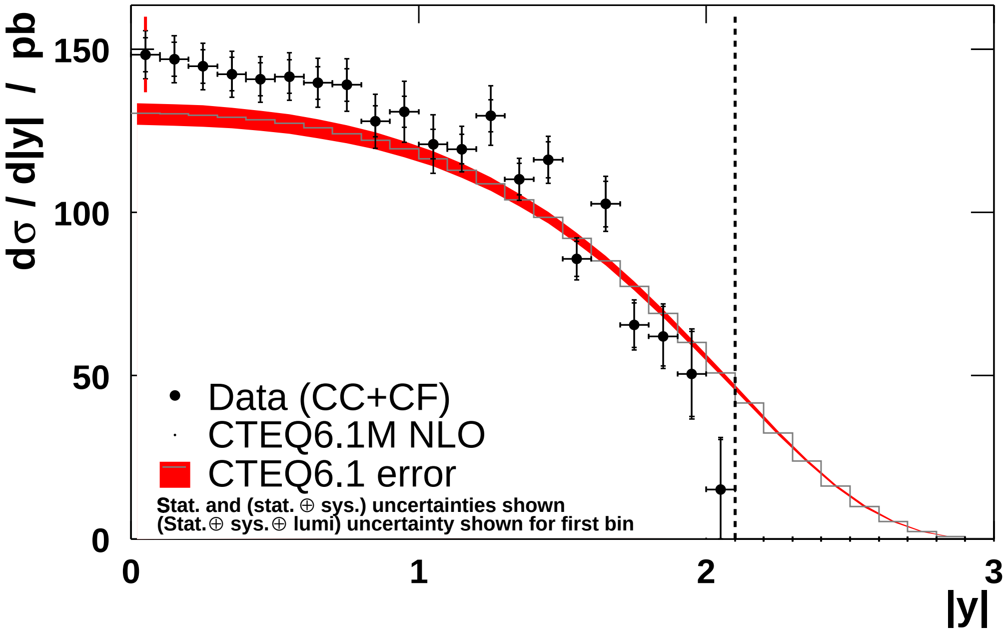

**Figure 68:** *$d\sigma/dy$, compared to NLO calculations made with the* CTEQ6 *error PDF sets (no normalisation).*

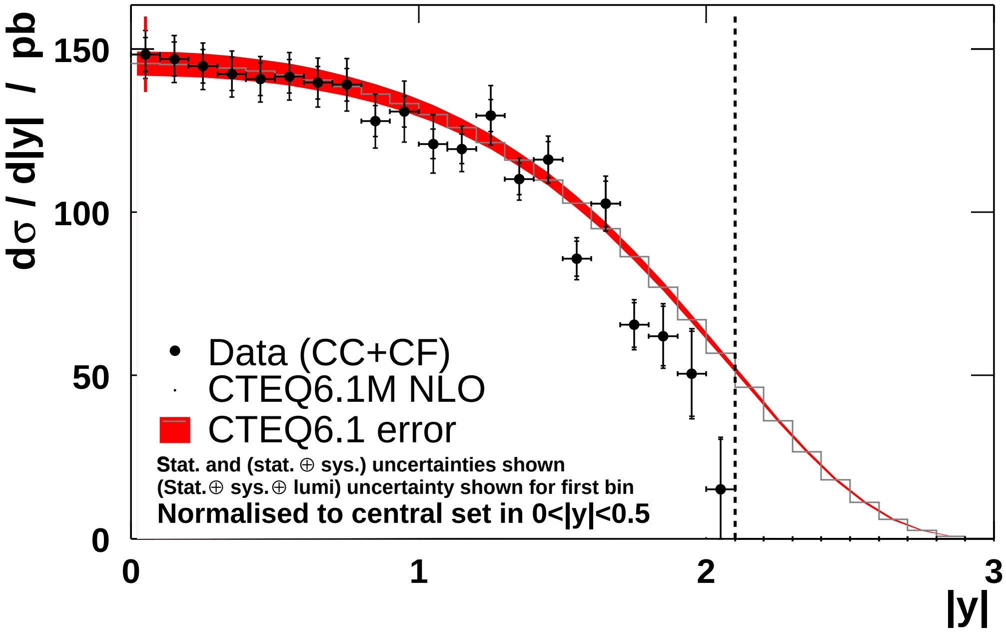

**Figure 69:** *$d\sigma/dy$, compared to NLO calculations made with the* CTEQ6 *error PDF sets. The calculation using the central PDF set is normalised to the data in the region $|y| < 0.5$, and the same scale factor applied to each error PDF set. The vertical dashed line gives the acceptance limit and a common 6% luminosity uncertainty is not shown except in the first bin.*

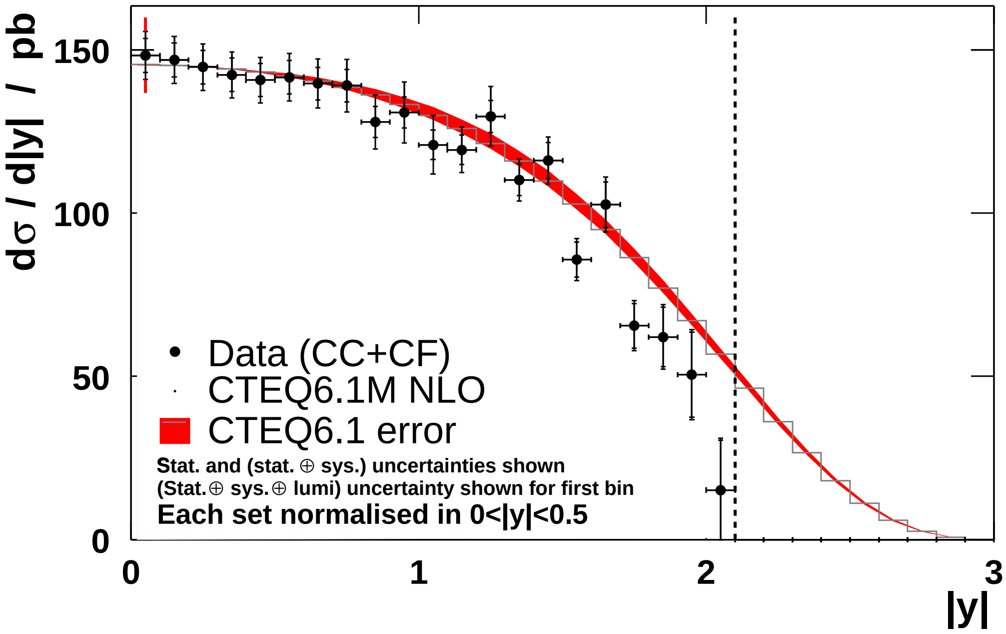

**Figure 70:** *$d\sigma/dy$, compared to NLO calculations made with the* CTEQ6 *error PDF sets. The calculation using each PDF set is normalised to the data in the region $|y| < 0.5$. The vertical dashed line gives the acceptance limit and a common 6% luminosity uncertainty is not shown.*

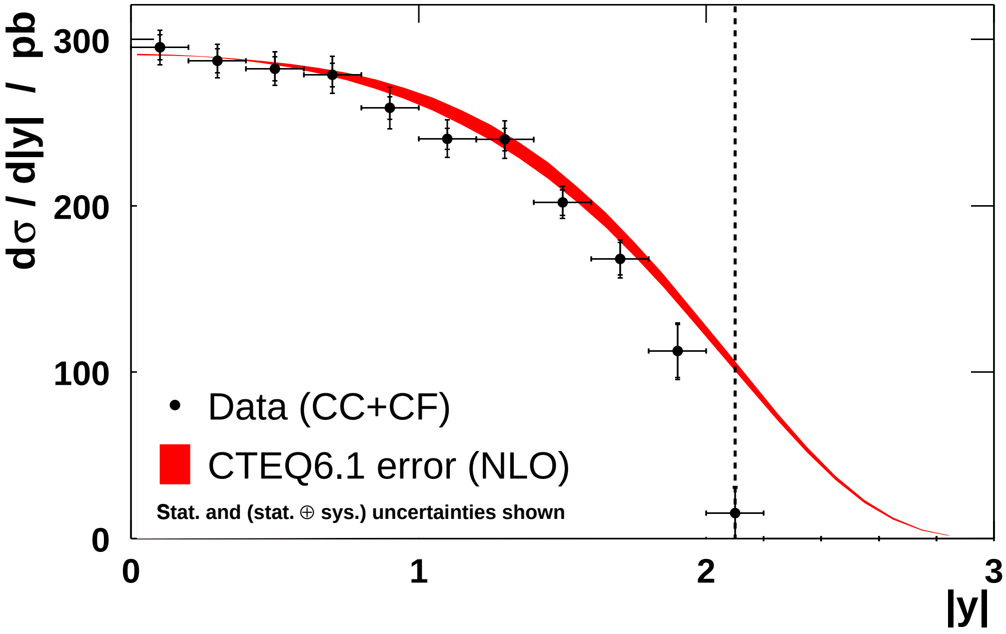

**Figure 71:** *$d\sigma/dy$, compared to NLO calculations made with the* CTEQ6 *error PDF sets. The vertical dashed line gives the acceptance limit and a common 6% luminosity uncertainty is not shown. This figure is the same as Figure 70, but with coarser binning.*

**Forward-Forward Events** Owing to the very low efficiency for forward-forward events as a result of the silicon tracking requirement, the forward-forward events were not included in the total cross-section measurement. However they are interesting as they probe the highest region of rapidity.

The reconstructed invariant mass is shown for the forward-forward events in Figure 72, and demonstrates how clean the sample is when a tracking requirement is applied. The rapidity distribution of candidate events is shown in Figure 73, and it is seen that these events add five bins of rapidity to the previous CC+CF results, extending the measurement close to the kinematic limit.

Figure 74 shows $d\sigma/dy$ calculated from forward-forward events, overlaid on the previous CC+CF distribution.

The total cross-section that comes from integrating $d\sigma/dy$ measured from forward-forward events is:

$$(91.7 \pm 38.6_{\mathrm{stat}} \pm 5_{\mathrm{lum}})\,\mathrm{pb} \qquad (1.2 < |y| < 2.6) \;\; ,$$

which on correcting for the range of $y$ sampled gives:

$$(252 \pm 106_{\mathrm{stat}} \pm 15_{\mathrm{lum}})\,\mathrm{pb} \;\; .$$

As the cross-section measured from the forward-forward events is consistent with that measured from CC+CF events, the results may be combined, taking account correlations in the systematic uncertainties. The resulting measured $d\sigma/dy$ is shown in Table 25 and in Figure 75. $\chi^2/\mathrm{dof}$ is 0.8 (74%) for NNLO and 1.3 (12%) for NLO. When the predictions are normalised in the region $|y| < 0.5$ to take account of the luminosity uncertainty, the resulting $\chi^2/\mathrm{dof}$ is 0.87 (81%) for NNLO and 0.75 (65%) for NLO, which are both compatible with the data.

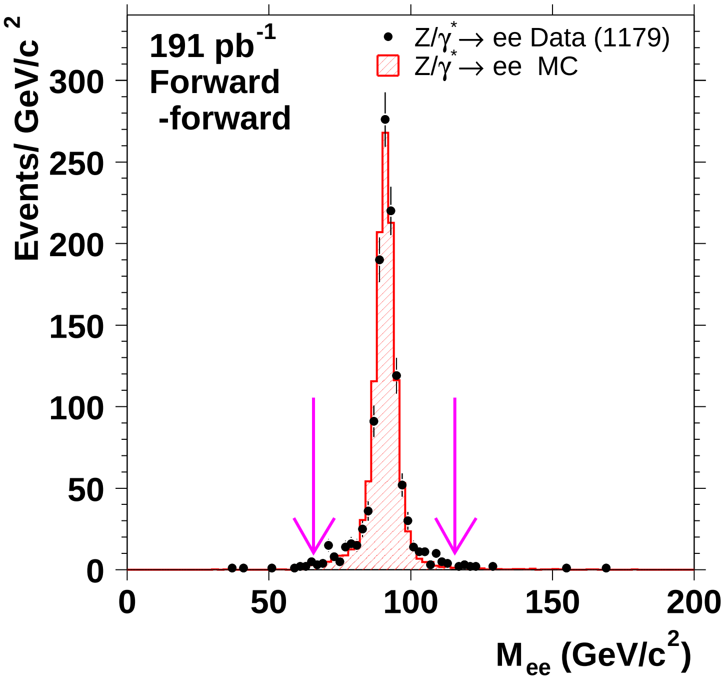

**Figure 72:** *$M_{ee}$ for forward-forward events.*

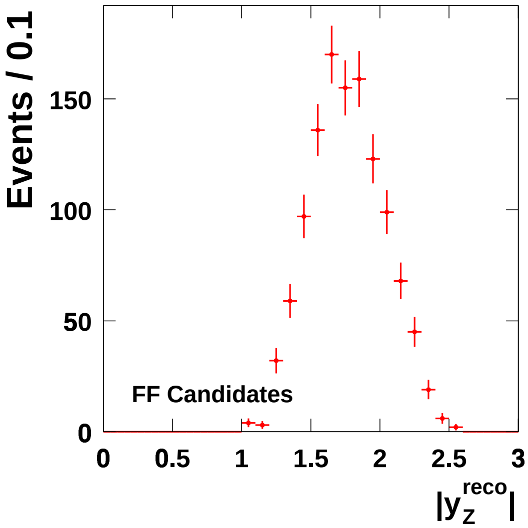

**Figure 73:** *Rapidity dependence of candidate events (FF).*

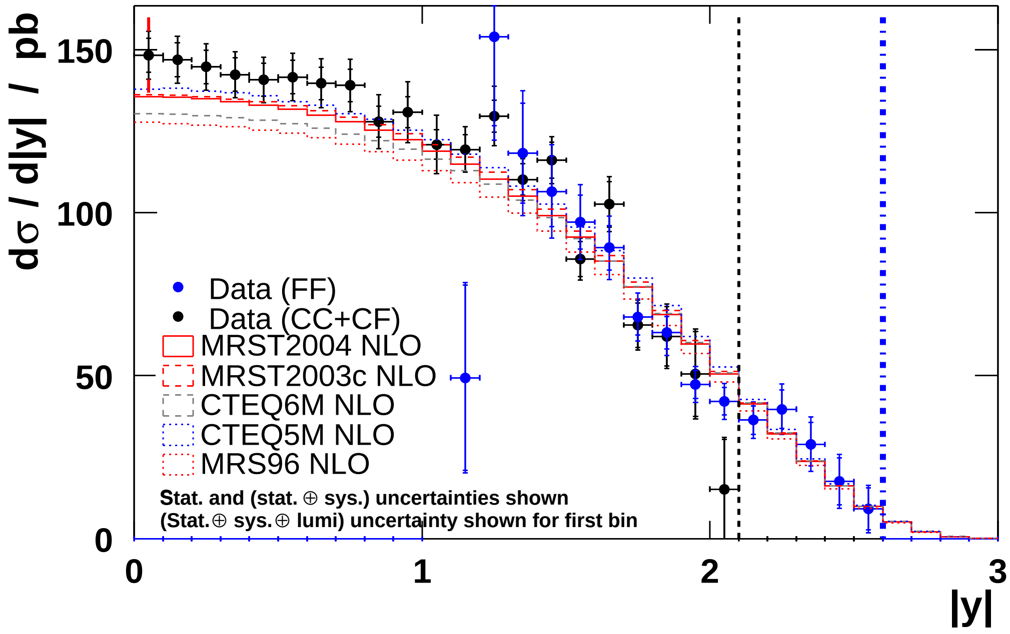

**Figure 74:** *$d\sigma/dy$, compared to NLO calculations made with* CTEQ *and* MRST *PDF sets (no normalisation). The vertical dashed line gives the acceptance limit for CC+CF events, and the vertical dash-dotted line the limit for FF events. A common 6% luminosity uncertainty is not shown except in the first bin.*

| $\lvert y\rvert$ | $d\sigma/d\lvert y\rvert$ / pb | stat.$\oplus$ sys. / pb | stat. only /pb |
|---|---|---|---|
| 0.05 | 148.3 | 7.4 | 5.2 |
| 0.15 | 146.9 | 7.2 | 5.2 |
| 0.25 | 144.7 | 7.1 | 5.2 |
| 0.35 | 142.4 | 6.9 | 5.1 |
| 0.45 | 140.7 | 6.9 | 5.1 |
| 0.55 | 141.6 | 7.0 | 5.1 |
| 0.65 | 139.6 | 7.2 | 5.0 |
| 0.75 | 139.0 | 7.7 | 5.0 |
| 0.85 | 127.9 | 7.8 | 4.8 |
| 0.95 | 130.6 | 8.8 | 4.8 |
| 1.05 | 123.3 | 8.6 | 4.6 |
| 1.15 | 116.3 | 6.9 | 4.3 |
| 1.25 | 132.7 | 9.1 | 4.9 |
| 1.35 | 112.4 | 7.9 | 4.7 |
| 1.45 | 112.9 | 9.7 | 4.9 |
| 1.55 | 92.1 | 9.8 | 4.7 |
| 1.65 | 94.4 | 11.7 | 4.8 |
| 1.75 | 67.9 | 9.3 | 4.3 |
| 1.85 | 63.6 | 10.1 | 4.4 |
| 1.95 | 47.8 | 7.7 | 4.1 |
| 2.05 | 42.2 | 8.0 | 4.2 |
| 2.15 | 36.6 | 7.5 | 4.4 |
| 2.25 | 40.0 | 9.6 | 6.0 |
| 2.35 | 29.2 | 9.3 | 6.7 |
| 2.45 | 17.7 | 8.7 | 7.2 |
| 2.55 | 9.2 | 7.6 | 6.5 |

**Table 25:** *$d\sigma/dy$ (CC+CF+FF events), with bin-centring corrections applied. A common 6% luminosity uncertainty is not shown except in the first bin.*

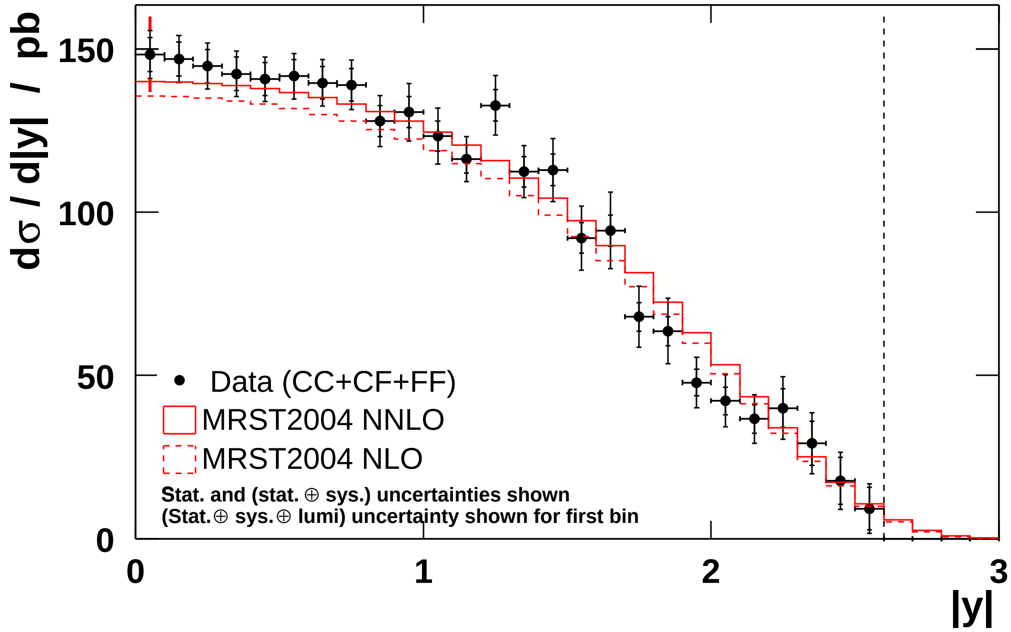

**Figure 75:** *$d\sigma/dy$, combined for central-central, central-forward and forward-forward events and compared to NNLO and NLO calculations made with* MRST *PDF sets (no normalisation). The vertical dashed line gives the acceptance limit and a common 6% luminosity uncertainty is not shown except in the first bin.*

| PDF set | $\chi^2$ / dof |
|---|---|
| MRST2004 NNLO | 0.8 |
| MRST2004 NLO | 1.3 |

**Table 26:** $\chi^2$ *between data and the calculations of $d\sigma/dy$ using the MRST 2004 PDF set shown in Figure 75 (no normalistaion).*

## 5.4. Outlook

High-precision measurements have been presented: the total cross-section for Z boson production has been measured to 2.2% in the electron channel (neglecting the 6% luminosity uncertainty), the ratio R measured to 1.9% in the electron and muon channels, and a measurement of $\Gamma(W)$ extracted of comparable uncertainty to the current direct and indirect combined world average.

However around twice the integrated luminosity is now available compared to that available at the cutoff for these analyses. These larger datasets will allow both statistical uncertainties and those systematic uncertainties that arise from limited statistics to be further reduced. In addition, the availability of calorimeter-seeded silicon tracking in the forward region, which has a much higher efficiency than the silicon standalone tracking used in these analyses, will allow the uncertainty on the forward-forward cross-section determination to be reduced.

The luminosity uncertainty of 6% is very much larger than the experimental uncertainties, and since the luminosity uncertainty arises in part from an experimental disagreement between CDF and E811, there is not room for more than modest improvement. Given that the experimental uncertainties are under control and the W and Z boson cross-sections are well-calculated at high orders, it is therefore possible that in future the cross-section measurements may be turned around and used to determine the luminosity. This could also be a useful technique at the LHC.

However at the LHC the PDF uncertainties will be very large: Figure 76 shows the effect of different PDF sets on the calculation of $d\sigma/dy$ in pp collisions at $\sqrt{s} = 14\,\mathrm{TeV}$ and a comparison with the distributions from $\mathrm{p\overline{p}}$ collisions at $\sqrt{s} = 1.96\,\mathrm{TeV}$ at the Tevatron. The W and Z total and differential cross-sections will therefore be among the first important measurements to be made at the LHC, both as standard candles in the understanding of the detectors required for all other high-$p_T$ physics measurements, and for the information they will give about the structure of the proton at very high energies.

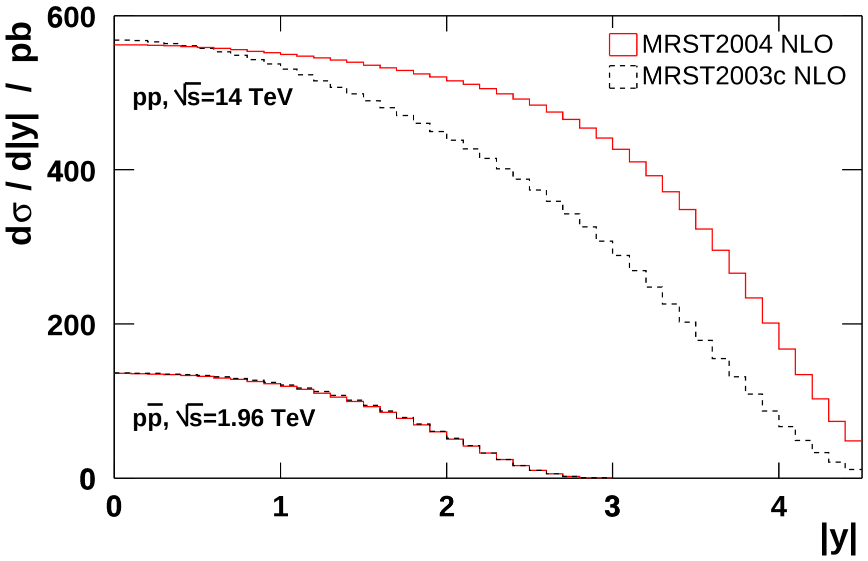

**Figure 76:** *$d\sigma/dy$ for $Z \to ee$ in $pp$ collisions at 14 TeV and in $p\bar{p}$ collisions at 1.96 TeV, computed using* MRST *PDF sets.*

## CDF Notes

The following CDF Notes were written by Robson et al. during the course of the work presented in this thesis. CDF notes are available from the author on request.

7332: *First Measurements of Inclusive W and Z Cross Sections from Run II of the Tevatron Collider* (October 2004), to be submitted to Phys. Rev. D.

7014: *First Measurements of Inclusive W and Z Cross Sections from Run II of the Tevatron Collider* (May 2004), Public CDF Note.

6939: *First Measurements of Inclusive W and Z Cross Sections from Run II of the Tevatron Collider* (March 2004), accepted by Phys. Rev. L.

6896: *A Combined Measurement of* $\sigma \cdot Br(\mathrm{Z} \rightarrow \mathrm{ee})$ *using Central-Central and Central-Plug Events in* $72\,pb^{-1}$ (February 2004).

6789: *Plug Electron Baseline Cuts as defined in Summer 2003 and their Efficiencies* (February 2004).

6681: *Measurements of* $\sigma \cdot Br(\mathrm{W} \rightarrow \mathrm{e}\nu)$, $\sigma \cdot Br(\mathrm{Z} \rightarrow \mathrm{ee})$ *and the Ratio R using CDF Run II Data* (rev. February 2003).

6642: *A Measurement of* $\sigma \cdot Br(\mathrm{Z} \rightarrow \mathrm{ee})$ *using Run 2 Central and Plug Electrons in* $72\,pb^{-1}$ (August 2003).

6573: *Estimate of the Amount of Material in the CDF Tracker using High-Pt Electrons* (rev. February 2004)

## References

[1] The CDF Collaboration, *The CDF II Detector Technical Design Report*, FERMILAB-Pub-96/390-E (November 1996)

[2] Aitchison, I. J. R. and Hey, A. J. G. *Gauge Theories in Particle Physics*, IOP (1989).

[3] Webber, B. R., Stirling, W. J. and Ellis, R. K. *QCD and Collider Physics*, CUP (1996).

[4] Brandelik, R. et al., Tasso Collaboration *Evidence for Planar Events in* $e^+e^-$ *Annihilation at High Energies*, Phys. Lett. B **86** 243 (1979).

[5] Abreu, P. et al., Delphi Collaboration *Experimental Study of the Triple-Gluon Vertex*, Phys. Lett. B **255** 466 (1991).

[6] Renton, Peter *Electroweak Interactions*, CUP (1990).

[7] Cooper-Sarkar, A and Devenish, R *Deep Inelastic Scattering*, OUP (2004).

[8] Ahmed, S. J. et al., The SNO Collaboration *Measurement of the total Active* $^8B$ *Solar Neutrino Flux at the Sudbury Neutrino Observatory with Enhanced Neutral Current Sensitivity*, Phys. Rev. L **92** 181301 (2004).

[9] Afforder, T. et al., The CDF Collaboration *Measurement of* $d\sigma/dy$ *for High Mass Drell-Yan* $e^+e^-$ *Pairs from p anti-p Collisions at* $\sqrt{s} = 1.8\,TeV$, Phys. Rev. D **63** 011101(R) (2001).

[10] Abe, F. et al., The CDF Collaboration *Measurement of the Lepton Charge Asymmetry in W-boson Decays Produced in p anti-p Collisions at* $\sqrt{s} = 1.8\,TeV$, Phys. Rev. Lett. **81** 5748 (1998).

[11] Pumplin, J. et al., CTEQ Collaboration *New Generation of Parton Distributions with Uncertainties from Global QCD Analysis*, JHEP **0207** 012 (2002). http://www.phys.psu.edu/ cteq .

[12] Martin, A. D., Roberts, R. G., Stirling, W. J., Thorne, R. S. *Physical Gluons and High* $E_T$ *Jets*, hep-ph/0410230; *Uncertainties of Predictions from Parton Distributions. I: Experimental Errors*, Eur. Phys. J. **C28** 455 (2003).

[13] Arnison, G. et al. *Experimental Observation of Lepton Pairs of Invariant Mass Around 95 ,GeV/*$c^2$ *at the CERN SPS Collider*, Phys. Lett. **126B** 398 (1983).

[14] Banner, G. et al. *Evidence for* $Z^0 \rightarrow e^+e^-$ *at the CERN* $\overline{p}p$ *Collider*, Phys. Lett. **129B** 130 (1983).

[15] Affolder, T. et al. *CDF Central Outer Tracker*, Nucl. Instrum. Meth. A **526** (2004) 249-299.

[16] Balka, L. et al. *The CDF Central Electromagnetic Calorimeter*, Nucl. Instrum. Meth. A **267** (1988) 272-279.

[17] Bertolucci, S. et al. *The CDF Central and Endwall Hadron Calorimeter*, Nucl. Instrum. Meth. A **267** (1988) 301-314.

[18] Albrow, A. et al. *The CDF Plug Upgrade Electromagnetic Calorimeter: Test Beam Results*, Nucl. Instrum. Meth. A **480** (2002) 524-546.

[19] Yasuoka, K. et al. *Response Maps of the CDF Central Electromagnetic Calorimeter with Electrons*, Nucl. Instrum. Meth. A **267** (1988) 315-329.

[20] GEANT 3 *Detector Description and Simulation Tool*, CERN Program Library Long Writeup W5013 (1993).

[21] Acosta, D. et al. *The CDF Cherenkov Luminosity Monitor*, Nucl. Instrum. Meth. A **461** (2001) 540-544.

[22] Klimenko, S. et al. *Averaging of the inelastic cross sections measured by the CDF and the E811 experiments*, FERMILAB-FN-0741 (December 2003).

[23] For 72 $\mathrm{pb}^{-1}$ dataset:
`http://www-cdf.fnal.gov/internal/physics/ewk/tools_and_datasets/good_run_list.html`
For later data: `http://www-cdf.fnal.gov/internal/dqm/goodrun/good.html`, Version 4.0.

[24] Sjostrand, T., Lonnblad, L. and Mrenna, S. *High-energy-physics Event Generation with* PYTHIA *6.1*, Comput. Phys. Commun. **135**, 238 (2001). Version 6.203.

[25] Kang, J. et al. *Measurements of* $\sigma.B(\mathrm{W} \rightarrow \mu\nu), \sigma.B(\mathrm{Z} \rightarrow \mu\mu)$ *and R using CDF Run II Data*, CDF Note 6711 v3 (March 2004).

[26] Veramendi, G., Robson, A. et al. *Estimate of the Amount of Material in the CDF Tracker using High-*$p_T$ *Electrons*, CDF Note 6573 v2.0 (February 2004).

[27] Anastasiou, C. et al. *High-precision QCD at Hadron Colliders: Electroweak Gauge Boson Rapidity Distributions at NNLO*, Phys. Rev. **D66** 094008 (2004).

[28] Private communication, W. James Stirling, NLO program, 2004a version including $b$-quark contributions.

[29] Sakumoto, W. *W/Z Cross-section Prediction Errors for* $\sqrt{s} = 1.96\,TeV$, CDF Note 6899 (February 2004).

[30] Wagner, R. G. *Electron Identification for Run II: Algorithms*, CDF Note 5456 v.2.1 (March 2003).

[31] Issever, C., Robson, A. et al. *Plug Electron Baseline Cuts as defined in Summer 2003 and their Efficiencies*, CDF Note 6789 v3 (February 2004).

[32] Private communication, Eva Halkiadakis.

[33] Nielsen, J. et al. *Trigger Efficiencies for High* $E_T$ *Electrons*, CDF Note 6234 (February 2004).

[34] Halkiadakis, E., Robson, A. et al. *Measurements of* $\sigma.B(\mathrm{W} \rightarrow \mathrm{e}\nu), \sigma.B(\mathrm{Z} \rightarrow \mathrm{ee})$ *and R using CDF Run II Data*, CDF Note 6681 v2.0 (February 2004).

[35] Sakumoto, W. and Hocker, A. *Event* $|Z_{vtx}| \leq 60\,cm$ *Cut Acceptance for Run II*, CDF Note 6917 (March 2004).

[36] Wagner, R. G. *Electron Identification for Run II: Understanding and Using Lshr*, CDF Note 6249 (January 2003).

[37] Wyatt, A. and Heinemann, B. *Correction for Leakage Energy and Multiple Interactions for electrons and photons in the Central and Plug Calorimeters*, CDF Note 6167 (Dec 2002).

[38] Corcella, G. et al. *HERWIG 6.5: An Event Generator for Hadron Emission Reactions with Interfering Gluons*, JHEP **0101** 010.

[39] Baur, U. et al. *QCD Corrections to Hadronic $W\,\gamma$ Production with Nonstandard $WW\gamma$ Couplings*, Phys. Rev. D **48** 5140 (1993).

[40] Sakumoto, W. *W/Z Cross Section Predictions for $\sqrt{s} = 1.96$ TeV*, CDF Note 6341 (Feb 2003).

[41] Private communication, James Stirling.

[42] Dorigo, T et al., CDF and D0 Collaborations *W and Z Cross-sections at the Tevatron*, hep-ex/0306008, 38th Rencontres de Moriond on QCD.

[43] Albajar, C. et al. *Measurement of the Ratio $R = \sigma_W Br(W \rightarrow \mu\nu)/\sigma_Z Br(Z \rightarrow \mu\mu)$ and $\Gamma_W^{tot}$ at the CERN Proton-Antiproton Collider*, Phys. Lett. **B253**, 503 (1991).

[44] Alitti, J. et al. *Measurement of the W and Z Production Cross-sections at the CERN $p\overline{p}$ Collider*, Z. Phys. C **47**, 11-22 (1990).

[45] Abe, F. et al. *W and Z Boson Production in $p\overline{p}$ Collisions at $\sqrt{s} = 1.8$ TeV*, Phys. Rev. Lett. **75**, 1456 (1995).

[46] Abachi, S. et al. *Measurement of $\sigma \cdot Br(W \rightarrow e\nu)$ and $\sigma \cdot Br(Z \rightarrow ee)$ in $p\overline{p}$ Collisions at $\sqrt{s} = 1.8$ TeV*, Phys. Rev. Lett. **76**, 3070-3075 (1996).

[47] Abbott, B. et al. *Measurement of the Width of the W Boson from Measurements of $\sigma(p\overline{p} \rightarrow W + X) \cdot Br(W \rightarrow e\nu)$ and $\sigma(p\overline{p} \rightarrow Z + X) \cdot Br(Z \rightarrow ee)$ and their Ratio*, Phys. Rev. Lett. **76**, 3070-3075 (1996).

[48] Schmitt, M. *Updated Combination of e and $\mu$ Measurements of the W and Z Cross-sections and their Ratio*, CDF Note 6895 (May 2004).

[49] LEP Electroweak Working Group, *A Combination of Preliminary Electroweak Measurements and Constraints on the Standard Model*, hep-ex/0412015 (December 2004).

[50] Renton, P. B., *Precision Electroweak Tests of the Standard Model*, Rep. Prog. Phys. **65** 1271 (2002).

[51] Particle Data Group, *Review of Particle Physics*, Phys. Rev. **D66** 010001 (2002).